High-Temperature Superconductivity in a family of Iron Pnictide Materials

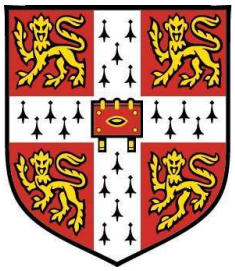

Jack Gillett

Department of Physics

University of Cambridge

A thesis submitted for the degree of

Doctor of Philosophy

October 2011

This dissertation is the result of my own work and includes nothing which is the outcome of work done in collaboration except where specifically indicated in the text.

Ultimately, support for this project has come from the working people of the World, to whom I would like to dedicate it, particularly to those who did not enjoy my fortunate start in life. It is my sincerest hope that they may one day derive some benefit from it.

Acknowledgements

Although I have been able to make many measurements on the samples I have grown during the project, some were outside of my capabilities or breadth of experience. The following datasets presented in this work were measured by collaborators: Resonant Ultrasound Spectroscopy data presented in chapter 6 was measured by Prof. Michael Carpenter in the Earth Sciences department at the University of Cambridge; and the Heat Capacity with Doping data presented in chapter 5 was measured by Dr. Jose Espeso from CITIMAC, Universidad de Cantabria, Spain. In both cases, the samples were grown and characterised by myself, and all data analysis presented was done by myself. The X-Ray Diffraction data presented in chapter 4 was performed in collaboration with Dr. Jacqui Cole from the Structure and Dynamics Group in the Cavendish, who also performed the quantitative analysis on the dataset. Chapter 7 also discusses the work of several collaborators, borrowed data and graphs are referenced in the text.

I have also borrowed data from the literature for use in figures at a small number of points, in all cases this is acknowledged in the text.

I would like to thank the EPSRC and Trinity College, through whom funding for my work was directed, and without whom it would most certainly have been a significantly more arduous experience.

I would also like to thank all of the Quantum Matter group in the Cavendish for their continuing support, especially my supervisor, Gil Lonzarich, who has been supporting throughout my time in the lab; John Cooper, which whom it has been a pleasure to have worked and who's assistance has been above and beyond the call of duty; Suchitra Sebastian, who has been a fantastic advisor, particularly in

the field of sample growth; Dan Hills, for teaching me how to make resistance measurements; Montu Saxena, for the use of his pressure cell in chapter 4; Paul Nahai-Williamson, for his invaluable support in setting up said cell; Doug Astill, for his tireless support with the various instrumentation used during my project; and Sitikantha D. Das, for his help in making many of the crystal samples discussed here. I would also like to mention the various residents of office 419A, who were perpetually cheerful and enjoyable to work alongside.

Abstract

The work in this thesis falls roughly into three parts, which I characterise loosely as a developmental stage, an exploratory stage, and an attempt to contribute to understanding of the field.

In the developmental stage, I have worked to design a variety of methods to create high-quality samples of various Iron Pnictide superconductors, to dope them with various chemicals and to characterise the resulting crystalline samples. I discuss in depth the signature of good quality crystals and the various experiments that they have been used in by myself and my collaborators. These processes are ongoing and will hopefully continue to contribute to my research group's capabilities.

My exploratory work involves a detailed survey of one particular family, $Sr(Fe_{1-x}Co_x)_2As_2$, as the level of Cobalt is varied, and the mapping of the phase diagram for the system (shown below and repeated in chapter 4). I have also made a comparison to the better-measured Barium analogue, and discuss the reasons for the differences in character between the two, most notably the lack of a splitting of the structural and magnetic transitions in the first species. I also discuss the effect of pressure, which can lead to superconductivity in lightly doped samples for very modest pressures; and annealing, which increases transition temperatures within samples, on a limited quantity of crystals.

Finally, I attempt to contribute to the understanding of the field via a series of Resonant Ultrasound Spectroscopic experiments conducted by a collaborator on my crystals and analysed by me. I see distinct first-order transitions in the parent compounds, characterisable above

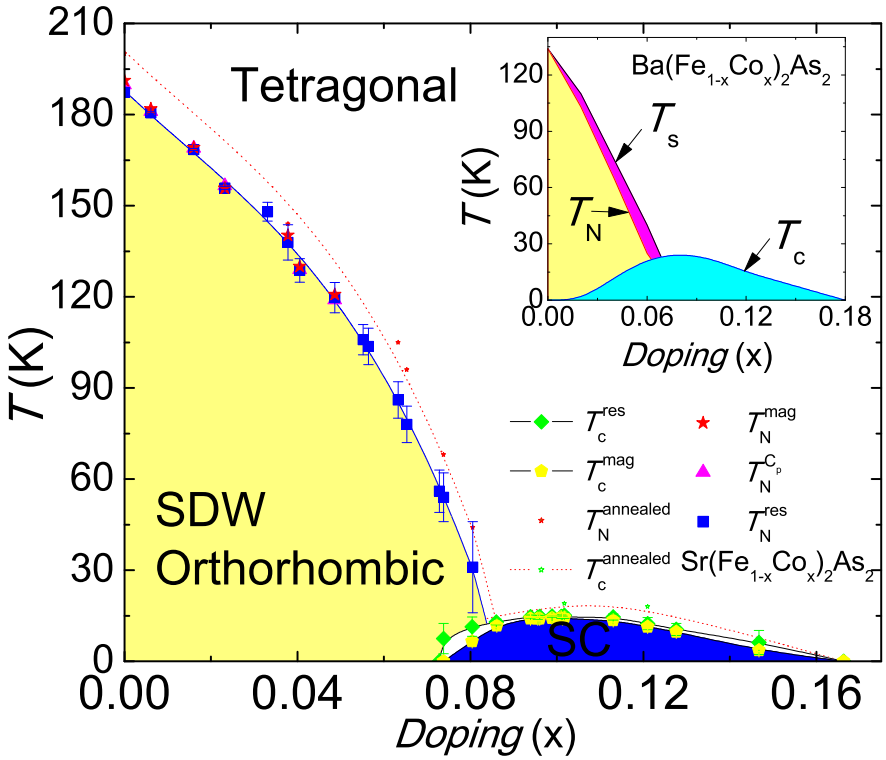

Figure 1: My measured phase diagram of Co-doped Sr122 from Magnetisation, Heat Capacity and Resistivity. The upper dashed lines correspond to higher Neel and critical temperatures for annealed samples. The inset shows a schematic of the phase diagram of Co-doped Ba122 constructed from our measurements and previous reports [12; 50]

the high-T structural transition within a Ginzburg-Landau pseudo-proper ferroelastic scheme for a transition coupling weakly to strain but driven by another order parameter. My observations allow several statements about the symmetry of the order parameter and are suggestive of a non-magnetically driven structural transition. In the case of doped samples a much richer behavior is seen, with a broad transition and simultaneous relaxation of all elastic peaks and a broad temperature range of significant dispersion. The effect of the softening is seen far above T_N and lends strong support to the familiy of models predicting such high-T fluctuations.

Contents

List of Figures

List of Tables

LIST OF TABLES

Chapter 1

Introduction

The iron pnictides, discovered in early 2008, have proved to be a most remarkable class of superconductor. The obvious high superconducting transition temperatures of up to about 55K [10; 25] aside, the variety of families and number of ways in which superconductivity can arise is fascinating. The best known families, ReFeAsO (where Re is a Rare Earth metal, henceforth the '1111' compounds) and AFe_2As_2 (where A is an Alkaline Earth metal, known as the '122' compounds and henceforth variously Ca122, Sr122 and Ba122), can be made superconducting by the application of pressure, by a variety of dopants - in many cases electron-doping and hole-doping can *both* lead to superconductivity, reaction with atmosphere leading to unwanted surface superconductivity, or in some cases even by gentle simmering in red wine[14]!

Crucially, a new chapter in high-T_c superconductivity has been established now that Copper Oxide layers have been realised not to be critical. Even binary iron systems, lacking the Iron Arsenic layers of the 1111 and 122 families, have been discovered to superconduct, notably FeSe and doped $FeSe_{1-x}Te_x$ [76].

There are often other transitions in these systems that can be suppressed by the application of a tuning parameter (magnetic field, pressure etc.), and that as they are driven towards 0K, new forms of ordering emerge. Indeed, it was rapidly found that chemical doping lowers the high-temperature transitions until at some critical doping superconductivity emerges. Superconductivity near to such critical points is very interesting. Firstly, since it is so close to a magnetic transition, it is an ideal candidate for unconventional superconductivity. Secondly, at 0K

the laws of thermodynamics tell us that entropy changes disappear. So, samples on both sides of the transition must be equally ordered - frequently the lack of an observable order parameter means that one state must have some 'hidden ordering'.

A large part of the work presented here has been explorational. I have developed methods and materials to study the pnictides, most notably the 122 families with cobalt doping [35], and looked at the resultant behaviour. Although similar, there are critical differences between the two families which I attempt to address. I perform a careful examination of the evolution of the magnetic to superconducting transition with doping, and in particular explore whether any splitting of the structural and magnetic transitions can be discerned in the manner of Co-doped Ba122 [47].

I find evidence of a first order transition in Sr122 from a variety of experimental probes [18], where the magnetic transition coincides with the structural transition. It has been suggested that the first orderness of this transition is related to the larger interlayer exchange in the more three-dimensional [74] Sr122 and associated with the suppressed superconductivity, and further separation of the superconducting dome in Co-doped Sr122 compared to Co-doped Ba122. I look in more detail at the transition by means of Resonant Ultrasound Spectroscopy (RUS), a technique sensitive to any elastic contributions to phase transitions, in order to probe the evolution of the transition on doping.

The field is still moving incredibly quickly and fascinating insights are being developed on a daily basis. Perhaps the most important theme is that copper oxide is no longer critical to elevated T_cs. However, there are many similarities between the systems that provide tantalising clues to the behaviour of the systems. Both structures are layered and demonstrate highly anisotropic superconductivity. Both seem to be close to magnetic instabilities, suggesting that magnetic fluctuations might be critical to a microscopic understanding of high T_c. Both have very sensitive dependence on stoichiometry, but perhaps most importantly, however, the undoped parent compounds in the new family are metallic rather than insulating. This allows Fermi surface measurements to follow the development of the superconducting state that is not possible in the insulating cuprates, and shows that a doped Mott insulator is not the only route to high T_cs.

Chapter 2 will discuss in brief some of the important experimental and theoretical results on the iron arsenide superconductors, particularly those with relevance to my study.

In Chapter 3 gives an introduction into my growth procedure and developments to work with the iron arsenides. It also discusses the various methods of characterisation that I have used to optimise crystal quality.

Chapter 4 looks at my work to probe the phase diagrams of one of these systems, with particular focus on magnetic ordering at the high-T transition.

Chapter 5 will discuss briefly the application of Ginzburg-Landau theories to structural phase transitions, and then cover my efforts to probe this transition via elastic techniques. It includes my attempts to build a Ginzburg-Landau model that accurately describes the transition.

Chapter 6 will discuss a small selection of the various collaborations that have involved the use of my crystals, including a brief summary of the techniques and any specific growth problems that had to be overcome.

Finally, Chapter 7 will summarise the work presented and discuss avenues for further study of these families of materials.

Chapter 2

A Review of Superconductivity in the Iron Arsenides

There are several questions to be answered regarding superconductivity in the Iron Arsenides. Firstly, the wide range of families of materials leads to questions about the role played by the crystal structure, and its relationship with dopants. We are interested in the microscopic nature of magnetic ordering, and whether it plays a part in forming Cooper pairs. However we are mainly interested in the electronic structure and the pairing symmetry of the superconducting wavefunction. All of these have been addressed in great detail by many research groups since the discovery of the pnictides, I attempt to give a brief overview of some of the important results.

2.1 Material Families and Crystal Structures

Although initially called the Iron Pnictide superconductors, the diversity of families exhibiting superconductivity was recently extended to the binary Iron Chalcogenides [20; 76], featuring tellurium and selenium instead of the Pnitogen, showed that Fe-As layers were themselves not the critical factor.

To date the families can be broadly classified into the 1111 and 122 families, the binary 11 Iron Chalcogenides, the 111 materials such as LiFeAs [69], and more exotic and two-dimensional materials with larger blocking layers such

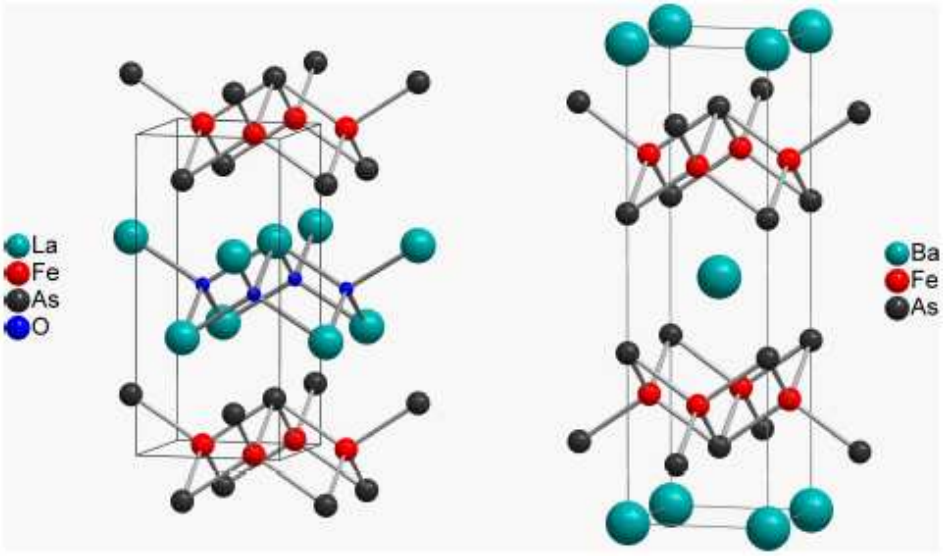

Figure 2.1: From ref. [70]. The general crystal structure of the 1111 and 122 Iron Arsenides

as $(Fe_2P_2)(Sr_4Sc_2O_6)$ [51]. By far the most explored system is the 122 family, due largely to the simplicity of their crystal structure and diversity methods of induction of superconductivity, and it is to this family that most of my work is directed.

Superconductivity can be induced in the 122 compounds by doping with many materials. Unlike the cuprates, in which superconductivity is extremely sensitive to doping in the Cu-O planes, in the 122 pnictides superconductivity has been realised by changing each of the three constituents [54; 55; 72]. In these systems long range magnetic order is first suppressed before the onset of superconductivity. The role of doping is also not straight-forward. While initially it was envisaged to be a purely charge-doping effect, where extra electrons or holes are added to the 'blocking' layers leading to an optimal charge density for superconductivity, more recent work has shown that even isovalent substitution can cause superconductivity [54].

Pressure has also been shown to suppress magnetism and cause superconductivity. A seminal work by myself and collaborators showed that in both $SrFe_2As_2$ and $BaFe_2As_2$, pressure alone was enough to stabilise a superconducting state [2]. The dependence on the method of applying pressure is also non-trivial, with

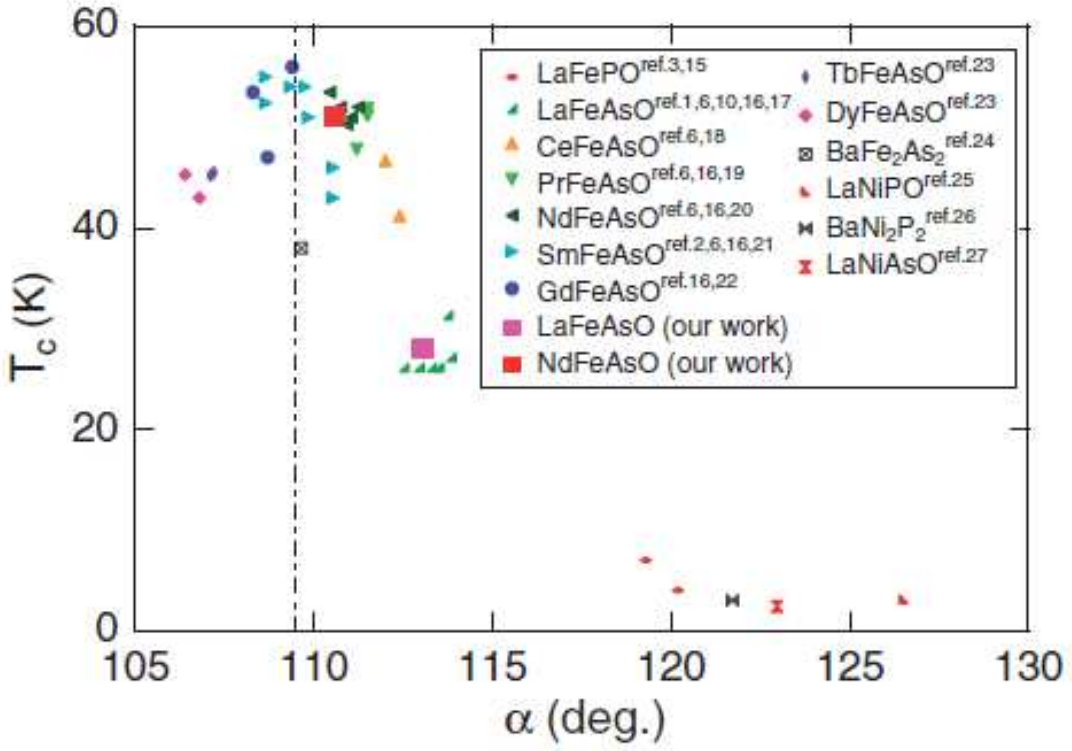

Figure 2.2: Taken from ref. [34]. Superconducting T_cs in many pnictide families plotted against α, the Fe-As bond angle in the Fe-As planes within the compounds. The highest observed T_cs are seen to be culstered around the 'ideal' tetragonal angle of 109.47 degrees

work showing that $CaFe_2As_2$, for example, will *only* superconduct under non-hydrostatic pressure [79].

An early observation was that peak T_cs values are largely achieved, whether through pressure or doping, when the bond angle within the $FeAs_4$ tetrahedra in the Fe-As layers is near the tetragonal angle of 109.47 degrees [34], shown in figure 2.2. This led to suggestions that the effect of doping is purely to induce 'chemical pressure' by varying lattice parameters of the doped compound. Indeed, there is a remarkable similarity between the effect of pressure and doping upon lattice parameters in several superconducting compounds [28]. However, this suggestion is also rather too simplistic, since several 3d and 4d metals suppress magnetism without leading to superconductivity [4; 61].

Many families exhibit a tetragonal-orthorhombic phase transition either co-

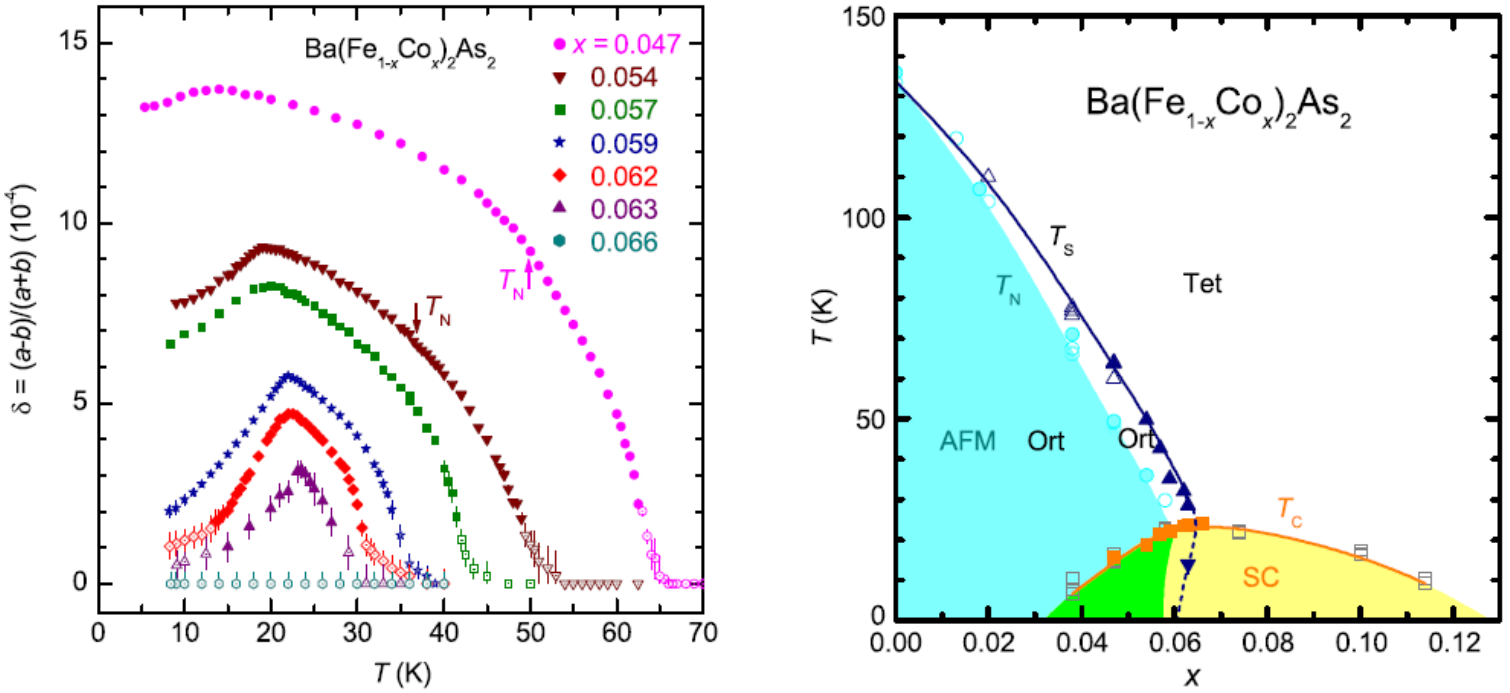

Figure 2.3: Taken from ref. [47]. The left panel shows the orthorhombic distortion in $Ba(Fe_{1-x}Co_x)_2As_2$ for various values of x. The structure is seen to become orthorhombic some distance before the Neel transition in the doped compound. Once it becomes superconducting, the distortion begins to fall again. The right-hand panel shows the measured x-T phase diagram for the material. T_s marks the onset of the orthorhombic distortion, where δ in the left panel becomes non-zero, and T_s marks the onset of magnetism. The region between these two curves is suggested to be a non-magnetic orthorhombic state

inciding with or at a slightly higher temperature than the magnetic ordering. Since magnetic ordering needs to be largely suppressed for the onset of superconductivity, it was thought that only the tetragonal state could support superconductivity. However, detailed x-ray work [47] has shown that superconductivity occurs in both phases at low temperature, and that in those samples that are orthorhombic, orthorhombic distortion increases as T is lowered towards T_c and then decreases again below T_c, shown in figure 2.3.

2.2 Magnetic Ordering below T_N

Below the Neel temperature, these materials are found to order with anti-ferromagnetic stripes along the longer orthorhombic axis and ferromagnetic stripes along the shorter orthorhombic axis, as predicted by density functional theory (DFT) calculations. However, such calculations overestimate by several times the measured ordered moment of $\sim 0.4\mu_B$ (LaFeAsO) - $0.9\mu_B$ (NdFeAsO, Ba122); the discrepancy has been attributed to strong spin fluctuations in the ordered state [62].

In some systems, notably the 1111 compounds, the structural transition precedes the Neel transition by ~10K, although this separation has been shown to be sample-dependent, with better quality samples showing a smaller splitting [23]. Although in the 122 parent compounds the two transitions coincide, on doping Ba122 with certain materials the transition is seen to separate, again by up to 10K [12; 50].

Since the system is metallic, itinerant antiferomangetism might be expected as for chromium. However, fixed-spin models have been shown to give a good fit to spin dispersion observed by inelastic neutron scattering across the entire Brillion zone [80], although they give highly anisotropic $J_{1a} - J_{1b}$ coupling constants along the two orthorhombic axes. More recently itinerant models have been developed that seem to work at least as well [29]. In this itinerant picture, the magnetic order is described by a spin density wave (SDW), coming from a Fermi surface reconstruction due to a significant nesting vector in the (π, π) direction. There is some direct evidence of an SDW gap forming from optical spectroscopy [21].

2.3 Electronic Structure in the Pnictides

Early theoretical work into electronic structure explained why pnictides are susceptible to superconductivity via both hole- and electron-doping [77]. A deep gap in the Fe-d orbitals is centred on the Fermi energy, and charge-doping of either sign is sufficient to move into an area of heavy carriers with a large fermi surface.

Various bandstructure models have been tried, the most successful of which have been 5-band models [27], successfully simulating the various Fermi surface pockets seen in quantum oscillations and ARPES. The high-temperature Fermi surface of most materials in the family is largely two-dimensional, with two central hole-like cylinders and several outer electron-like Fermi arcs at the zone boundary - in another early work we showed the large reduction in Fermi surface across the magnetic transition in Sr122 via De Haas van Alpen oscillations via nesting [59] as discussed above.

The pairing symmetry of the order parameter has also come under intense scrutiny. Proximity to magnetic order hints at unconventional pairing mediated by magnetic fluctuations. Indeed, the pnictides conform to a variety of criteria that have been predicted for such exotic superconductivity [44]; they are largely 2-dimensional, leading to strong nesting behaviour; proximity to antiferromagnetism leads to spin susceptibilities that can be rather large; and d-shell character provides a larger magnetic energy scale than in comparable f-shell superconductors. Unlike a phonon-mediated interaction attractive interactions are not necessarily isotropic, leading to wavefunctions displaying angular and radial nodes at certain points on the fermi surface.

Various wavefunction symmetries were rapidly ruled out, microwave penetration measurements showed a fully gapped state in both the 1111 and 122 materials [42; 46] (although evidence is not totally unambiguous, a resolution between gapless and gapped observations is offered in ref [62]). Recently a large body of evidence has been growing to support the $s_{\pm}$ state pair wavefunction [24; 63] predicted early on from bandstructure calculations [43], with a sign change occurring along the radial momentum direction, and between inner and outer fermi pockets; with two superconducting gaps forming, one from the central hole fermi surface sheet and one from the outer electron fermi surface sheets, shown in figure 2.4.

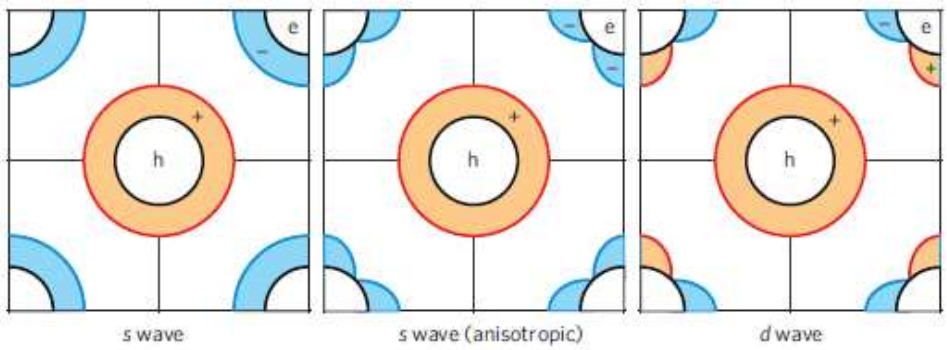

Figure 2.4: Taken from ref. [53]. Three possible pairing scenarios for the iron pnictides. In the isotropic $s_{\pm}$ case, a sign-change between the inner and outer Fermi surface sheets leads to two distinct nodeless gaps. In the anisotropic case, the gap on the electron Fermi surface has line nodes but no sign change. Finally in the d-wave case (mostly ruled out, see text), the electron sheet has a nodal gap that also shows a sign-change.

Similar behaviour has been seen in other pnictide families [64].

The most convincing argument for d-wave superconductivity in the cuprates came from experiments showing a sign-change across a corner junction. Although d-wave has been largely ruled out in the pnictides, it is much less easy to distinguish $s_{\pm}$-wave from various other possible s-wave configurations(figure 2.4, ref. [53]), and to date experimental evidence is limited.

2.4 Seperation of T_N and T_s in some materials

One of the most interesting phemomena in these materials is the splitting of T_N and T_s alluded to above. In some doped Ba122 compounds, two separate transitions have been seen, with the structural transition occuring first but magnetism only setting in below the second transition. Since magnetism is expected to be the driving force behind the structural transition, the observation of T_N being pushed below T_s is very strange. A rich discussion has evolved in the literature around this.

It is interesting to consider how such a splitting from one to two transitions could emerge from a Ginzburg-Landau theory discussed in the last chapter. Clearly it could be artificially inserted via a second order parameter with a different critical temperature, and such an approach has been demonstrated to provide

the correct order of phase transition [7]. However, such a model does not explain the transition from one type of behaviour to the second on doping.

Measurements on detwinned crystalline samples revealed asymmetry in different directions even above the transitions [67]. Directional anisotropy in an isotropic crystal state is behaviour conventionally associated with nematic liquid crystals, and the picture developing to describe this is called the 'nematic' picture[1]. Theories developed to explain this behaviour [45; 73] predict large fluctuation effects whose effects reach high above the Neel temperature, which will later be seen to be in line with my observations on doped Sr122 and Ba122.

[1] although X-ray measurements have shown residual orthorhombicity all the way up to 450K [36], so some caution regarding phase separation is required.

Chapter 3

Metallic Flux Growth

3.1 Sample Preparation and Metallic Flux Growth

In order to study materials experimentally, a source of high-quality samples is required. Such samples can come in either polycrystalline or single crystal form. In the former, many microcrystals are fused together with random orientations. Although these can be useful for detecting some properties of materials and are generally easier to synthesise, properties measured will be an average over crystal orientation. For measurement of anisotropic properties single crystals are vital.

We have spent a significant amount of time developing effective methods for synthesis of high-quality single crystal samples. This has built on the recent expansion of the Quantum Matter group's sample preparation facility which uses high-temperature metallic flux growth methods that will be described here. The iron arsenides have proved particularly challenging and developments and refinements to the method for these samples will also be discussed.

The method of crystal growth from metallic fluxes is well described in the literature [5]. The desired constituents are mixed in a chosen molar ratio and heated in a sealed environment with metallic flux. At high temperature the flux melts, and reactions are able to take place in the liquid phase. As the temperature is slowly reduced, crystals form in the liquid flux (much like salt crystals forming from Na^+ and Cl^- ion in brine solutions). A finishing temperature is chosen such that the flux will still be liquid, and the ampoule is removed from the furnace

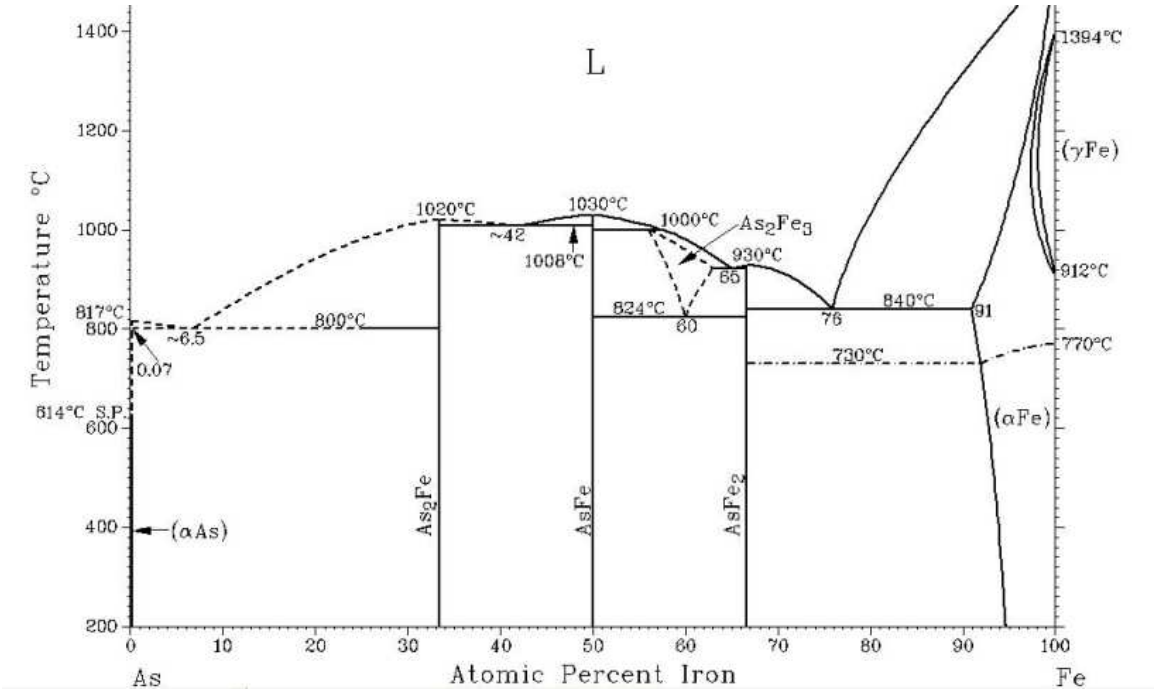

Figure 3.1: The phase diagram for a mixture of Iron and Arsenic from ref. [52]

and spun in a centrifuge to separate the liquid flux from solid crystals formed within. The flux rapidly cools and when the container is opened crystals can be easily retrieved, as described later.

Figure 3.1 shows the chemical phase diagram for a mixture of iron and arsenic. The upper section shows the region where all components form a homogenous liquid, the curved line separating it from the lower section is called the liquidus. In the lower section different areas represent equilibrium between different solid and liquid components. Vertical lines show the thermodynamically stable solid phases - in this case Fe_2As, FeAs, and $FeAs_2$. The phase diagram shows the behaviour of the melt as we vary temperature and composition.

As an example, we can consider a mixture of As_8Fe_2. When warmed above the liquidus at about 920 °C it will melt into the liquid phase. On cooling back to this temperature it will begin to precipitate out $FeAs_2$, which will increase the concentration of As in the melt and the remaining liquid follows the liquidus to the left. At 800 °C, much $FeAs_2$ has left solution and only about 6.5% of the remaining liquid is Fe. At this point we reach a minimum of the liquidus -

below this point all remaining liquid solidifies. We can see that although $FeAs_2$ does not melt until 1020 °C, we have been able to precipitate $FeAs_2$ crystals at lowered temperatures by use of excess As - we call arsenic a flux, it provides a liquid phase for the formation of $FeAs_2$ to take place. In other cases we will use a different substance, often tin, for the same purpose. We are limited to a maximum temperature of around 1200 °C by the softening temperature of quartz, so such considerations can prove critical.

Although growth of two-component compounds is fairly straightforward when the binary phase diagram is known, growth of compounds with higher numbers of components is much harder, since due to the large number of possible combinations, ternary and higher phase diagrams are rarely known in detail. Thus, choice of composition becomes largely an empirical process, although binary phase diagrams can give some insight.

In our basic procedure the ratio of compounds is chosen, quantities are measured from high-purity ingredients (usually at least 99.999% purity) and weighed to ±0.0005g. The ingredients are placed in an alumina crucible and put inside a quartz tube. Another crucible is filled with quartz wool (the 'catch crucible') and placed upside-down on top. More quartz wool is placed at either end of the whole arrangement for support. When the growth is spun in the centrifuge at the end of the process (the centrifuge used is shown later in figure 3.5), the catch crucible will act as a filter, 'catching' the precipitated crystals while the remaining melt flows off.

Sealing quartz involves heating it to very high temperatures with a hydrogen-oxygen blowtorch flame. At these temperatures quartz glows very bright white and behaves like a viscous liquid. Dark safety goggles must be worn to protect the eyes from this bright light. If the pressure on either side of the quartz is equal (eg. if the setup is open to atmosphere) as with any liquid, this very hot quartz will try to minimise its surface area by adopting a catenary formation, a smooth concave egg-timer shaped curve. If the growth is sealed, the pressure difference will lead to the soft quartz very rapidly expanding or contracting depending on the direction of the pressure difference. If it is sealed but there is initially no pressure difference, the heat from the torch will rapidly increase the internal pressure and lead to swelling.

Sealing the quartz tube is a two-stage process. The whole ampoule will reach over 1000 °C during the furnace step so it must be sealed at low pressure to prevent explosion. Sealing the ampoule requires closing one end of the tube with a blowtorch, but the quartz is too wide to seal in one step at low pressure (which causes the quartz tube to flow inwards too rapidly and implode as described above). So, while still open to the atmosphere the quartz tube is 'necked' - a large blue flame is used to thin the tube from 17mm diameter to about 6mm.

The entire arrangement is then connected to the sealing rig to evacuate the air and close off the quartz tube. Initially, the entire tube is evacuated to approximately 3×10^{-3}mbar and then backfilled with argon, and the entire process repeated three times, with the final back filling being to about 1/3 atmosphere of argon. A narrow flame is then used to cut through the thinned section of the quartz and remove it from the assembly, sealed under argon. Figure 3.2 shows the arrangement after cutting the quartz tubing.

A temperature growth profile is chosen depending upon the components and target compound, but typically involves rising to a high temperature, then slowly cooling to the final spinning temperature over several days to allow large crystals to form in the melt.

A complete list of the ∼400 growths attempted during this project can be found in Appendix B.

3.2 Challenges growing Iron Arsenide materials

3.2.1 Flux Choice, Equipment and Growing Conditions

Of the several families of iron arsenide high-temperature superconductors, the 1111 oxypnictides were found to be very difficult to synthesise in crystalline form using flux methods due to lack of suitable fluxes. Several attempts were made to synthesise SmFeAsO and CeFeAsO using Sn and NaCl:KCl fluxes, but single crystals were never attained. Other groups reported similar results, application of high pressures was found to be needed during the growth phase even to form tiny crystals. More recently, some groups have had limited success growing crystals of from a flux mixture, but sample properties are seen to vary strongly with sample

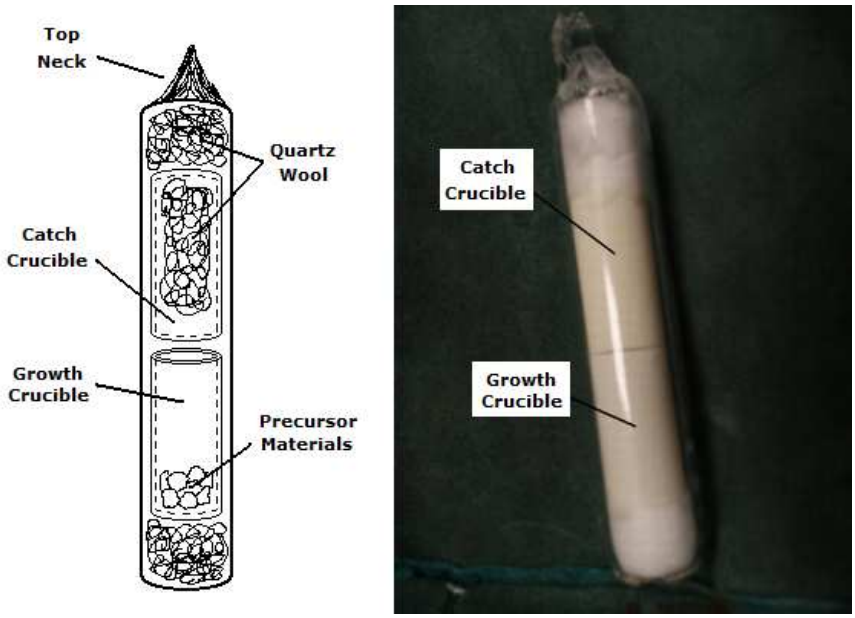

Figure 3.2: A schematic and a photo of a sealed growth ampoule. The diagram on the left shows the internal setup, with precursor materials in the lower 'growth crucible'. Crystals will form when the melt of these materials is slowly cooled in the furnace. The quartz wool in the upper 'catch crucible' will act as a sieve, separating the crystals from the melt when spun in a crucible. The photo on the right shows the final arrangement of a growth ampoule before heating.

quality [23].

Consequently, we have largely focussed on the 122 alkali earth iron arsenides Sr122 and Ba122 and doped variations of these. The fierce reactivities of both Strontium and Barium - and also Potassium, a common choice of dopant for Ba122 - to oxygen in atmosphere have presented several practical challenges. High quality potassium in particular is highly flammable in small quantities of oxygen and extreme care should be taken when using it, it should remain in an oxygen-free glove box at all times and any offcuts should be left in the glovebox to oxidise slowly over several days.

Initial attempts to follow the growth sequence described above led to large oxygen impurities. Barium and Strontium would discolour as they were cut and weighed, and barium samples would even warm noticeably as oxidation took place. Sr122 crystals made from this procedure frequently showed spurious superconductivity at temperatures around 20K (the parent compounds are not expected to superconduct down to 1K), probably due to chemical degradation from moisture [19].

First, a glove box was deployed to weigh and package material under an inert atmosphere. We tried sample growth packaged under argon, but still necked open to atmosphere as before. Unfortunately, these samples showed little improvement - the necking process heats the whole ampoule and would be expected to lead to rapid oxidation of the exposed material.

Several methods were tried for closing off the quartz tubing before necking took place, so that it could be done under argon. Rubber tubing was found to produce too poor a seal, and often was difficult to remove from the tubing after sealing. Also, necking under a sealed environment of argon requires a lot of care, as the trapped gas pressurises quickly as it is heated, and can cause the tubing to rapidly swell and burst. A variety of new procedures have been developed to deal with this, for example a sequence of custom-made brass quartz-balloon adaptors (figure 3.3) that maintained a sealed environment while accommodating slight pressure variations due to heating of gasses.

We have had customised rotaflow glassware and several brass sealing pieces made to enable the materials to be packaged and sealed in the glove box (figure 3.4), and flexible metal tubing and connectors to allow it to fit out of the

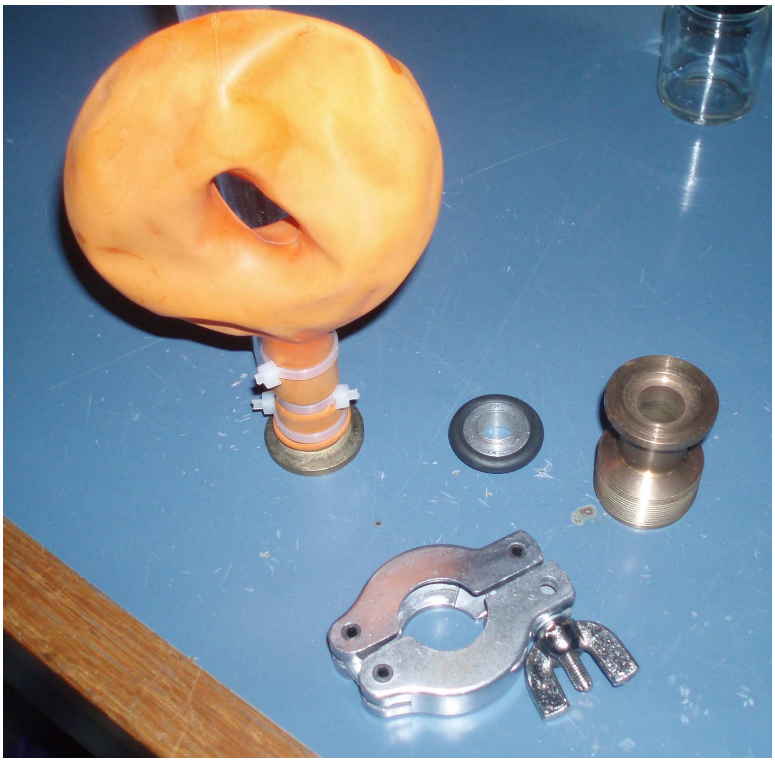

Figure 3.3: Our balloon adaptor for dealing with slight variations in pressure in a sealed environment due to heating

glove box atrium, before transporting to the sealing rig and pumping and flushing with argon. Recent samples have shown significant improvement, discussed in the next section.

Flux choice is also a significant determinant of sample quality. Initially, Sn-flux was used to grow crystals in a ratio of Sn:Sr/Ba of about 50:1 which had good morphological properties, and temperatures up to 1000 °C were found to be sufficient. However, this lead to tin impurities in crystals, which in particular had a large effect on Ba122 as reported in the literature [48]. Consequently, a move was made to a self-flux sample recipe. This involves using FeAs in excess as a flux - FeAs:Sr/Ba in a 4:1 ratio was found to produce good crystals. The ampoule was gradually heated to 1180 °C followed by cooling to 1020 °C at 2 °C/hr and spun. Maximum temperatures of 1180 °C were required by the self-flux recipe, moreover significant amounts of materials were used in each growth.

3.2.2 FeAs Pre-reaction

Initially, pre-reacted FeAs was purchased from industrial suppliers. However, high demand for this material led to price increasing by a factor of ten, becoming prohibitively expensive. Consequently, a pre-reaction technique was developed to grow our own FeAs. Since Fe and As are not air sensitive at room temperature and pressure, the glovebox was not required to seal these growths. However, arsenic is highly toxic and has a high vapour pressure at high temperatures, so the balloon piece described above (figure 3.3) was attached to the growths during sealing to prevent arsenic escape.

Approximatly 5g of Fe (powder, 99.998%, Alfa Aesar) and As (lumps, 99.9999%, Alfa Aesar) was mixed in a 1:1 stoichiometric ratio, heated to 1000 °C gradually with intermediate dwells at 500 °C and 800 °C to allow the arsenic to vapourise slowly, and held for 48 hours at 1000 °C. This produced a single large piece of small fused silver-coloured lumps. These were reground in a plastic bag inside our fume hood and resealed, and the same temperature profile was repeated.

This produced a silver powder which was found to give large, good quality crystals.

A significant safety concern is the stability of the quartz in the furnace at high

Figure 3.4: Custom-made glassware and brassware for sealing under inert atmosphere. The blue plastic piece is the 'rotaflow' value, attached via a brass demountable o-ring vacuum seal for quartz tubing, with another on the other end

temperature during these growths. A simple analysis using the ideal gas equation and assuming near-complete vapourisation of the arsenic indicates maximum pressures of up to 80bar. Although empirically the quartz tube was found to survive for our setup, the safety of this setup is a strong function of the strength and thickness of the quartz. During optimisation we had several accidents involving explosions of quartz tubes at high temperatures. These are very dangerous and risk toxic contamination of the furnace and surrounding areas. Consequently, both of our furnaces were always run in a sealed and negative pressure environment to remove any poisonous gasses.

3.2.3 Doping Samples

Initially, doping was attempted using Sn as a flux. However, doping was found to vary unpredictably between samples and when we stopped using Sn as a flux for undoped crystals we began to use a self-flux recipe for doped crystals too.

Unlike FeAs, we were unable to find an effective recipe to grow CoAs in the lab. Cobalt attacks the quartz used for the sealing and left a blue discolouration

on the silica and alumina. Consequently, CoAs (99.5%, Cerac) was purchased and used for these growths.

This was mixed with FeAs (pre-reacted) and Sr/Ba (pieces, 99.9%, ESPI) according to the ratio Sr:FeAs:CoAs = 1:4(1-x):4x, using all of the growth conditions discussed before. The ampoule was gradually heated to 1180 °C followed by cooling to 1020 °C at 4 °C/hr, at which temperature the ampoule was centrifuged to remove the liquid flux, crystals retrieved and stored under vacuum.

This cooling rate is significantly faster than the rate used for undoped crystals. We found that the level of doping was affected by cooling rate, with longer times leading to lower dopings as undoped crystal structures are thermodynamically preferred if given time to form.

We also attempted to dope crystals using K, which can lead to critical temperatures up to 40K. Due to the very strong reactivity of Potassium, this was very difficult. It attacked the quartz wool used in growths to sieve crystals during spinning, so we could not spin to separate crystals and flux. It also attacked the sealing quartz, often leading to the growth breaking up in the furnace.

The best way to solve the problem would be the deployment of an arc welder, which would allow the growths to be sealed in tantalum which is unreactive and stable but needs much higher temperatures to weld closed. At time of writing we do not have such a system, although one is under construction. We were eventually able to make crystals of KFe_2As_2 using an intermediate tantalum layer with an imperfect seal and very thick quartz to seal the outside, but the crystals were small and hard to separate from the flux without a spinning step. The very thick quartz required a very large flame to work with, which was both difficult and uncomfortable (and potentially dangerous should there be a crack and rapid oxidation of the potassium inside). Consequently, further attempts have been put on hold until the arc welder is ready.

3.2.4 Growing Large Crystals for Inelastic Neutron Scattering

A large amount of time was spent developing techniques for growing crystals for Inelastic Neutron Scattering (INS). In these experiments, neutrons are used to

Figure 3.5: The centrifuge used to spin our samples (left) and the two sets of brass moving pieces used for smaller and larger growths (right). Penny pieces were used to balance growths and quartz wool was used to cushion them during the spin. Samples were placed in the centrifuge from the furnace, and the centrifuge switched on. Once it had got to about 3000 rpm, which typically took 7 seconds, the centrifuge was turned off and samples left to cool.

Figure 3.6: Three different size of crucibles were used to grow INS crystals

probe the magnetic excitations of crystals. Because of their very low scattering cross-section, large amounts of single crystal are needed.

In general this can be achieved by scaling up the growth setup. A larger reaction crucible allows more space for crystals to grow and greater amounts of material allow larger crystals to form. However, larger quartz is much harder to work with effectively. Wider tubes need higher temperatures to neck, and are also much more likely to break during the process.

Figure 3.6 shows the larger growth setups used to grow these crystals. A significant increase in crystal size was seen moving from the small to medium setup. The increase in crystal size moving from the medium to large size was much smaller, although the increase in effort to set the growth up was significant. Consequently, the medium sized setup was our most commonly used setup for INS crystals. The increasing sizes of quartz also required larger moving parts in the centrifuge - figure 3.5 shows the centrifuge we used and the larger brass moving parts developed for INS crystals.

3.3 Characterisation

Being able to characterise samples is central to our ability to optimise our process. We have measured the resistivity and DC magnetisation of all of our samples being used for further measurements, and have developed collaborations to perform crystal x-ray analysis, electron microprobe analysis, heat capacity measurements and scanning electron microscopy on important batches.

3.3.1 DC magnetisation

We use a Quantum Design MPMS Superconducting QUantum Interference Device (SQUID) to measure magnetisation. A crystal sample is mounted on a straw and placed inside another straw for stability and protection. In order to fit the first inside the second it is slit lengthways and folded over. A slight variation of mounting technique allows for the crystal to be mounted with any axis either parallel or perpendicular to applied field (Figure 3.7).

The sample straw is placed in a magnetic field, which induces a moment on the sample depending on its susceptibility and orientation. The MPMS then moves the sample through a sequence of coils, generating a voltage proportional to the magnetisation of the sample, which can then be inferred by fitting the measured signal.

With magnetisation measurements, we were typically looking for one of two things. Firstly, we can look for the sample's characteristic Neel transition temperature. The 122 family undergoes a transition from high temperature tetragonal to a low temperature orthorhombic structure and adopts long range magnetic order with a resulting change in the magnetic susceptibility, but the signal is rather weak, so a large sample must be chosen. In practice we have found that the crystal should be at least 0.002g if a clear Neel transition is to be observed, and a field of larger than 1 tesla is required.

Many of our early samples showed a large Curie-Weiss background at low temperatures presumed due to impurities, particularly oxides. In order to reduce this effect, we first focused on the inert atmosphere sealing process described in section 3.2. We also developed the heating profile for our samples. To remove the oxygen from the homogenous liquid we incorporated a long dwell period

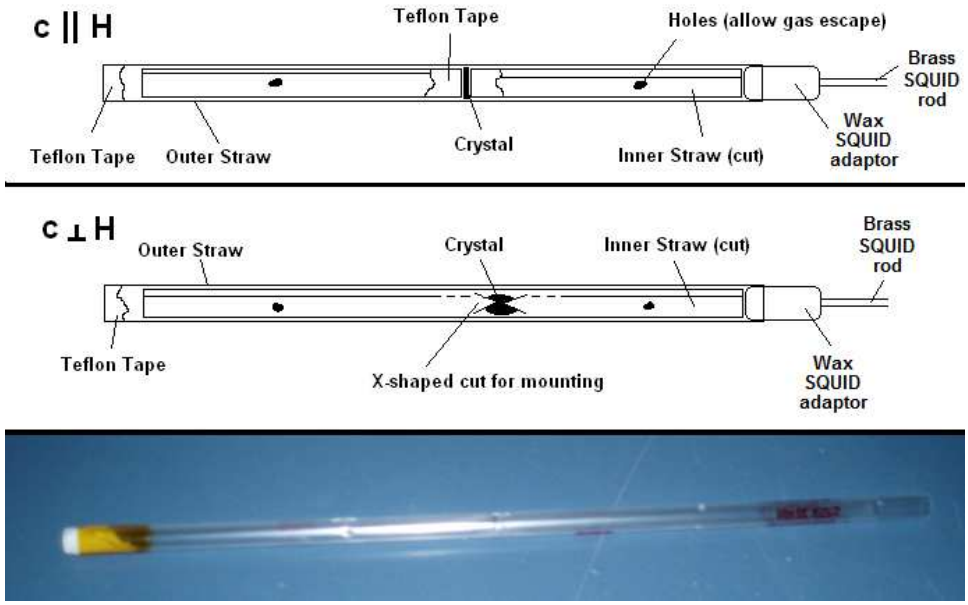

Figure 3.7: The upper diagram shows the procedure for mounting samples with c-axis ∥ H-field. An inner straw is cut down its length to fit into an outer straw, and cut in half. Each end is covered with a small amount of teflon tape, and the crystal is squeezed between these ends. For mechanical stability, and to allow oxygen to escape easily, holes are made with sharp tweezers about a quarter and three-quarters of the way along the outer straw. The lower diagram shows the procedure for mounting with c-axis ⊥ H-field. An inner straw is cut down its length, and an X-shaped cut is made opposite the cut. The crystal is wedged into this, and fitted into the inner straw, outward tension of the inner straw guarantees stability. Again, holes are made to allow gas to escape. The photo at the bottom shows an example of this mounting technique

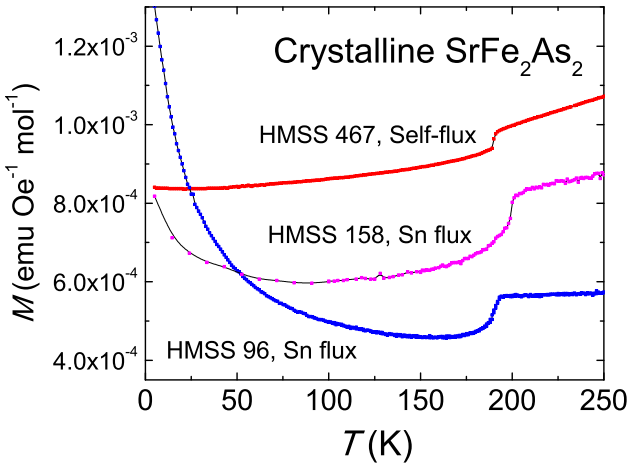

Figure 3.8: The variation of M vs. T with sample quality. HMSS number refers to the batch number of the crystal sample, lower numbers refer to earlier batches (see Appendix B for more details). These early crystals had a large Curie-Weiss tail, which was removed by increasing the dwell at high temperatures and moving to a self-flux recipe. This lead to monotonically increasing M with T, and reduced T_{N} to 192K (it was higher for many Sn-grown samples). Data offset for clarity.

at our maximum temperature, 1180 °C, before beginning a much slower cool down (which also allows larger crystals to form). Crystals from the more recent batches show much smaller impurity signals as well as a much more consistent Neel transition of 192K.

This is demonstrated by comparison in figure 3.8, a selection of three crystals of Sr122. The more recent growths have a much smaller impurity tail at the low-T end. The T-linear behaviour of magnetisation above T_{N} is strange and has been the subject of much discussion in the literature [30].

Secondly, due to the Meissner effect, magnetisation measurements provide a very sensitive probe of superconductivity. On becoming a superconductor, a sample will expel all magnetic flux and become a perfect diamagnet. This shows up as a strong negative voltage response, whose absolute magnitude can be used to calculate the fraction of the sample which has become superconducting.

Since inside a magnetic material (in cgs units),

$$4\pi M = \frac{\chi}{1 + D\chi} H_0 \tag{3.1}$$

and rearranging gives

$$\frac{\chi}{4\pi} = \frac{M}{H - 4\pi DM} \tag{3.2}$$

H is applied field, M is magnetisation and D is the demagnetisation factor between 0 and 1, dependent only on sample geometry (nb. some texts treat 4πD as the demagnetisation factor, and allow it to vary between 0 and 4π). This is 0 for an infinite slab of crystal with c-axis $\perp$ H-field, and 1 for c-axis $\parallel$ H-field. For our crystals, it is somewhere in between and cannot be determined with perfect accuracy. Further, full flux expulsion is not achieved in many samples due to flux pinning of vortices within the sample. These measurements therefore allow order-of-magnitude calculations of the magnetic susceptibility and hence superconducting volume fraction.

Due to the strong signal, very small samples can be used. Small fields are also preferable, as even low fields can sensitively suppress the superconductivity in type-II superconductors, including almost all non-elemental superconductors.

3.3.2 Resistivity

Resistivity of samples was measured on an Oxford Instruments custom-built helium flow cryostat configured for resistivity measurements shown in figure 3.9. Samples were mounted onto a probe using 4929 silver paint and 50-micron diameter gold wires to make four-point contacts as shown in figure 3.10 and cooled, with in-plane resistance measurements carried out using an excitation current of 50μA at a frequency of 77.7Hz.

Four-point contacts are vital for conducting samples, whose intrinsic resistance is small compared to that of the contacts between sample and wire (typically $\sim$1 Ohm). A two-point contact measures the resistance of the wire + contact + sample, which is much larger than the sample's resistance. In a four point measurement, separate leads are used for current and for measurement of potential

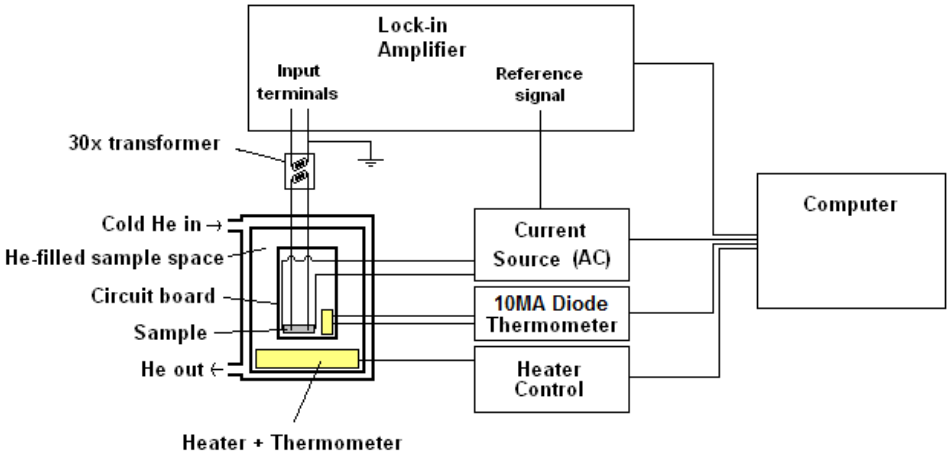

Figure 3.9: The configuration used to measure sample resistance. The probe allows two samples to be mounted simultaneously with current running in series and a second lock-in amplifier used for the second voltage measurement. The inner sample chamber contained He exchange gas and was sealed from the outer chamber through which cold He was circulated directly from a dewar. User-entered values on the computer controlled heating rates; cooling rates were determined by the helium flow but could be partially controlled using the heater to reduce cooling rate if helium flow rates were large enough

drop, so that only the potential drop over the part of the sample between both current and voltage terminals is measured.

The process is made difficult by the mechanical weakness of the silver paint which often fails at low temperatures. Other methods of making contact such as spot welding and thermally setting glues were tried, but we observed that the crystals both oxidise and give off Arsenic when heated, going off stoichiometry. Consequently a room-temperature method of making contacts was preferred. Despite the weakness, the method allows a resistivity ratio to be measured to give some idea of sample purity and also highlights any transitions.

These samples were found to cleave very easily along their ab-planes. This allowed for thin, bar-like samples with cleaved surfaces to be used for measurements, which is preferable. However, it was also found that even normalised resistivity measurements were quite variable, as found in other studies [68]. This is assumed to be due to inter-plane cleaves leading to an unpredictable geometric factor for current flow. Indeed, on some resistance sweeps resistance was seen to

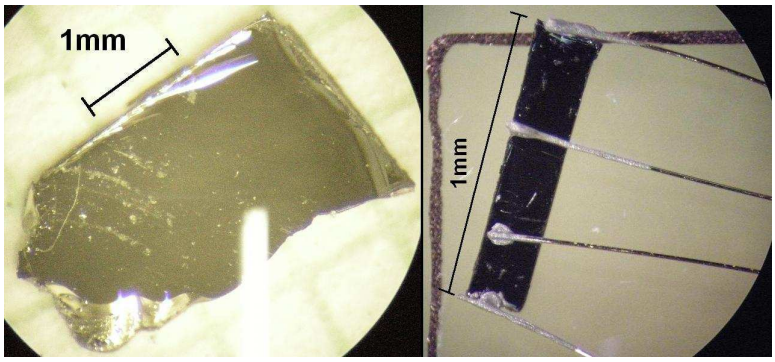

Figure 3.10: The crystal on the left is an as-grown crystal sample of Sr122. The c-axis can be seen clearly, although the a- and b-axes are less easy to determine. It has been cut along the top right side, and spontaneous cleaves can be seen here. The crystal on the right is a cut and cleaved sample mounted for a four-point resistance measurement. The current flows through the outer two leads, and potential drop is measured over the inner two. A bar-like morphology with a length $\gg$ width is preferred for these samples to force current to flow uniformly

jump sharply at some point on warming before continuing at some multiple of the resistance previously measured on cooling, due to an internal thermal cleave.

Typical resistivity ratios R(273K) / R(5K) for these crystals are about 2. In very pure samples of some types of metals ratios of 500 or more are possible, so this low ratio suggests that there is a lot of disorder in the crystal structure. However, direct comparison of these ratios is complicated by carrier densities, and observation of quantum oscillations means that a reasonable electron mean free path is achieved. This discussion is continued in subsection 3.3.5.

3.3.3 Heat Capacity

Heat capacity of samples was measured using an Oxford Instruments Physical Properties Measurement System (PPMS). This uses a relaxation method to measure heat capacity indirectly, where a pulse of heat is used to warm the sample, and the time to decay back to its initial temperature is measured. The heat capacity is a factor in the decay constant, and can be inferred from this measurement by the system. Although a direct method of measuring heat capacity (where a known amount of heat is added and the temperature change measured) can in principle be more accurate, it requires large samples and very good thermal

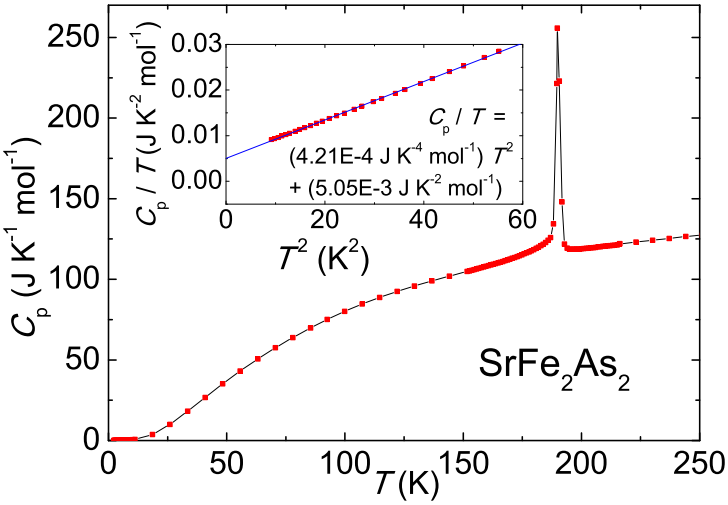

Figure 3.11: C_p vs. T for a sample of Sr122. The high-T structural/magnetic transition gives a large peak in C_p at 189K. This measurement involves heating over a range of about 2K so is effectively an average - a finer measurement with narrower heating ranges shows an even sharper peak (see, for example, figure 4.10). The inset shows C_p/T vs. T^2 for the low-T data, from which the Sommerfeld coefficient can be extracted

isolation, as well as corrections for radiative losses. By contrast, the relaxation technique allows for quick measurement of fairly small samples with a good accuracy.

Heat capacity is a thermodynamic probe, and gives us several useful pieces of information. High temperature transitions lead to large increases in entropy, seen as a large spike in the heat capacity around the transition. This is seen in figure 3.11, the heat capacity of a sample of Sr122.

From fitting low-temperature data other variables, such as the Sommerfeld coefficient and the Debye temperature(s) can be estimated, typically using the expected form for a free-electron metal

$$\frac{C_p}{T} = \gamma + \beta T^2 \tag{3.3}$$

3.3.4 Scanning Electron Microscopy

A Scanning Electron Microscope can be used to give some idea of surface morphology and composition, as well as possible contaminants.

As well as producing very detailed surface images showing the typical size of surface flux inclusion, an SEM running in Energy Dispersive X-ray Spectroscopy (EDAX) mode can give an idea of the composition of a sample from the x-rays emitted on electron bombardment of the surface (although data is not quantitatively accurate, unlike EPMA discussed below). This allows contaminants to be identified and a rough degree of the amount of flux within the crystal to be established.

A typical SEM image of one of our crystals, here chosen to demonstrate some of the effects mentioned, is shown in figure 3.12.

3.3.5 Crystal X-Ray Diffraction

X-ray diffraction is a standard method for measuring crystal structures from the Bragg scattering that they produce on x-ray irradiation. The more common method uses a powdered sample of crystalline materials. Because of the random alignment of the powdered samples, it shows all of the separate Bragg peaks in a sample. However, a significant amount of the sample is required. These measurements were taken in collaboration with Jacqui Cole (see acknowledgements).

We used single-crystal X-ray diffraction to confirm the structure of a sample of Sr122. This requires a much smaller sample - we used a 300 x 275 x 60 μm crystal mounted on a Rigaku SCX mini diffractometer in the Cavendish, equipped with an Oxford Cryosystems nitrogen cryostream. This can hold the temperature constant (we performed the measurements above and below the Neel transition temperature) while the crystal is rotated through 180° and a Bragg image taken every degree.

Unit cell parameters were determined above and below the Neel temperature at $T = 220$K and 155K. Our results were consistent with a tetragonal structure above the transition and an orthorhombic structure below. A particularly interesting feature of the diffraction patterns is the characteristic V-shape of the peaks, shown in figure 3.13. This indicates that there is some type of 2D disorder

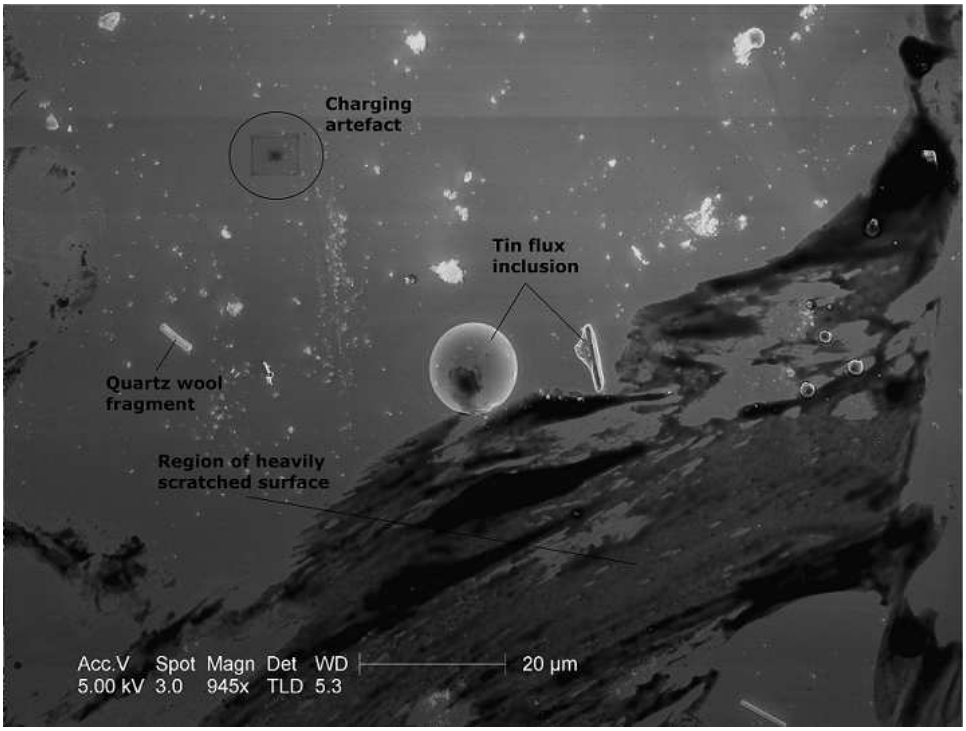

Figure 3.12: An SEM image of a part of our sample surface. The darker lower area shows surface faults due to scratching, and the large circle in the middle is tin flux inclusion on the surface. The white line on the middle left is a small piece of quartz wool. All of these can be removed by cleaving the crystals. The darker square in the top left is a relic of the SEM imaging. we looked more closely at this part and charge from the microscope built up, indicating that either the crystal is only semi-metallic, or that the electron beam is having an effect on the crystal structure

in the 3D crystal structure. One possibility is that there is a substitution effect happening, with the Iron and Arsenic atoms exchanging places in the crystal. Their ionic radii are less than 1% different so that swapping wouldn't put a great mechanical stress on the structure. Since superconductivity in these compounds is thought to be confined to the FeAs plane, we might well expect such substitution to strongly affect superconducting characteristics. It might also explain why the resistance ratios described above were so low, since swapped atoms would reduce electrical mean free path in the compound.

3.3.6 Electron Microprobe

We used a Cameca Electron Probe Microanalyser (EPMA) equipped with 1 EDS and 5 WDS spectrometers in the Department of Earth Sciences operating at 15keV to determine the composition of some samples. Mounting and measuring samples is a time-intensive process so only a selection of samples were analysed. The probe bombards the sample with energetic electrons, which causes it to emit X-rays that are characteristic of the elements present, and allow a quantitative calculation of the stoichiometry. A typical example of a resulting homogeneity map is shown in figure 3.14.

Samples were cleaved in atmosphere, then mounted on sticky carbon tape for probing. Typically insulating samples must be mounted in a resin, polished, and coated with a thin graphite layer to allow electrons to leave the sample and prevent charging causing artefacts. However, our samples were highly conducting and no difference was detected within experimental resolution between samples coated in graphite and those not, so for the majority of samples the more simple technique was used. Pyrite, Celeste, Cobalt metal and Arsenopyrite were used as standards to calibrate spectra. It should be noted that electrons in EPMA cannot go further than about ten lattice spacings into crystals due to their strong electromagnetic scattering cross-section, so this is a surface rather than bulk probe.

For each sample, a selection of 20 random points was chosen to scan. A typical dataset is shown in table 3.1. Datasets were averaged and used to calculate atomic formulae. Note in addition to doping the slight variation away from ideal

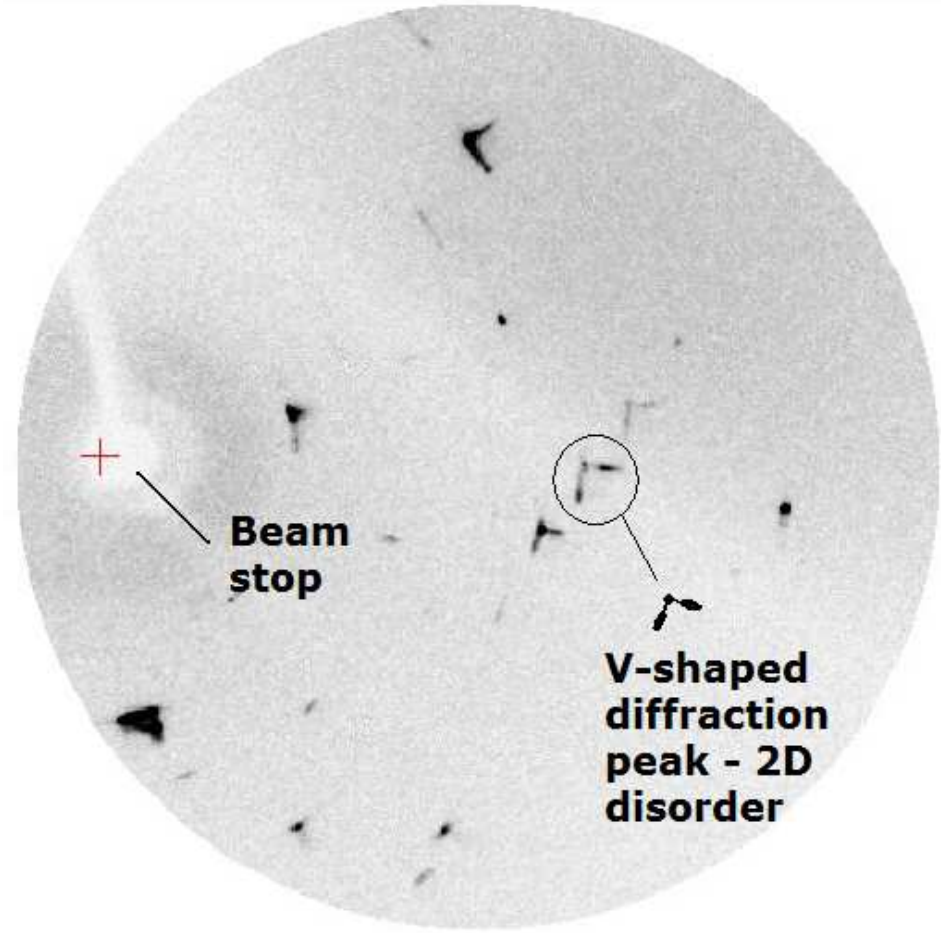

Figure 3.13: A Bragg image at a particular angle at $T = 155$K. We can see the diffuse scattered V-shaped peaks indicating some type of 2D disorder, most likely in the FeAs planes due to the similarity in Fe and As ionic radius. A reduced version of this image is featured in ref. [2]

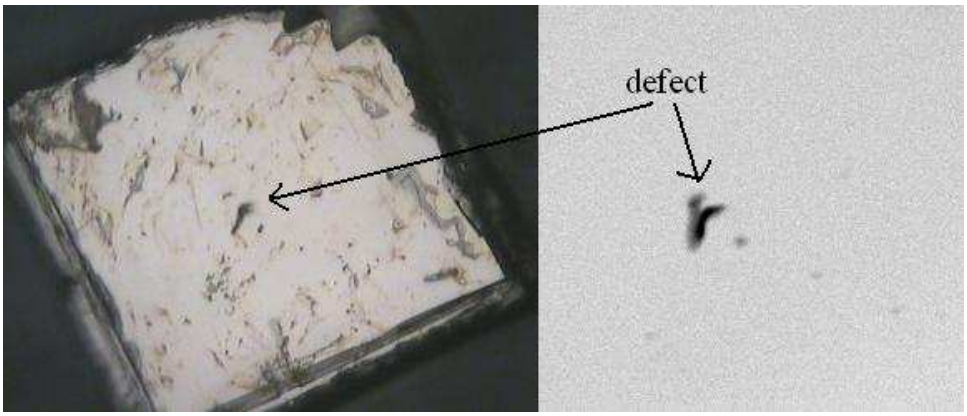

Figure 3.14: An image of a microprobed sample (left) and a homogeneity map (right). The black mark on the right image is the surface defect that can be clearly seen in the middle of the imaged crystal. Elsewhere the phase of the crystal is homogeneous across the surface.

stoichiometry of Sr (here just under 1% deficient) and sometimes As, common to most samples measured.

Table 3.1: EPMA measurement of 20 points in a nominally 11%-doped sample

Point	Strontium %	Iron %	Cobalt %	Arsenic %
1	19.8	36.4	3.69	40.0
2	20.0	36.4	3.84	39.8
3	19.9	36.3	3.74	40.0
4	19.9	36.5	3.69	39.9
5	19.9	36.3	3.75	40.1
6	19.9	36.3	3.67	40.1
7	19.8	36.5	3.78	40.0
8	19.8	36.3	3.79	40.0
9	19.7	36.4	3.81	40.1
10	19.7	36.6	3.78	40.0
11	19.7	36.4	3.76	40.1
12	19.6	36.6	3.70	40.1
13	19.8	36.6	3.66	40.0
14	19.9	36.4	3.72	39.9
15	19.7	36.4	3.73	40.2
16	19.9	36.2	3.79	40.1
17	19.6	36.5	3.82	40.1
18	19.7	36.4	3.81	40.0
19	19.9	36.3	3.78	40.0
20	19.7	36.3	3.78	40.2
average	19.8	36.4	3.75	40.0
formula	$Sr_{0.991}(Fe_{0.910}Co_{0.093})_2As_{2.00}$			

Chapter 4

The Phase Diagram of $Sr(Fe_{1-x}Co_x)_2As_2$

4.1 Superconductivity in the Iron Arsenides

The phase diagrams of superconducting materials are often of considerable interest. A striking feature in common between iron pnictide, cuprate, and heavy fermion superconductors is the proximity of superconductivity to magnetism. In many cases, a high temperature magnetic transition is suppressed to lower temperatures on the application of a tuning parameter such as doping, pressure or magnetic field. Eventually the transition is suppressed to 0K, at which point a quantum phase transition must take place as the tuning parameter is varied, with entropy fixed. One ordered state must give way to another, frequently this is superconductivity.

In the 1111 [25] and 122 [55] families of Iron Pnictide superconductors, the undoped material is an antiferromagnet which follows exactly this pattern, evolving into a superconductor upon doping. The manner in which magnetism evolves into superconductivity is of particular interest, especially whether a quasicontinuous magnetic phase transition is involved.

The 122 system has attracted interest due to the appearance of superconductivity either by chemical (hole- [55] or electron- [4; 49; 60]) doping; or by applied pressure [2]; and the relative ease with which large crystals can be grown.

Co-doped Ba122 has been well studied [1; 12; 50]; exhibiting superconducting temperatures up to ≈24K. The single magnetic and structural transition in the undoped compound is observed to split into separate magnetic and structural transitions at higher doping and has been followed into the superconducting state via x-ray experiments, with superconductivity found in both the orthorhombic and tetragonal states [47].

The Sr122 system has also been explored in polycrystalline samples [35], where critical temperatures of up to 19K are observed. Measurements on single crystals of these materials are difficult due to the development of rogue superconductivity at about 20K in samples exposed to air. Various mechanisms have been suggested for this, including surface reaction [19] and instability to lattice distortions [58]. Consequently, it is vital to work with freshly prepared samples and keep them in vacuo between measurements.

4.2 Synthesis and Measurement

To investigate the phase diagram of Co-doped Sr122, I grew single crystals of Co-doped Sr122 and Co-doped Ba122 of up to 5mm × 5mm × 0.5 mm as described in chapter 3. The exact procedure used for sample synthesis was as follows:

1) FeAs and CoAs were mixed in the ratio mentioned in section 3.2.3 on the bench, and added to a crucible. These crucibles were moved into an argon-filled glovebox, where Sr was added to complete the mixture.

2) The crucible was put inside a quartz tube with outer diameter approximately 17mm along with an upper catch crucible. Quartz wool was placed above and below the crucibles to cushion them. The balloon adaptor shown in fig. 3.3 was used to seal the growth tube.

3) The whole setup was removed from the glovebox and necked with a medium blue hydrogen-oxygen flame just above the upper quartz wool to a thickness of about 6mm (the balloon adaptor allows the setup to change slightly in volume to accommodate pressure due to gas heating).

4) The setup was returned to the glovebox, where the balloon adaptor was removed, and replaced by a closed 'rotaflow' valve (figure 3.4). This was then removed from the glovebox and connected to the pumping rig.

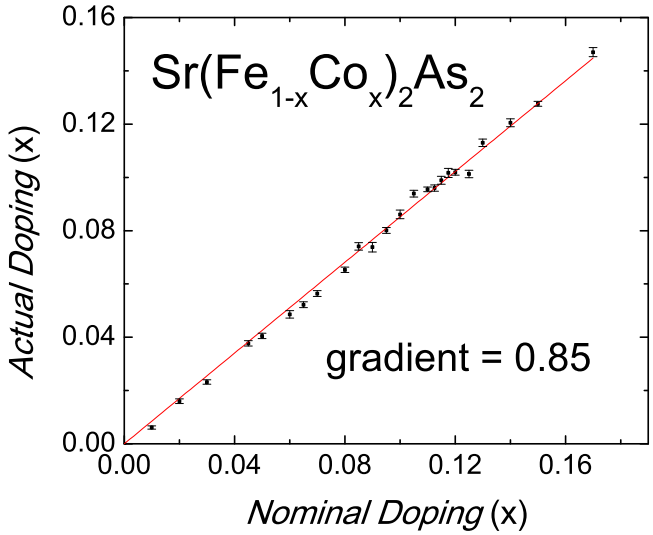

Figure 4.1: The nominal-to-actual doping, measured by electron microprobe analysis of the surface of cleaved samples. Actual doping is an average of 20 points, with the error bars given by the n-1 standard deviation. The red line shows a linear fit to the data

5) Once attached and pumping, the rotaflow valve was opened to pump on the growth. It was pumped to low pressure and flushed with argon three times to ensure low levels of residual oxygen.

6) Finally, it was refilled to 1/3 bar argon and the quartz neck was closed off with a small blue flame.

7) The ampoule was heated in the furnace using the profile mentioned before. Afterwards it was spun while hot, allowed to cool and broken open to retrieve crystals. These were stored in a large vacuum desiccator between measurements to prevent degradation due to atmosphere.

Samples were characterised in Cambridge via electrical resistance, magnetisation and EPMA measurements as described in section 3.3. A collaborator also measured the heat capacity of a selection of samples using the same technique described in this report.

Crystals with nominal doping levels of Co in the range $0.00 < x < 0.19$ were grown. Variation of Co doping within a crystal was found to be small and almost independent of doping, remaining less than 2% for the majority of

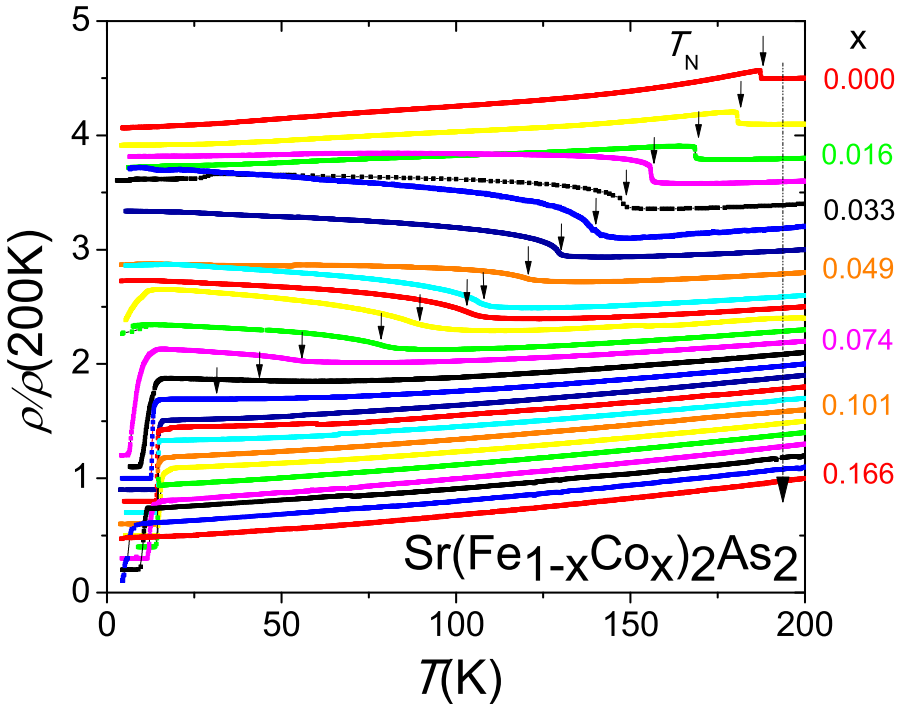

Figure 4.2: The electrical resistivity (ρ/ρ_{200K}) as a function of doping in Co-doped Sr122 from $x = 0$ to $x = 0.166$. Data are normalised to the resistivity above the Neel transition in all samples, and for clarity, data for the various dopings is offset. T_N (defined as the point of greatest negative slope in the resistance) is indicated by arrows. Representative x values are given to the right of some resistance sweeps.

samples and ∼10% for the lowest doping, as shown in figure 4.1. No difference was detectable between different crystals from the same batch within these limits, and actual doping was found to vary roughly linearly with nominal doping with coefficient ∼0.85. No impurity phases were observed. Annealing of some samples was performed by heating to 850 °C followed by a 48 hr dwell under argon or in vacuum, followed by cooling to room temperature.

Undoped samples of Sr122 show a structural and antiferromagnetic transition at T_N=192K (seen in resistance, figure 4.2, and magnetisation, figure 4.4). On Co-doping, this transition is suppressed, with T_N eventually disappearing (the point of disappearence is captured by the resistance profiles shown in figure 4.5, accompanied by the onset of superconductivity at x=0.075, extending from x = 0.075 to 0.144, with the optimal superconducting temperature occurring at

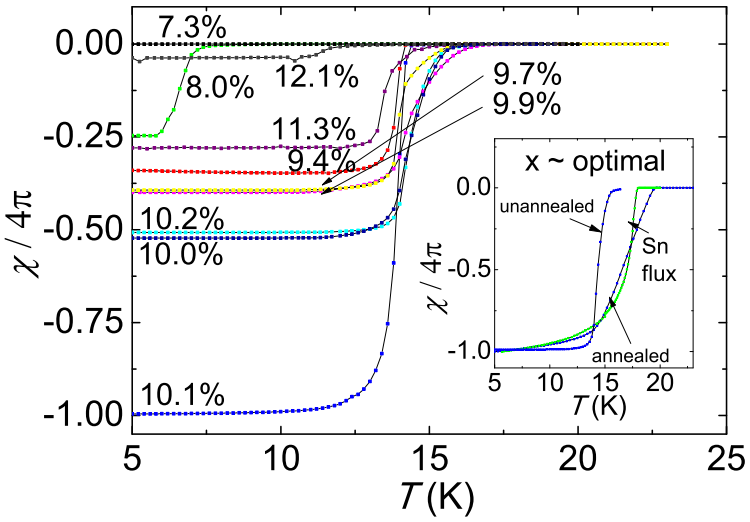

Figure 4.3: Shielding in DC magnetisation corresponding to the development of superconductivity with doping ($\chi/4\pi = M/H$). All measurements were performed in a 50 Oe field applied parallel to the c-axis of the crystal after zero-field cooling. The volume fraction reflects bulk SC in all cases, and has been renormalised to 1 for the highest volume fraction for purposes of comparison. T_c is defined as the point of greatest negative slope in the magnetisation. Inset: magnetisation for annealed and Sn-grown cobalt-doped samples with close to optimal x show higher onset T_c and a broader transition compared to the unannealed sample (volume fraction has been renormalised to be equal).

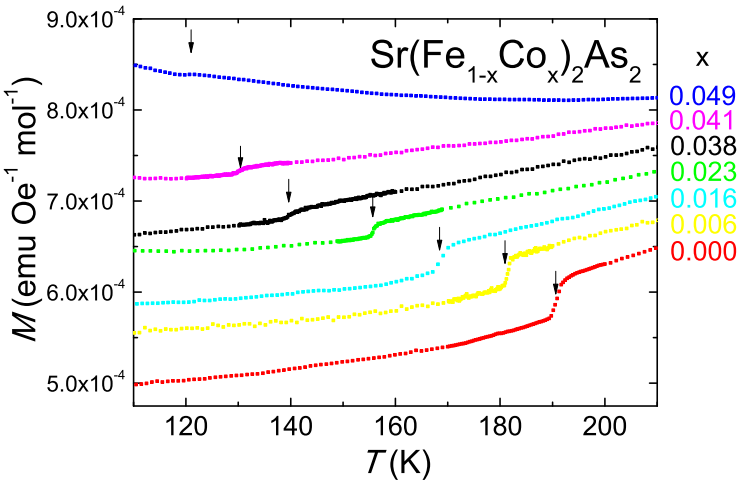

Figure 4.4: The suppression in T_N as seen at 5T in a DC SQUID magnetometer. Beyond 5% doping the transition cannot be resolved by these methods, although it can be followed further by heat capacity and resistance measurements. Although there is a slight smearing of the transition, the transition width (as defined by derivative FWHM) is no more than 2K in all cases

$T_c \approx 16$K for x=0.102. The superconducting transition can also be seen in heat capacity. Figure 4.6 shows the entropy redistributed to the superconducting transition region in a near-optimally-doped sample.

Annealing is seen to have a rather interesting effect on Sr122 and Ba122 samples. The chief effect of annealing by the procedure described above is to reduce the in-plane resistivity of samples at most temperatures. The residual resistance ratio (RRR), defined here as R_{200K}/R_{4K}, increases with annealing for non-superconducting samples (for example, an increase from ≈2 to ≈20 is seen in figure 4.7 for undoped Sr122). Annealing also increases T_N from 192K to 200K in undoped samples along with the suppression in the upturn in the resistance at the antiferromagnetic transition before a rapid drop in resistance at lower temperatures. In doped samples, T_N is raised by several degrees on annealing (figure 4.8). Rather surprisingly, T_c is also enhanced by annealing - more closely resembling previously reported values for polycrystalline samples [35] - accompanied by a noticeable broadening of the superconducting transition (figure 4.3).

Microprobe analysis reveals a loss of Sr on annealing, with annealed samples

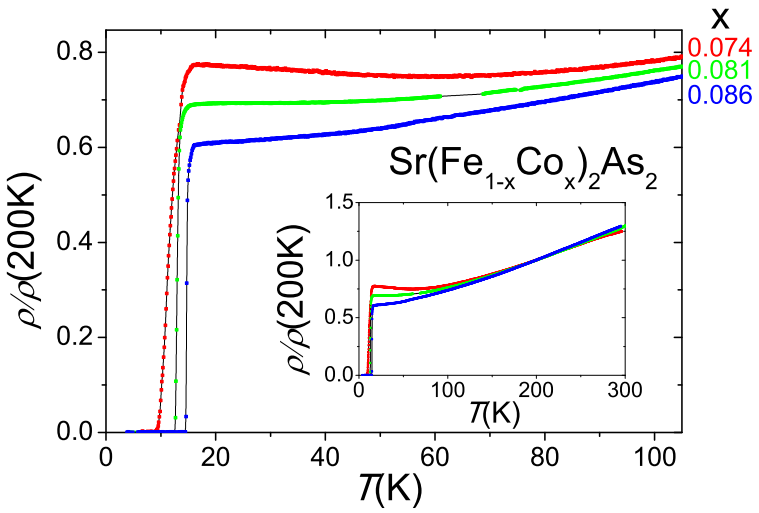

Figure 4.5: At low dopings, the Neel transition is marked by a sharp upturn in electrical resisitance. Assuming that this remains true at higher dopings, the critical doping at which the Neel transition is suppressed into the superconducting dome is revealed by detailed resistivity measurements to occur between 8.0% and 8.6% doping

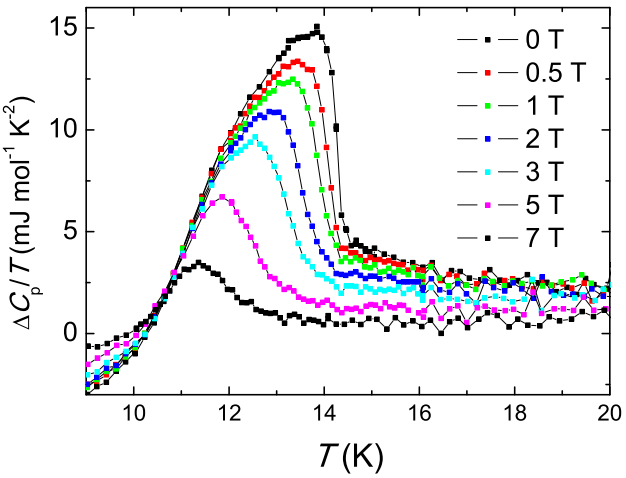

Figure 4.6: The suppression of the C_{p}/T superconducting anomaly in a near-optimally doped sample of Co-doped Sr122 by increasing magnetic field. The value of C_{p}/T at a 9T field (the highest accessible for these measurements, by which point the transition entropy, although not superconductivity, is largly suppressed) was used as a background subtraction for each measurement

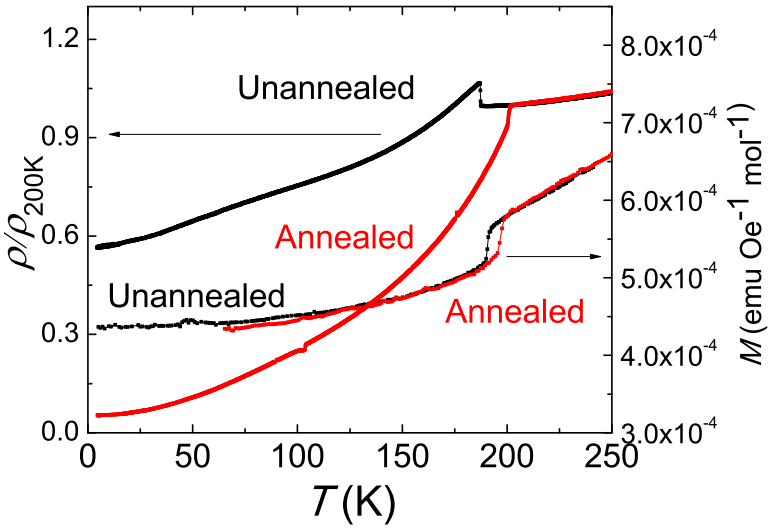

Figure 4.7: Here we show the effect of annealing on a typical undoped Sr122 crystal. R_{200K}/R_{4K} is improved and T_N is increased. Magnetisation also shows the increase in T_N, indicating that this is a full-volume effect. Magnetisation data for annealed sample is offset by a constant for comparison with unannealed data.

characterised by Sr-deficiency of up to 10%. A similar broadening of T_c is seen for samples grown out of Sn flux (figure 4.3), with an enhancement of T_c accompanied by a broadened superconducting transition. Sn impurities are known to substitute for Sr(Ba) in Sr(Ba)122 [65], with a similar effect to the loss of Sr (the 'spacer' in-between the superconducting FeAs planes) on annealing. Possible consequences of this inter-plane depletion of Sr ions include effective electron-doping (similar to K-substitution [55]), a disturbance of the antiferromagnetic nesting, effective uniaxial strain [31], or a reduction in the Coulomb repulsion [29]; all of which could be reasons for the enhancement in superconducting temperature.

4.3 Phase Diagram and Discussion

Figure 4.9 shows a phase diagram for Co-doped Sr122 constructed from measurements of resistance, heat capacity, and magnetisation. The magnetic/structural transition temperature is obtained from the sharp feature in resistance (fig. 4.2)

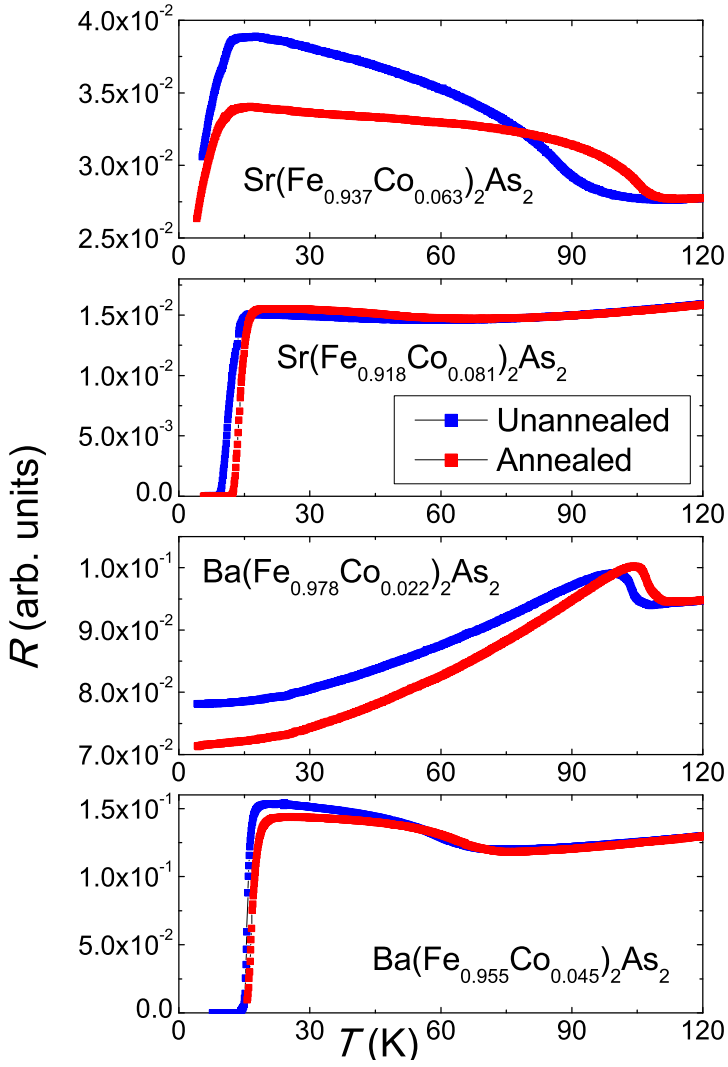

Figure 4.8: The effect of annealing on the resistivity of several Co-doped samples from the Sr122 and Ba122 families. Annealing raises the transition temperatures of magnetic and structural transitions, although the detailed effect appears rather complex. It does seem, however, that lower doped crystals are affected more by the annealing process

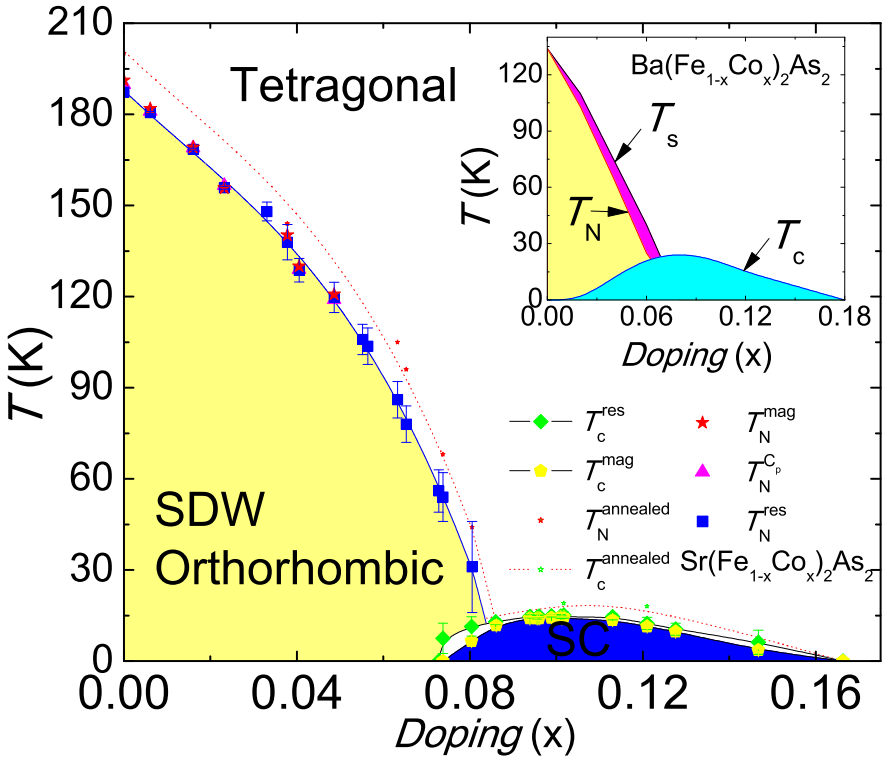

Figure 4.9: The phase diagram of Co-doped Sr122 measured from magnetisation, heat capacity and resistivity. The upper dashed lines correspond to higher Neel and critical temperatures for annealed samples (nb. NOT splitting of the transition in a single sample as seen in doped Ba122). The inset shows a schematic of the phase diagram of Co-doped Ba122 constructed from our measurements and previous reports [12; 50]. The purple region between the structural and magnetic transitions that occurs in Co-doped Ba122 is not seen in Co-doped Sr122

– traced up to the doping where the superconducting dome onsets, and from the sharp drop in magnetisation and the peak in heat capacity (fig. 4.10) – both of which are traced to lower dopings x=0.045, after which point neither probe is able to detect a transition. The superconducting transition temperature is obtained from the drop to zero resistance (fig. 4.2) and the occurrence of superconducting screening in magnetisation (figure 4.3). While the phase diagram of Co-doped Sr122 is superficially similar to Co-doped Ba122, vital differences are introduced due to the chemical tuning from Ba to Sr.

The optimal T_c in Co-doped Sr122 is only ≈70% of the optimal T_c in Co-doped Ba122 (ref. [6], fig. 4.9) while T_N is over 40% higher. The region of magnetism in Co-doped Sr122 is further separated from the region of superconductivity, with less overlap - occurring only between 7.5% and 8.5% in Co-doped Sr122 as compared to the region between 2.5% and 6% in Co-doped Ba122. These observations broadly support the notion that magnetism and superconductivity are competing in these materials, and the stronger magnetic order in Sr122 leads to superconductivity developing only at higher dopings and lower temperatures.

Interestingly, on careful inspection there is no resolvable splitting between the magnetic and structural transitions in Co-doped Sr122. Figure 4.10 shows the C_p transition at various Co-dopings in Sr122 (The heat capacity data presented in this diagram was measured in Spain by Jose Espeso, as mentioned in acknowledgements). A comparison is made at a representative doping of Ba122 (chosen for a similar % suppression of T_N), which reveals a distinct splitting in the transition, much commented-upon in the literature. An absence of splitting in Co-doped Sr122 due to a smearing of the two transitions is ruled out by the greatly reduced width of the single transition in Co-doped Sr122.

The nature of the magnetic transition in Co-doped Sr122 is compared with that in Co-doped Ba122 by a study of the entropy change associated with the transition. Figure 4.10b) shows the integrated value of C_{mag}/T (red lines) as a function of temperature for Co-doped Sr122 and Co-doped Ba122, where C_{mag}/T= (C_p - C_{nonmag})/T. Here C_{nonmag}/T is obtained from the measured C_p in a higher doped sample without a magnetic transition. The blue peak is the local value of C_{mag}/T. Whereas the entropy change at T_N in Co-doped Sr122 shows a significantly more abrupt near-vertical change, consistent with the latent heat involved

at a largely first order transition - the entropy change at T_N in Co-doped Ba122 shows a more gradual change with an extended shoulder characteristic of a quasicontinuous transition.

I also calculate the excess entropy of transition for the parent compound Sr122, as shown in figure 4.11. This figure will be a useful reference for our later study of the structural transition.

The difference between the magnetic and structural transitions in Co-doped Sr122 and Ba122 is important, and the differences between the phase diagrams can be associated with them. The quasicontinuous magnetic transition in Co-doped Ba122 occurs several Kelvin lower than the structural transition. In contrast, enhanced interlayer coupling in the more three-dimensional Sr122 leads to a higher magnetic transition that coincides with the structural transition to yield a single transition. Models that attempt to explain the splitting between magnetic and structural transitions in Ba122 and the 1111 family [16; 41] have also discussed the effect of increased interlayer exchange as reducing the splitting between magnetic and structural transitions. While the application of external pressure was suggested as a way to tune the splitting, this shows that chemical tuning, by replacing Ba with Sr to increase the dimensionality of the 122 material in question, is an effective way of achieving this tuning.

The first-order nature of the simultaneous magnetic/structural transition we observe in Co-doped Sr122 can be explained from symmetry as a consequence of the simultaneous occurrence of an Ising structural transition and an XY antiferromagnetic transition [26]. The first-order character of the transition in underdoped 122 materials where the magnetic and structural transitions coincide [32] has been characterised in detail, and the precise nature of the transition revealed by the TEM measurements of one of our collaborators (ref. [40], discussed later in section 6.3). Further, in contrast to the onset of the in-plane anisotropy in resistance in detwinned Co-doped Ba122 above T_s and T_N [11] indicating fluctuations of the order parameter, these fluctuations are truncated in Co-doped Ca122, which exhibits a strongly first order transition in the undoped material [38].

This suggests that enhanced interactions at the split quasi-continuous transition in the lower dimensional Ba122 lead to enhanced superconducting temperatures, compared to the single first-order transition in higher dimensional Sr122,

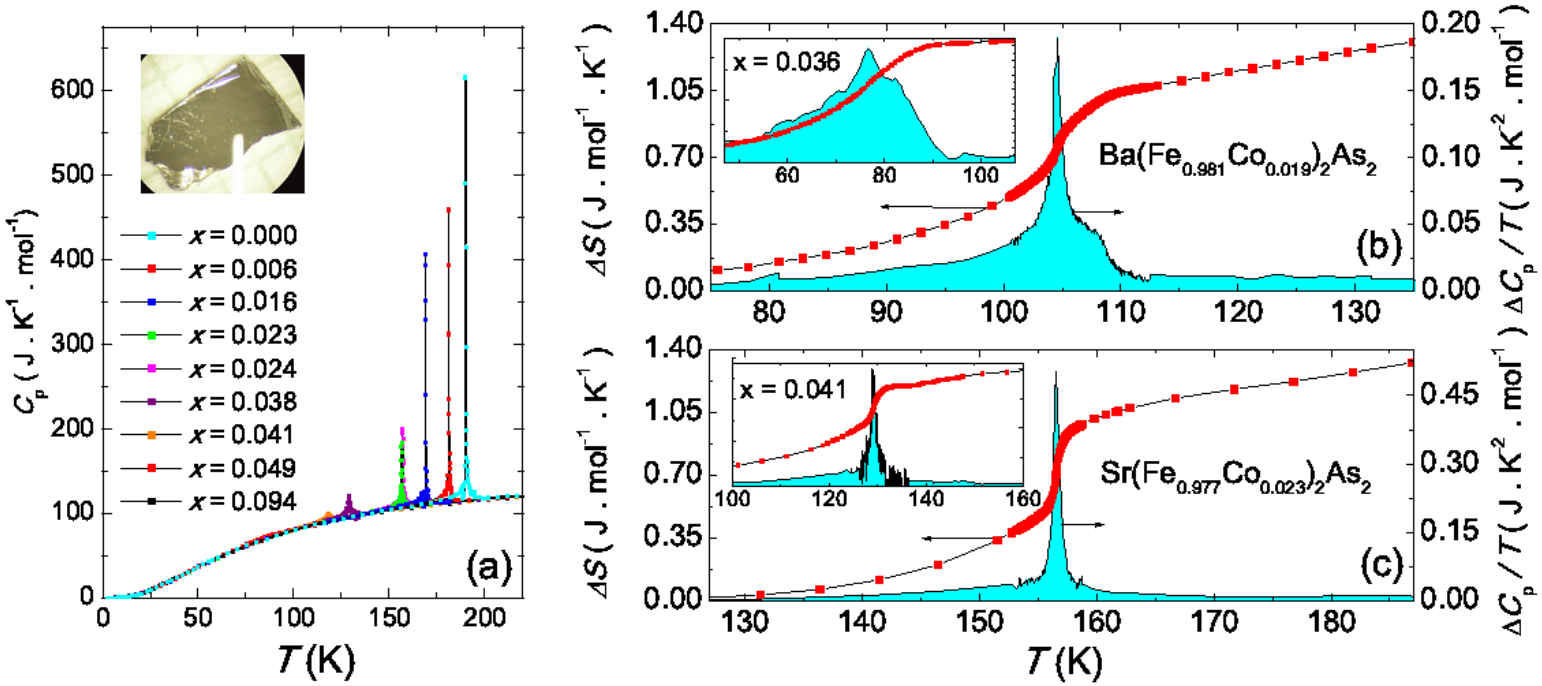

Figure 4.10: a) shows the heat capacity for a series of Co-doped Sr122 samples. Because of the narrowness of the transition, a temperature rise of only 0.3% was used for each measurement in the vicinity of the transition. The magnitude of the heat capacity jump at the magnetic transition falls with doping until it is unobservable at x=0.063. b) and c) show a comparison of the entropy and heat capacity jumps for 1.9% Co-doped Ba122 and 2.3% Co-doped Sr122, as described in the text. Dopings for comparison of Ba122 and Sr122 are chosen to correspond to a similar percentage suppression of T_N. The transition in Co-doped Sr122 is seen to be much sharper and more first-order-like than in Co-doped Ba122. The insets are similar data for higher doped 3.6% Co-doped Ba122 (data taken from ref. [12]) and 4.1% Co-doped Sr122 respectively, showing increased broadening in the Ba122, while the Sr122 remains sharp and first-order-like.

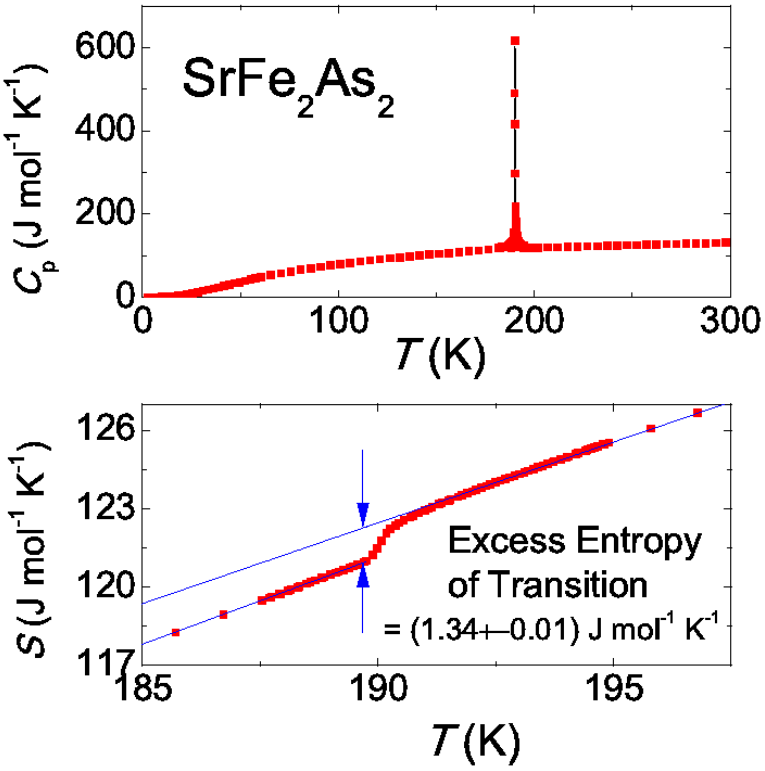

Figure 4.11: The upper panel shows the sharp first-order-like transition in Sr122 near to 190K. The lower panel shows the entropy jump on transition, and by fitting the data above the transition I calculate the excess entropy of transition. Since excess entropy also varies below the transition (according to equ 5.6, next chapter) it is important to measure as close to the lower end of the transition as possible

where T_c is suppressed, and the magnetic and superconducting domes further separated. My finding in the 122 family of materials is of relevance to the broader class of pnictide superconductors, such as the 1111 family, where reduced dimensionality and increased splitting between magnetic and structural transitions are accompanied by higher superconducting transition temperatures.

To further probe the nature of this transition across doping in both Co-doped Sr122 and Ba122, a probe that couples to magnetoelastic deformations is required. It has been proposed that such resonant elastic measurements should be able to distinguish between the several possible classes of transition, and allow the construction of a phenomenological Ginzburg-Landau model [7] for the structural transition explaining its coupling to magnetism. These measurements are the subject of the next chapter.

4.4 Pressure Effects

The parent compounds of these materials have been shown by us and others [1; 33] to superconduct upon the application of large pressures. In order to see superconductivity in undoped Sr122, pressures of at least 30kbar are required [2]. However, with reference to a cartoon phase diagram for these materials shown in figure 4.12, we can see that in samples whose magnetic transition has already been strongly suppressed by doping, it seems sensible that much more modest pressures might be sufficient to lead to superconductivity. Indeed, it has been shown for Ba122 that doping reduces the required pressure [13].

To test whether this is true in the Sr122 system, I used a piston-type cylinder cell developed in QM for use with the MPMS, which gives access to pressures of up to 12kbar, to measure doped samples near to the superconducting regime. The cell allows a very small sample to be pressurised and inserted into a SQUID magnetometer. Because of the large background from the cell, it is insensitive to weak transitions, but superconducting transitions can easily be detected. A piece of tin is used as the pressure gauge - since the superconducting transition temperature of tin with pressure applied is known, it can be used at low temperature to measure the pressure inside the cell. It is also used to centre the measurement on, so we hope that the tin and the sample are very close together. The mass of the

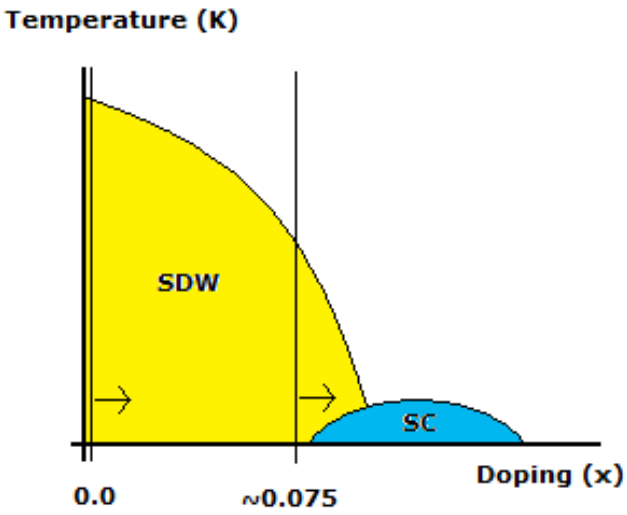

Figure 4.12: This diagram shows a cartoon of the phase diagram of Sr122 with doping, which suppresses magnetism and eventually leads to superconductivity. However, it is known that the parent compound can also be driven to superconductivity via quite large pressures, which also suppress magnetism and eventually lead to superconductivity. It seems sensible to hypothesise that samples in which doping has already significantly suppressed the Neel transition but which do not yet superconduct themselves might be susceptible to the development of superconductivity at much more modest pressures, achievable within a SQUID pressure cell.

sample and the tin are both below 0.0001g, the lower limit of our lab-based mass balance, but we can infer the volume of the tin from the size of its Meissner transition. As we don't know the volume fraction of the pnictide superconductivity quantitatively, we cannot make the same inference for the crystal.

The samples chosen for our measurements were 6.5% and 7.4% doped samples, neither of which showed the Meissner effect at ambient pressure. Up to the highest pressures applied, we did not see superconductivity in the first sample. The second sample, however, showed results consistent with Meissner effect at 7.09 kbar, as shown in figure 4.13 and 4.14.

The pressure in the cell at low temperatures can be calculated using the known superconducting transition temperature of tin with pressure, shown in figure 4.15, although we need to account for the additional suppression due to the

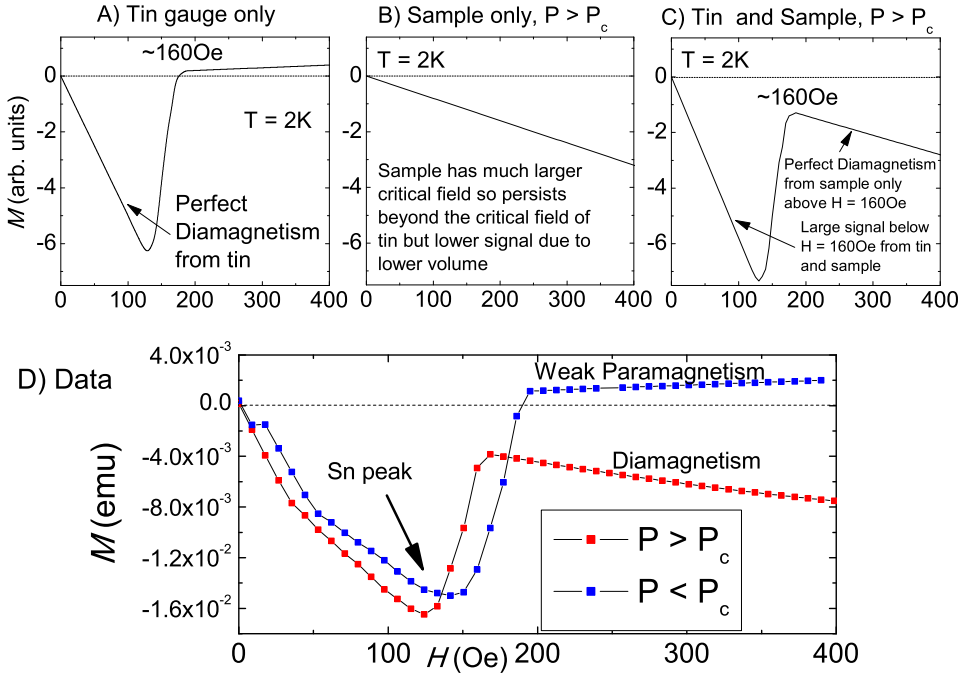

Figure 4.13: The top section shows a schematic of our measurement setup. In our cell we have a piece of tin, to be used as a pressure gauge, and a small sample of 7.4% doped $Sr(Fe_{1-x}Co_x)_2As_2$. The first three panels show the behaviour of different setups in different pressure configurations. Panal A) shows the expected M vs H profile of tin at $T = 2$K. B) shows the behaviour of a sample above its critical superconducting pressure at $T = 2$K. Finally, panel C) shows the behaviour of a combination of both tin and a sample (ie. the sum of A) and B)) above its critical pressure at 2K. Since the sample has a much higher critical field [60] but lower overall volume, its signal is smaller but persists to much higher fields. The large lower panel D) shows our background-subtracted cell data at two different pressures, which is consistent with a pressure-induced superconducting transition in our sample. The lower pressure data (blue) should be compared to panel A) above, while the higher pressure data (red) should be compared to panel C) above. The field at which the tin peak is suppressed allows us to calculate the pressure applied in each case (described in text). Lower critical fields in these materials are on the order of several hundred Oersteds [3], above the field range displayed in D)

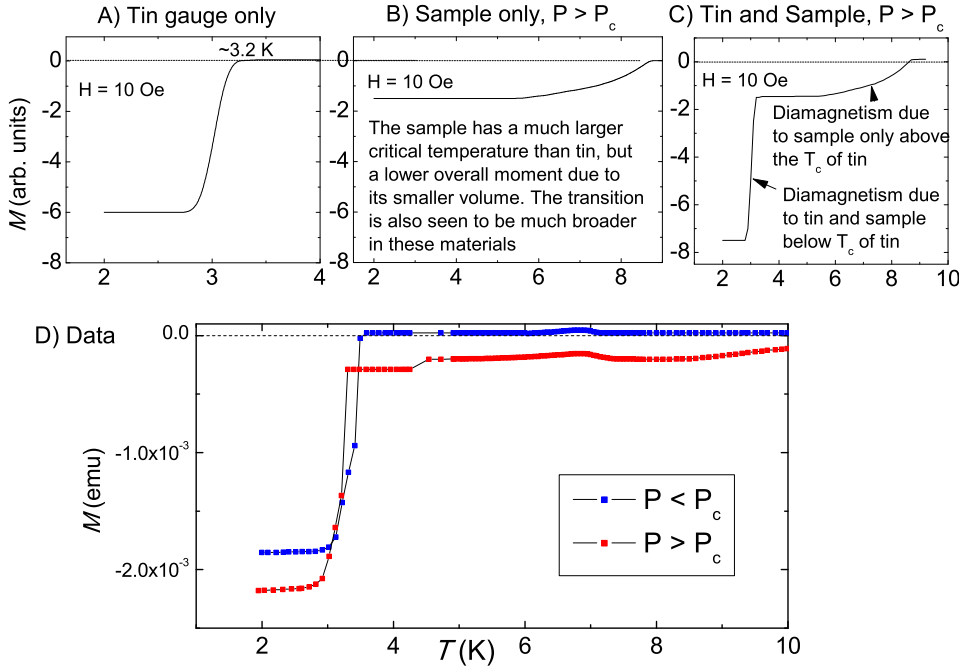

Figure 4.14: The first three panels show the behaviour of different setups in different pressure configurations. Panal A) shows the Meissner M vs T profile of tin at $H = 10$ Oe. B) shows a sample above its critical superconducting pressure at $H = 10$ Oe. Finally, C) shows the behaviour of a combination of both tin and a sample (ie. the sum of A) and B)), above its critical pressure at 10Oe. Since the sample has a much higher critical temperature but lower overall volume, its signal is smaller but persists to much higher temperatures. In the case where the two are combined, the low-T signal is also increased by the extra diamagnetic signal from the sample. The large lower panel shows our background-subtracted cell data at two different pressures, which is consistent with a pressure-induced superconducting transition in our sample. The lower pressure data (blue) should be compared to panel A) above, while the higher pressure data (red) should be compared to panel C) above. The temperature at which the tin peak is suppressed allows us to calculate the pressure applied in each case (described in text). Note that the two datasets here are at the same pressures as the measurements shown in figure 4.13

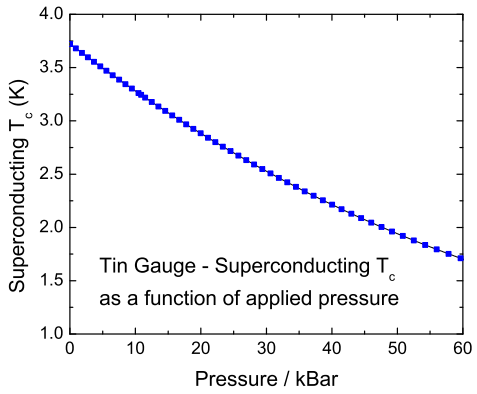

Figure 4.15: T_c vs. Applied Pressure in Sn, used to calculate the actual applied pressure inside a pressure cell at low T [Private Communication, Montu Saxena]

(small) magnetic field applied. At ambient pressure and zero field, the superconducting transition temperature of tin is T_c=3.72K, and the critical field is H_c=310 Oe. Suppression of transition temperature in a Type-1 BCS superconductor is described by the mean-field expression

$$\frac{T_c(H)}{T_c(0)} = \sqrt{\frac{H_c(0) - H}{H_c(0)}} \tag{4.1}$$

[1].

For the lower pressure, we observe a superconducting tin transition temperature of T_c(H=10 Oe) = 3.49K. Since $H \ll H_c$, a binomial approximation yields a good estimate of $T_c(0) \simeq 3.55$K, giving a pressure of 3.80 kbar.

For the higher pressure, T_c(H=10 Oe) = 3.35K. A similar calculation yields $T_c(0) \simeq 3.40$K, giving a pressure of 7.09 kbar.

However, the measurements were not unambiguous. Firstly, the large thermal mass of the cell led to the SQUID having problems between 4K and 4.2K, where the cooling mechanism switches from helium cooling to a 1K-pot cooling system, which gave jumps in our magnetisation data at that point. Secondly, the cell itself showed a magnetic signal with a peak at about 7K in M vs T sweeps,

[1] once again, this is formally only true *near* the transition, but like many aspects of the Ginzburg-Landau theory often turns out to give surprisingly accurate results right down to $T = 0$

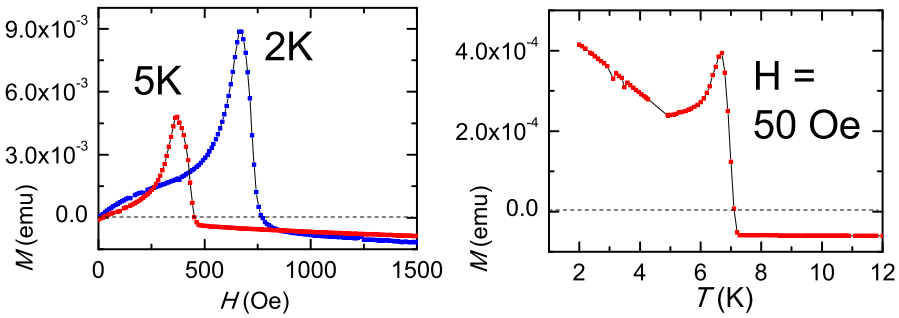

Figure 4.16: Background measurements for the easyLab Mcell 10 used in these measurements for M vs H at two temperatures and M vs T at $H = 50$ Oe. Clearly these backgrounds are not ideal. Although the MPMS system we used can subtract measured backgrounds, it does a poor job when the background is changing rapidly in temperature or field. Clearly this gives problems in the regions with large background peaks - notably around 7K for M vs T sweeps and above about 500 Oe for M vs. H sweeps at $T = 2$K.

and at varying temperature-dependent fields in M vs H sweeps (figure 4.16). Despite attempts to subtract background, this peak continued to appear in our M vs T data. Finally, the superconducting offset observed via magnetisation was broadened considerably by pressure. This was probably due to pressure inhomogeneities and made defining a superconducting temperature difficult.

I have shown in principle that in $Sr(Fe_{1-x}Co_x)_2As_2$ samples doped near to superconductivity, moderate pressures seem sufficient to induce superconductivity. Because of the problems discussed above, however, I decided not to continue with a more detailed investigation.

Chapter 5

Resonant Ultrasound Spectroscopy

In Resonant Ultrasound Spectroscopy (RUS), a sample is balanced mechanically between two transducers. One of these is vibrated at a varying ultrasonic frequency, and the other measures the response of the crystal. A schematic of the setup is shown in diagram 5.1. As mechanical resonances of the crystal are approached, there is a peak in the measured response. For known shapes of crystal, elastic constants can be extracted from these. For arbitrarily shaped crystals this is not straight-forward. However, sequences of response data can be measured at different temperatures and the behaviour of peaks followed up to phase transitions, which gives valuable information about the microscopic nature of the transition.

Early ultrasound spectroscopic measurements on the pnictides have suggested that some compounds can be fitted to a Ginzburg-Landau model [78], but to our knowledge no detailed study of dispersion has been attempted.

Four of our samples were measured by Prof. Michael Carpenter in the Earth Sciences department at the University of Cambridge (as mentioned in acknowledgements) at a collection of temperatures between room temperature and 10K, who supplied the data to me for analysis. Samples chosen had the following compositions: $SrFe_2As_2$, $Sr(Fe_{0.919}Co_{0.081})_2As_2$, $BaFe_2As_2$, $Ba(Fe_{0.955}Co_{0.045})_2As_2$. These samples represent the undoped parent compounds of each family, and a

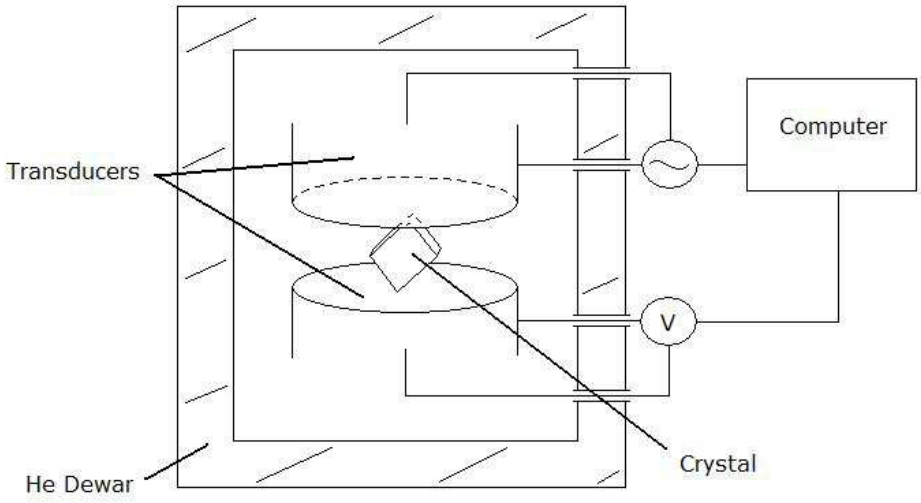

Figure 5.1: A schematic setup of an RUS experiment. The sample is balanced mechanically between two transducers. The entire setup can be immersed in a cooling chamber to allow a sweep of temperature. A driving frequency caused varying response from the crystal, rising to a maximum near to free resonance frequencies, which was measured by the lower transducer

sample chosen to display both a Neel transition and a superconducting transition (see figure 4.8 for resistance profiles).

In order to correctly interpret the results presented later in this chapter, we must first make a short diversion into the application of Ginzburg-Landau theory to ferroelastic phase trainsitions.

5.1 Ginzburg-Landau Theory of Structural Phase Transitions

Ginzburg-Landau theory has been applied with much success to many phase transitions. Here we develop a GL theory of structural phase transitions, looking particularly at the driving mechanism behind the transition. There are two broad subsets of structural transitions - those in which the spontaneous strain that occurs at the transition is the driving order parameter, and those in which it is driven by a separate parameter (In both cases there are a large number of

subsets).

This is of particular interest in situations where structural order onsets along with another type of order in determining which is the 'driving force' behind the transition. Because elastic constants are the second derivative of free energy with strain according to

$$C_{ik} = \frac{d^2G}{de_i de_k} \tag{5.1}$$

(quantities defined in section 5.1.2) and these are easily measurable across a wide range of temperatures, the theory allows a detailed test of many different proposals for the transition mechanism.

5.1.1 First- and Second-Order Transitions

To describe a phase transition in a GL framework we formulate a phenomenological free energy expansion in an order parameter assumed to be small near the transition. We will keep the discussion straightforward by assuming a scalar field. In doing so we neglect 'current' terms, but allow for a more intuitive explanation of a variety of phenomena. The expression for free energy density[1] coming from this is

$$F = \frac{1}{2}a(T - T_c)Q^2 + \frac{1}{4}bQ^4 + \frac{1}{6}cQ^6 \tag{5.2}$$

In the case that b is positive, the term in Q^6 can be neglected. Minimising F with respect to Q leads us to a second-order transition, with F zero above the transition and then becoming increasingly negative below, and $T_c = \frac{b}{a}$ (the order parameter in this case is defined to be unity at $T = 0$).

However, for b negative we have a new possibility - that of a first-order transition (the limiting case of a tricritical transition when $b \simeq 0$ is neglected here). In this case, we find a first-order transition occurring at T_{tr}, somewhat higher than T_c. At this point there is a sudden jump in the order parameter from $Q = 0$ to $Q = Q_0$. In anticipation of such transitions that we will encounter later, it

[1] since we are dealing with strains that are considered uniform across the entire crystal - there are no penetrating vortices of tetragonality in our orthorhombic crystal! - we use F to refer to the free energy *density*

is worth detailing the relevant behaviour arising in this situation, once again by minimising F with respect to Q

$$T_{\mathrm{tr}} = T_{\mathrm{c}} + \frac{3}{16}\frac{b^2}{ac} \tag{5.3}$$

$$Q_0 = \pm\sqrt{\frac{-4a(T_{\mathrm{tr}} - T_{\mathrm{c}})}{b}} \tag{5.4}$$

With a latent heat of transition

$$L = \frac{1}{2}aQ_0^2 T_{\mathrm{tr}} \tag{5.5}$$

And an entropy (relative to the unordered state) below the transition behaving as

$$\Delta S = -\frac{2}{3}\frac{L}{T_{\mathrm{tr}}}\left[1 + \sqrt{1 - \frac{3}{4}\left(\frac{T - T_{\mathrm{c}}}{T_{\mathrm{tr}} - T_{\mathrm{c}}}\right)}\right] \tag{5.6}$$

5.1.2 Strain-Driven Transitions

In many cases, the symmetry-breaking strain itself is the order parameter, and we consider Hooke's law in order to construct a free energy from spontaneous strains e_i, e_j etc. using Voigt notation defined in the literature[8; 9] and introduced briefly in appendix 7,

$$\sigma_i = C_{ik}e_k + C_{ikl}e_k e_l + C_{iklm}e_k e_l e_m + ... \tag{5.7}$$

We have considered here terms beyond the linear ones because at a spontaneous phase transition, many C_{ik} coefficients will become zero. In this case, higher order terms must be considered.

$$F_{elastic} = \frac{1}{2}\sum_{ik} C_{ik}e_i e_k + \frac{1}{3!}\sum_{ikl} C_{ikl}e_i e_k e_l + \frac{1}{4!}\sum_{iklm} C_{iklm}e_i e_k e_l e_m + ... \tag{5.8}$$

Considering this within the second-order Landau scheme discussed above for our tetragonal $\rightleftharpoons$ orthorhombic transition from point group I4/mmm to Fmmm,

the relevant elastic constant is C_{66} with the relevant strain order parameter given by e_6 and without odd terms in the order parameter

$$F_{elastic} = \frac{1}{2}C_{66}e_6^2 + \frac{1}{4}C_{6666}e_6^4 \tag{5.9}$$

When strain is the driving order parameter, this is the only contribution to the GL free energy density so

$$F = \frac{1}{2}a(T - T_c)e_6^2 + \frac{1}{4}be_6^4 \tag{5.10}$$

Minimising this with respect to the order parameter gives the expected T_c. We can go further and explore the behaviour of the relevant elastic constant C_{66} using equation 5.1,

$$C_{66} = \frac{\delta^2 F}{\delta e_6^2} = a(T - T_c) + 3be_6^2 \tag{5.11}$$

Remembering that the order parameter e_6 is zero above the transition and given by $e_6^2 = \frac{a}{b}(T_c - T)$ below, we expect that the elastic constant will be

$$C_{66} = \begin{cases} a(T - T_c) & T > T_c \\ 2a(T_c - T) & T < T_c \end{cases} \tag{5.12}$$

This behaviour is shown in figure 5.2, the elastic constant should go to zero linearly at the transition, but the slope on either side of the minimum will be in a 2:1 ratio.

Transitions driven purely by strain are known in the literature as 'proper ferroelastic transitions'.

5.1.3 Non-Strain Driven Transitions

It will transpire that interactions between strain and another driving order parameter will renormalise the bare elastic parameters. In the case where we have another structural feature driving a transition, strain will emerge as a consequence of coupling with the driving order parameter Q, we have to consider a

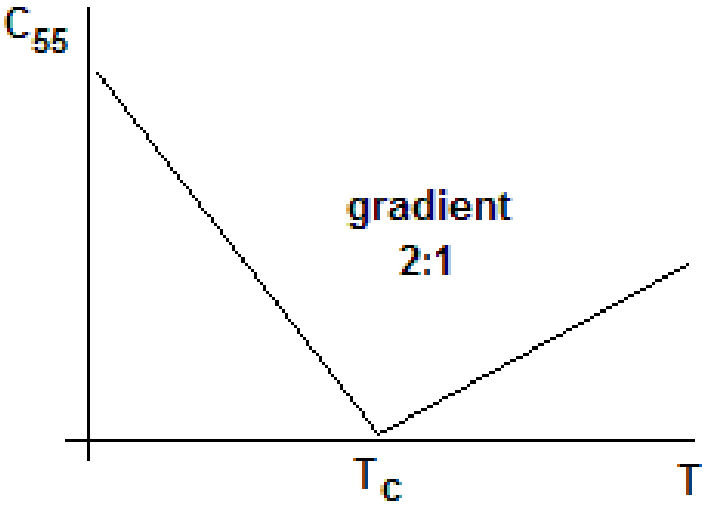

Figure 5.2: A schematic of the suppressed elastic constant across a strain-driven transition. The elastic constant linearly goes to zero on each side of the transition, but with a gradient ratio of 2:1

more general form of the free energy.

$$F = F_Q + F_{elastic} + F_{coupling} \tag{5.13}$$

Using the now familiar forms for F_Q and $F_{elastic}$ gives

$$F = \frac{1}{2}a(T - T_c)Q^2 + \frac{1}{4}bQ^4 + \frac{1}{6}cQ^6 + \frac{1}{2}\sum_{ik} C_{ik}e_i e_k + \sum_{i,m,n} \lambda_{i,m,n} e_i^m Q^n \tag{5.14}$$

(where m and n are integers). The form of elastic constants measured will depend strongly on the form of the coupling term.

In general, we could have any values of i, m, and n for $\lambda_{i,m,n}$, leading to a wide variety of transitions. In fact, since strains are typically small, we can usually confine ourselves to $m = 1$. Beyond that we need to consider the symmetry of the overall free energy. The full calculation is an excercise in group theory, and a detailed analysis of many general transitions is carried out in ref. [9].

This coupling has important implications for the elastic constants. Now that

e and Q in general depend on one-another, we must consider the full differential given in equ. 5.1 rather than the partial differentials in equ. 5.11. The new result for coupled e and Q is

$$C_{66} = C_{66}^0 - \left(\frac{\delta^2 F}{\delta e \delta Q}\right)^2 \left(\frac{\delta^2 F}{\delta Q^2}\right)^{-1} \tag{5.15}$$

This rather messy-looking equation has very important consequences. The mixed dirivative in e and Q will ONLY be non-zero above the transition (where both e and Q are zero) for the case of bilinear coupling. Any more complicated form of a coupling term WILL NOT produce softening above the transition temperature within this scheme.

Since it will turn out that we do indeed see softening of the elastic constant above the transition temperature, I will develop the situation for the case of a bilinearly-coupled transition, which will turn out to describe well my later observations. Such bilinear coupling is termed a 'pseudo-proper' ferroelastic transition in the literature, while linear-quadratic coupling is termed 'improper'. Such a model describes an order parameter that has the same symmetry as the orthorhombic strain. Most importantly, in these materials this order parameter CAN NOT be the antiferromagnetic order that develops below T_{N}, since it does not have the same symmetry as the orthorhombic distortion.

Writing again the free energy for our system within the bilinearly-coupled regime

$$F = \frac{1}{2}a(T - T_{\mathrm{c}})Q^2 + \frac{1}{4}bQ^4 + \frac{1}{6}cQ^6 + \frac{1}{2}C_{66}^0 e_6^2 + \lambda e_6 Q \tag{5.16}$$

Where C_{66}^0 etc. refer to the bare elastic constants. The elastic energy, ie. the Hooke's Law term, has been cut off after the quadratic term because the strain e_6 is small. At first glance the coupling term appears antisymmetric in the sign of Q. This tells us that e_6 and the order parameter must share the same symmetry, so that their product is unchanged for a reversal in the strain direction (because of this I will henceforth refer to Q as a STRUCTURAL order parameter).

Minimising F wrt. e_6 gives

$$e_6 = -\frac{\lambda}{C_{66}^0} Q \tag{5.17}$$

Substituting this back into equation 5.16 gives a second term in Q^2 which effectively renormalises the critical temperature to a higher value, which gives

$$F = \frac{1}{2}a(T - T_c^*)Q^2 + \frac{1}{4}bQ^4 + \frac{1}{6}bQ^6 \tag{5.18}$$

with

$$T_c^* = T_c + \frac{\lambda^2}{aC_{66}^0} \tag{5.19}$$

Using expression 5.15 for elastic constant softening

$$C_{66} = C_{66}^0 - \frac{\lambda^2}{a(T - T_c)} \tag{5.20}$$

Then combining 5.19 and 5.20 we come to an expression for the softening of elastic constants above a bilinearly-coupled ferroelastic phase transition

$$C_{66} = C_{66}^0 \left(\frac{T - T_c^*}{T - T_c} \right) \tag{5.21}$$

This important equation will form the basis of our fitting procedure for the later resonant ultrasound spectroscopy experiments and deserves some attention. T_c is the temperature at which the second order structural phase transition would occur without strain coupling to the order parameter Q, while T_c^* is the temperature at which it occurs after strain renormalisation. We see from equation 5.19 that $|T_c^* - T_c|$ is a measure of the strength of strain coupling to the order parameter.

The distinction between strain e as an order parameter and some other structural order parameter Q seems semantic (especially given that in the case of bilinear coupling, the two quantities will be directly proportional). However, as we have seen here there is a measureable difference between the two. A strain-driven transition will lead to elastic constants which soften linearly to zero above the transition as in figure 5.2. A non-strain-driven transition will either cause

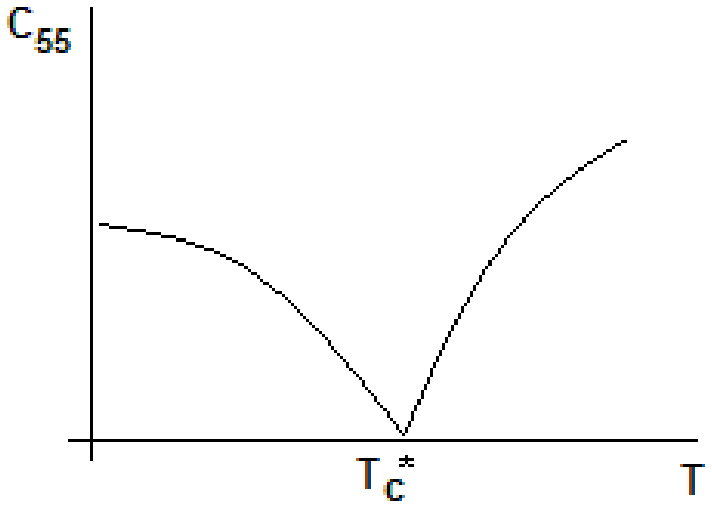

Figure 5.3: A schematic of the suppressed elastic constant across a bilinearly-coupled non-strain-driven transition. The elastic constant behaviour is very different from the strain-driven case, and is now supressed to zero at a strain renormalised temperature of T_c^*. For any coupling other than bilinear coupling, there would be no softening above T_c

no softening above the transition in the case of anything other than bilinear coupling, or will cause softening according to equ. 5.21 as shown in fig. 5.3 in the case of bilinear coupling. As we will see in my data later, observed behaviour is very clearly of the final type, a strong signal of bilinear coupling within this model.

Finally, remembering the sixth-order term in Q in the Landau expansion allowing first-order transitions as before, then the transition will occur at *neither* of these temperatures but in fact at T_{tr} discussed above - although of course the T_c term appearing in it will be renormalised by strain.

Equipped with this analysis, we are now in a position to return to the RUS experiment.

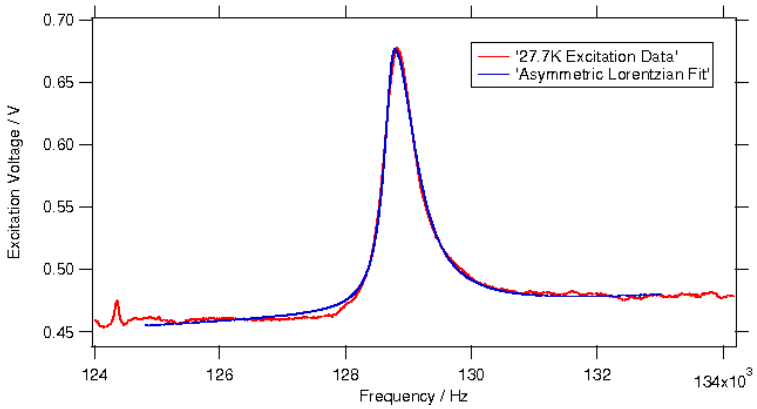

Figure 5.4: The excitation voltage measured by the lower transducer in the RUS setup, here at 27.7K. The Lorentzian fit typically produces a good match to the data except where other broadening phenomena are overlaid onto the peak

5.2 Fitting Procedure

Resonant peaks were fitted with a six-parameter asymmetric lorentzian lineshape

$$F(\nu) = \begin{cases} A + B\nu + \frac{C}{(\nu - D)^2 + E} & \nu < D \\ A + B\nu + \frac{C}{G(\nu - D)^2 + E} & \nu > D \end{cases} \tag{5.22}$$

This allowed the elimination of a local frequency-linear baseline and accounts for observed asymmetry in the observed lineshapes. A typical fitting curve is shown in figure 5.4.

For well-fitted peaks, an expression for the full width at half maximum can be quickly obtained by considering the points on either side at which $F(\nu) = C/2E$, leading to the expression

$$W_{\mathrm{FWHM}} = \sqrt{E}\left[1 + \sqrt{\frac{1}{G}}\right] \tag{5.23}$$

And finally the inverse quality factor of the resonant peak is given by the standard result for resonant systems

$$Q^{-1} = W_{\mathrm{FWHM}}/\nu \tag{5.24}$$

It should be noted that while spectra were measured across the full tempera-

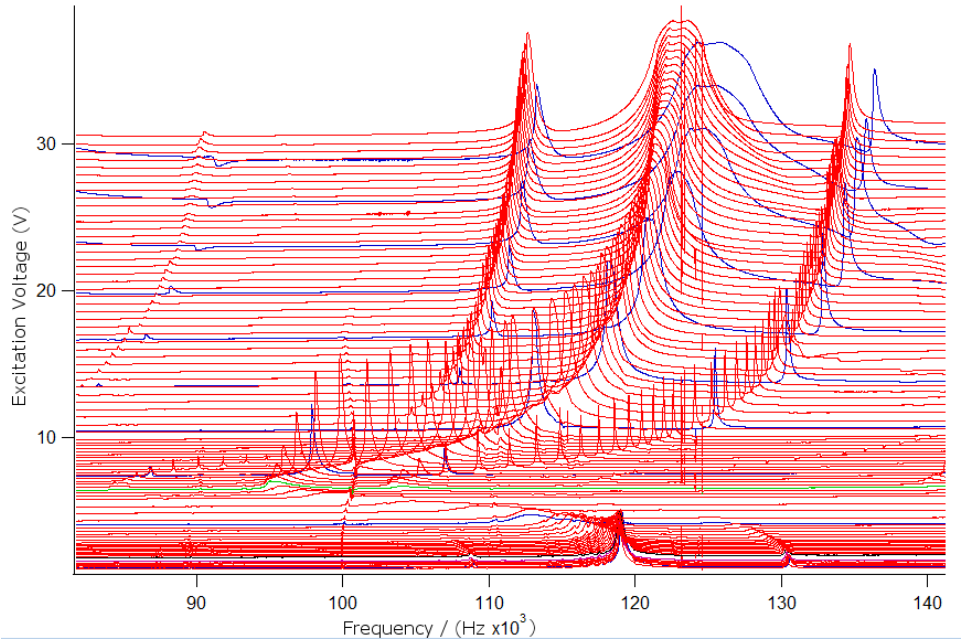

Figure 5.5: A typical set of measured RUS peaks. Each trace represents a different temperature, and they are offset by an excitation voltage proportional to their temperature for ease of viewing. We see a softening near and below the transition temperature, and a sequence of sharp peaks at high temperatures. The broadening of the central peak at the highest temperatures is in fact an artefact of the measurement, which saturates at 9V. To measure this peak accurately would require a lower input voltage to be used (which in turn would of course render the weak peaks at lower temperatures less accurate)

ture range spanning RTP to around 10K, it was not always possible to follow the evolution of particular resonant peaks across the whole range. Some peaks would shrink and disappear above a certain temperature, and others would cross regions containing temperature-independent noise peaks (mostly relics of the system architecture) or would cross one-another so that the overall peak was a convolution of the two, making them impossible to fit in certain regions. Once again, the tendency of these crystals to self-cleave on warming again led to difficulties in repeatability of some measurements, as the geometry of crystals occasionally changed unpredictably with temperature.

A typical set of measured profiles is shown in figure 5.5. In this case three peaks can be seen clearly around RTP. However, the lowest peak becomes very

weak above and during the transition region, making it very hard to follow. In some noisier datasets, the problems discussed above make accurate following of peaks impossible in various temperature ranges.

5.3 $SrFe_2As_2$

As discussed in the previous chapter, from other probes Sr122 was found to display a single transition from tetragonal and paramagnetic to an orthorhombic magnetically ordered state, with a transition that was sharp and first-order like. By combining RUS data, heat capacity measurements from the previous chapter, and some data from the literature, I am able to completely characterise the softening in elastic constants above the transition in Sr122 within the Landau phenomenology. Its behaviour below the transition is slightly more mysterious.

For a pseudoproper ferroelastic phase transition, as discussed in the section 5.1, we expect the elastic constant to vary above the transition according to 5.21, repeated here for convenience:

$$C_{66} = C_{66}^0 \left(\frac{T - T_c^*}{T - T_c} \right) \tag{5.25}$$

with quantities as defined before. Because the elastic constant is proportional to frequency squared, we can perform a fit to the datasets shown in the upper panels of figure 5.6 for which I have followed peaks up to at least 250K. The fit is shown in figure 5.8. Parameters extracted are $T_c^* = (172.0 \pm 0.8)$K and $T_c = (163.8 \pm 1.5)$K, giving a value of $|T_c^* - T_c| = (8.2 \pm 1.7)$K. Further, $T_{\mathrm{tr}} = (190.9 \pm 0.5)$K giving $|T_{\mathrm{tr}}^* - T_{\mathrm{c}}^*| = (18.9 \pm 0.9)$K.

The excess entropy of the transition can be calculated from the heat capacity data presented in the previous chapter in figure 4.10a and figure 4.11, by fitting the entropy for the transition to the region above and below the transition and measuring the entropy jump. The measured discontinuity across the full transition is (1.34±0.01) J mol^{-1} K^{-1}.

We can also use data from the literature to calculate the orthorhombic distortion, which is a function of the order parameter, the linear coupling constant, and the elastic constant, according to equation 5.17. I have taken data from

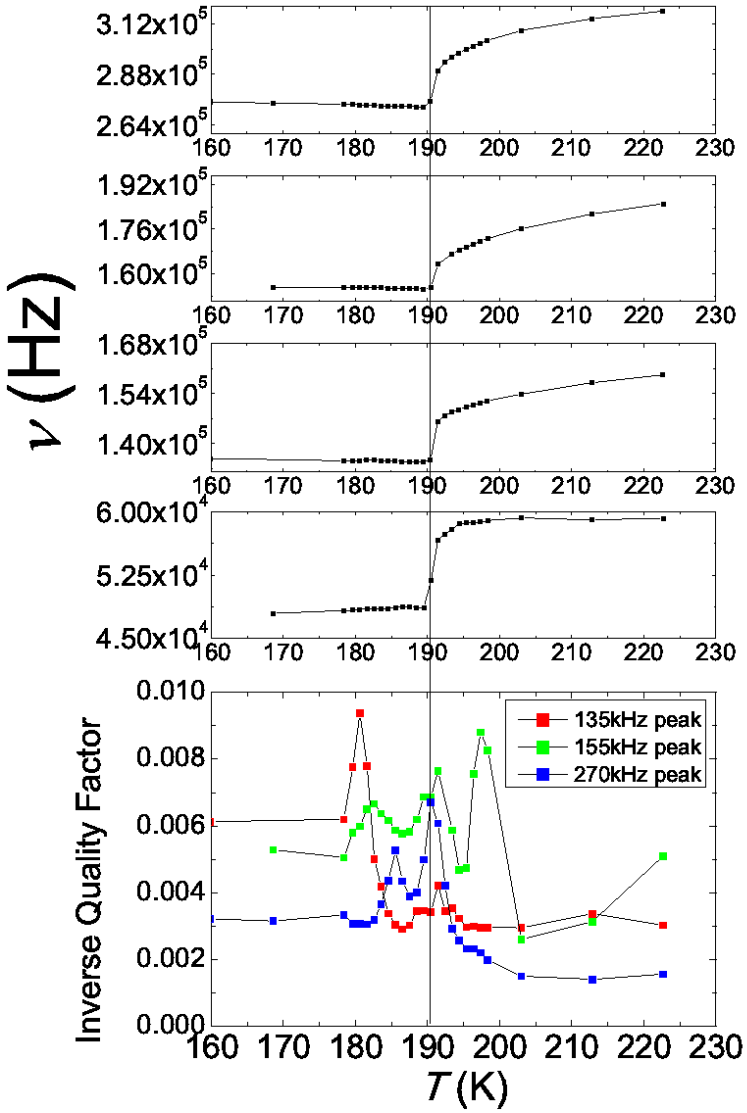

Figure 5.6: The upper four panels show the temperature dependence of several peaks in the RUS spectrum of undoped $SrFe_2As_2$. They all display a clear first-order-like transition at about 191K. The lowest panel shows the temperature dependence of the inverse quality factor of the resonant peaks for the higher three frequency peaks. As well as a peak near to 191K, there seems to be a lower, frequency-dependent peak in each spectrum (the peak near 200K in the 155kHz peak is due to an overlapping broad frequency-independent peak in the vicinity).

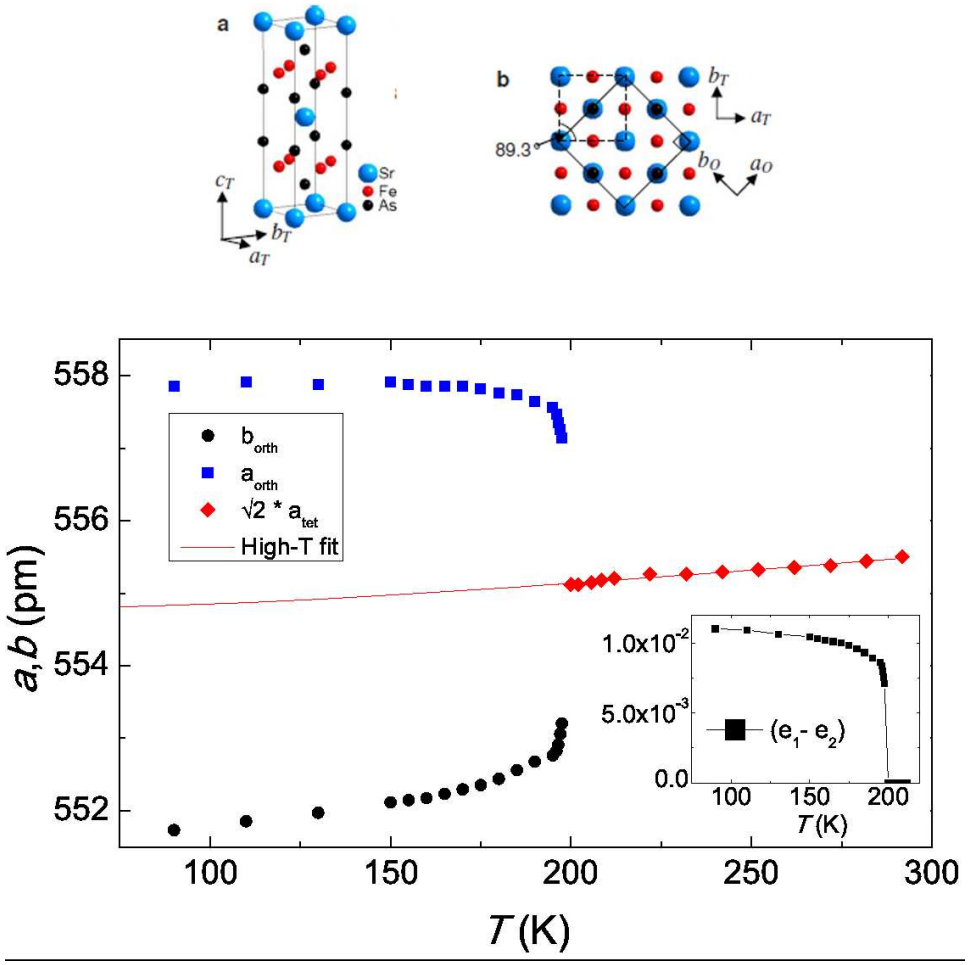

Figure 5.7: Strain analysis to extract orthorhombic strain parameters e_1 and e_2, using data presented in ref. [70]. The upper panels show a schematic of the tetragonal (a) and orthorhombic (b) unit cell viewed down [001]. The tetragonal unit cell is shown in dashed lines and the orthorhombic in solid lines. The lower panel shows variation of parameters with temperature, the high-temperature tetragonal parameters are fitted with a function $a + b.c.\mathrm{Coth}(\frac{c}{T})$ to ensure saturation at $T = 0$, and strain in the low-T state calculated by the difference from that baseline. The quantity $(e_1 - e_2)$ should be proportional to order parameter Q in a ferroelastic scheme

ref. [70][1], the strain analysis is shown in figure 5.7. Normalising the maximum orthorhombic distortion at $T = 0$ to 1 we calculate $Q_0 = (0.72 \pm 0.03)$.

The form of the free energy that we fit is the bilinear coupling of strain and the order parameter given in equ 5.16

$$F = \frac{1}{2}a(T - T_c)Q^2 + \frac{1}{4}bQ^4 + \frac{1}{6}cQ^6 + \frac{1}{2}C^0_{66}e_6^2 + \lambda e_6 Q \tag{5.26}$$

As discussed in the theory section, the role of strain is to renormalise the (second-order, T_c) transition temperature to a new value T_c^*, giving an effective free energy

$$F = \frac{1}{2}a(T - T_c^*)Q^2 + \frac{1}{4}bQ^4 + \frac{1}{6}cQ^6 \tag{5.27}$$

Since we have a value of the latent heat, L, from our heat capcity measurements; the discontinuity in the order parameter, Q_0, from the strain analysis; and a value of $(T_{tr} - T_c^*)$ from RUS measurements, we can use equations 5.3 to 5.5 to extract the a, b and c parameters[2].

$$a = \frac{2\ \Delta S}{Q_0^2} = (5.2 \pm 0.3)\ \text{J mol}^{-1}\text{K}^{-1} \tag{5.28}$$

$$b = \frac{-8\ \Delta S\ (T_{tr} - T_c^*)}{Q_0^4} = -(750 \pm 70)\ \text{J mol}^{-1} \tag{5.29}$$

$$c = \frac{6\ \Delta S\ (T_{tr} - T_c^*)}{Q_0^6} = (1.1 \pm 0.1)\ \text{kJ mol}^{-1} \tag{5.30}$$

Finally, the coupling constant λ can be extracted from the RUS data by dividing equations 5.17 and 5.19

$$\lambda = \frac{a(T_c^* - T_c)}{e_{6,\text{T=0K}}} = (3.5 \pm 0.8)\ \text{kJ mol}^{-1} \tag{5.31}$$

[1]It should be noted that there is still some disagreement in the literature, some variation exists in published lattice parameters (and transition temperatures) for Sr122, for example refs. [37; 75]. They agree, however, that the transition is first order

[2]Since equ 5.6 also features $(T_{tr} - T_c^*)$ we could try to extract this value by fitting the excess entropy from the heat capacity data instead of the RUS data. However in practice the region for which it is easy to calculate an accurate excess entropy is very limited, and even then the critical temperatures extracted vary rather sensitivly with the exact procedure used

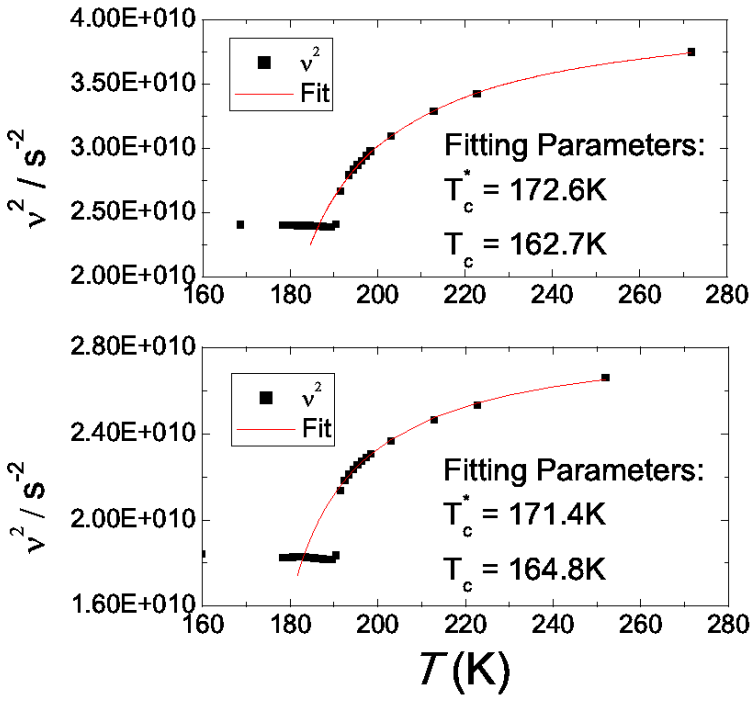

Figure 5.8: Fit for a pseudoproper ferroelastic transition to our frequency data in $SrFe_2As_2$, fit described in text. The two peaks we have enough data to fit show good agreement in the fitting parameters. The modulus of $|T_c^* - T_c|$ is a measure of the strength of the coupling between the strain and the order parameter

The behavior of the frequency peaks in figure 5.6 below the transition is unusual. In a traditional ferroelastic transition, peaks are expected to recover rapidly below the transition. Typically, the Landau expansion fails for one of two reasons. Firstly, it is assumed that the perturbed system responds rapidly enough to reach equilibrium, but systems with slow relaxation times typically do not obey this. Secondly, systems with more than one order parameter require a more detailed expansion in both order parameters and including coupling terms between them. In this system both of these are possibilities, further work will be needed to make firm conclusions.

In addition it is worth briefly discussing the behaviour of the inverse quality factor. There is a large peak occurring at the structural transition. This is to be expected as the material forms twins on lowering of the structural symmetry. Unlike in static experiments, in dynamic experiments these are able to migrate

through the material and lead to dispersion. In addition, each peak seems to display a lower frequency-dependent peak in dispersion several Kelvin below the transition. The origin of these is still unknown. It was suggested that it might be the formation of a tweed lattice (a precursor to frozen in twin pairs), but TEM experiments seem to rule this out[1].

5.4 $BaFe_2As_2$

As seen from various probes in Chapter 4, the picture that emerges from RUS is that of a very much less strong first-order transition in the Ba122 parent compound. A sequence of three peaks could be followed through the transition, their frequencies and inverse quality factors are shown in Figure 5.10. The elastic constant fittings show a much smaller transition near the Neel temperature, shown in Figure 5.11.

Parameters extracted froom the fits $T_c^* = (127.3 \pm 0.4)$K and $T_c = (121.9 \pm 2.0)$K, giving $|T_c^* - T_c| = (5.4 \pm 2.0)$K. Also, $T_{\rm tr} = (133.0 \pm 0.5)$K giving $|T_{\rm tr} - T_c^*| = (5.7 \pm 0.6)$K. A similar strain analysis was performed using data from ref. [56][2], shown in figure 5.9. The resulting normalised jump in order parameter is $Q_0 = (0.53 \pm 0.06)$.

Once again, this can be described within the Landau scheme for a ferroelastic transition above $T_{\rm N}$, and shows the same locking of elastic constants below the transition. I do not have a heat capacity dataset for my own materials, but in a very thorough survey of Ba122 found in the literature [57], a value of 0.84 J $\rm mol^{-1}$ $\rm K^{-1}$ is reported, which is broadly in line with our expectation of a smaller

[1] Private Communication, James Loudon

[2] Once again, the literature presents some variation in lattice parameters and transitions for Ba122. The variation is even greater due to the existence of tin-flux grown samples whose transition is significantly suppressed to ~90K, leading to significant deviations in behavior[66]

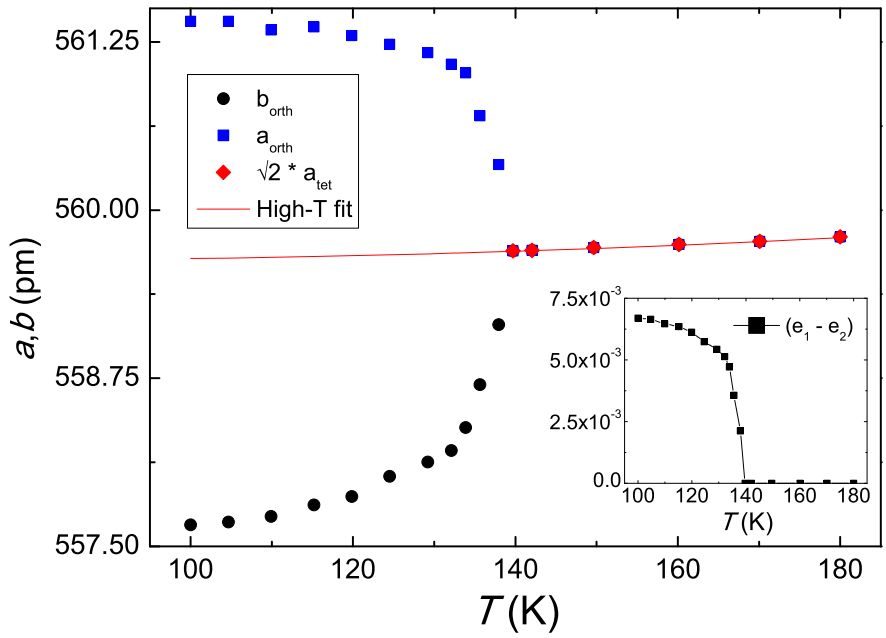

Figure 5.9: A similar strain analysis for $BaFe_2As_2$, revealing a much less strongly first order character than $SrFe_2As_2$. A schematic of the unit cell is shown in figure 5.7

transition than that in Sr122[1].

$$a = (6.0 \pm 1.0)\ \text{J mol}^{-1}\text{K}^{-1} \tag{5.32}$$

$$b = -(500 \pm 100)\ \text{J mol}^{-1} \tag{5.33}$$

$$c = (1.3 \pm 0.4)\ \text{kJ mol}^{-1} \tag{5.34}$$

$$\lambda = (4.0 \pm 1.0)\ \text{kJ mol}^{-1} \tag{5.35}$$

The largest variation between the GL parameters for Sr122 and Ba122 is

[1]The orthorhombic distortion reported in this paper is about twice that reported in the x-ray study I have previously referenced, and it has a significantly more first-order-like nature. However, the data reported is after a 30-day anneal, and they report that this significantly affects other structural parameters and is consequently not used in my survey. The excess entropy, however, is reported to be almost unaffected by this annealing

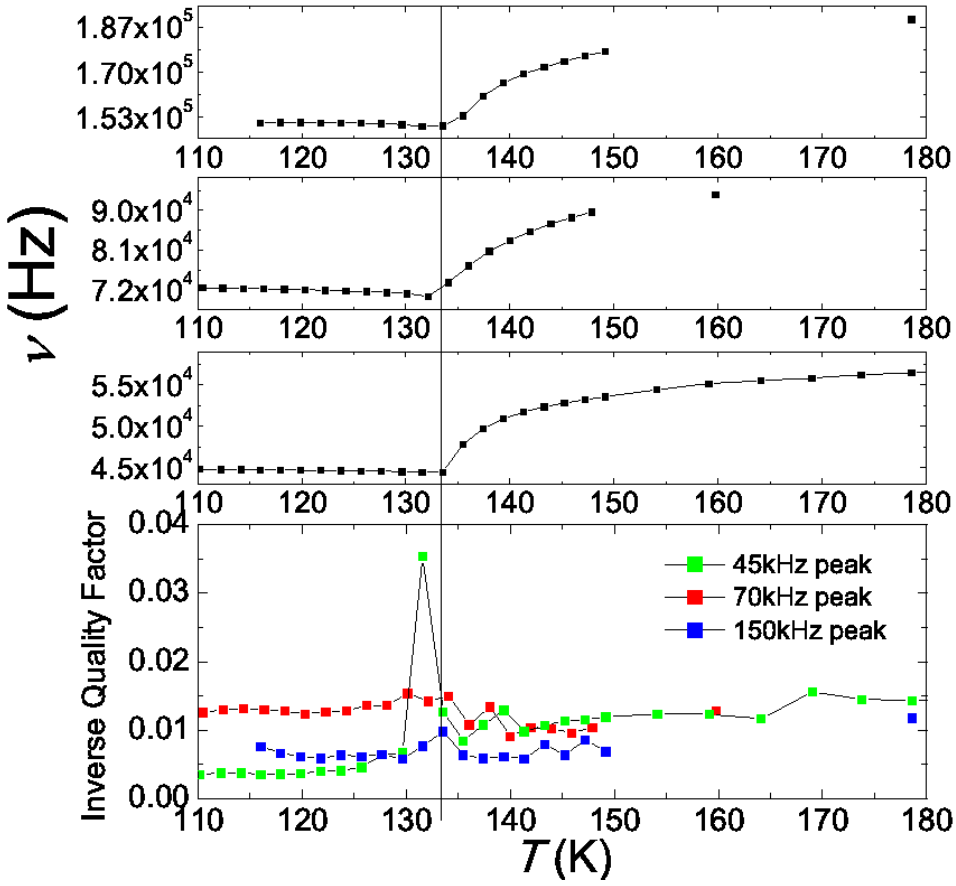

Figure 5.10: The upper three panels show the temperature dependence of several peaks in the RUS spectrum of undoped $BaFe_2As_2$. The lowest panel shows the temperature dependence of the inverse quality factor of the resonant peaks for the three frequency peaks. With one exception, the peak in inverse Q below the transition is much less pronounced in this material).

unsurprisingly in the b-parameter, which dictates the order of the transition as discussed in section 5.1. The strain coupling parameter, and the a and c parameters, are in fact surprisingly similar.

5.5 $Ba(Fe_{1-x}Co_x)_2As_2$

Crystals from both the Co-doped Ba122 and Sr122 families were measured. Dopings were chosen so that samples exhibited both a structural/magnetic transition at higher temperatures, and later a superconducting transition. For the Co-

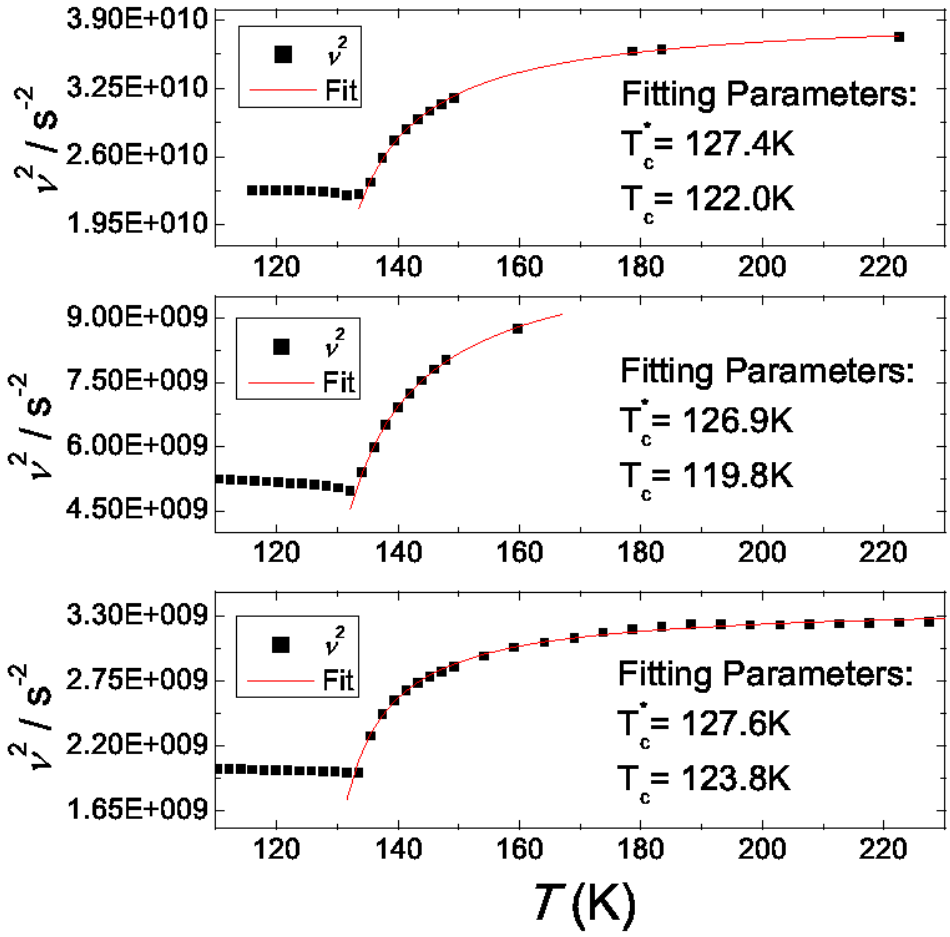

Figure 5.11: Fit for a pseudoproper ferroelastic transition to our frequency data in $BaFe_2As_2$, fit described in text. The spectra are clearly less first-order-like than the $SrFe_2As_2$ peaks shown in figure 5.8, with a smaller drop in elastic constants at the transition temperature. The three peaks we have fitted show good agreement in the fitting parameters. $|T_c^* - T_c|$ is smaller in this material, indicating a weaker coupling of strain to the transition.

doped Ba122 family, a doping of $x = 0.045$ was chosen (unfortunately, at these doping levels the thermodynamic probes discussed in the last chapter cannot see the higher-T transition, which is so-far only visible to us via transport measurements).

The contrast between the doped compounds and the parent compounds is striking. The downturn in resonant frequencies across the transition for Co-doped Ba122 is smooth and uniform across several peaks; and rather than a sharp peak in inverse Q, there is a broad peak extending across 30K, matching very well the derivative of the resistance profile in this material (figure 5.12). The elastic constants are also seen to recover at temperatures below the transition, which was not seen in the parent compounds (but is expected in general in these types of structural transition).

The elastic constants can also be well-fitted using the thermoelastic fitting function 5.25, giving $T_c^* = (57.1 \pm 2.0)$K and $T_c = (45.1 \pm 1.4)$K so that $|T_c^* - T_c| = (12.0 \pm 2.4)$K. This is significantly larger than in the undoped case, indicating an increased role for strain near the transition region for this material. Given that this material exhibits a structural temperature several Kelvin above its magnetic transition, it is tempting to speculate that the increased strain coupling is what leads to the initial occurrence of the structural transition, compared to the case in the parent compounds that might be relatively more strongly driven by magnetism. However, the even-larger strain coupling in the (un-split) doped Sr122 compound explored in the next section seems to argue against this simplistic interpretation.

There also seems to be a subtle baseline shift and slight drop in resonant frequency at the superconducting transition temperature, indicating that superconductivity indeed couples to the lattice, as expected from other work[47]. More work needs to be done to fully understand the detailed effect that this is having.

5.6 $Sr(Fe_{1-x}Co_x)_2As_2$

A strontium sample was chosen as described above with $x = 0.081$. The data for the doped strontium compound was sadly not as good quality as the other datasets and only two peaks could be followed, the measurements are included

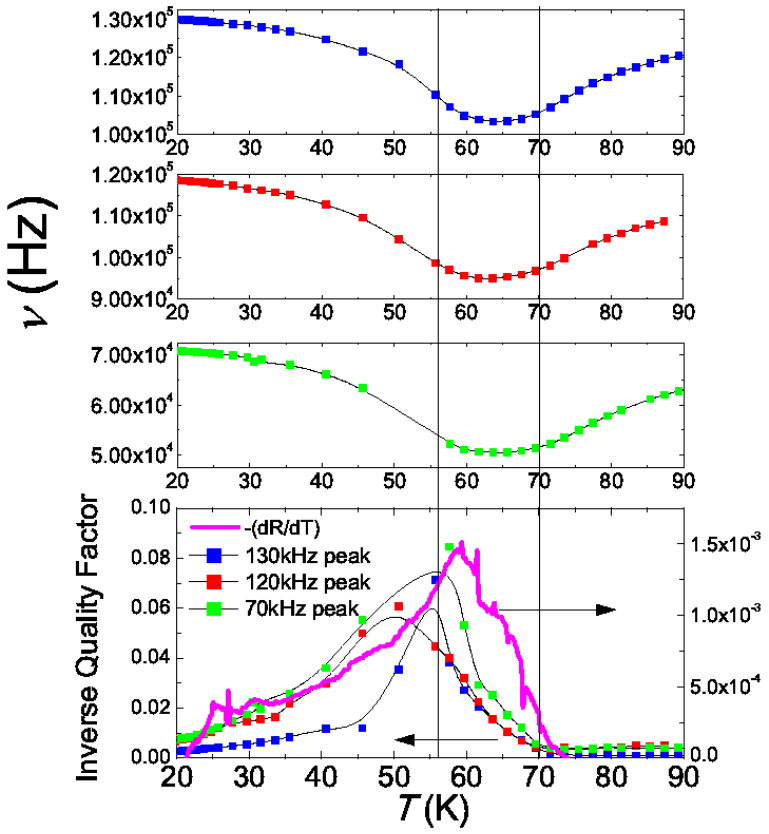

Figure 5.12: The behaviour of three peaks followed through the transition in $Ba(Fe_{0.955}Co_{0.045})_2As_2$ at 55-70K. The peak is seen to be much less first-order-like, with a softening of all elastic constants down to the transition followed by a return to stiffness afterwards. The upturn in the inverse quality factor matches a sharp upturn in the electrical resistance (the derivative plotted here has been smoothed) in this material suggesting a common mechanism for electrical scattering and elastic dispersion.

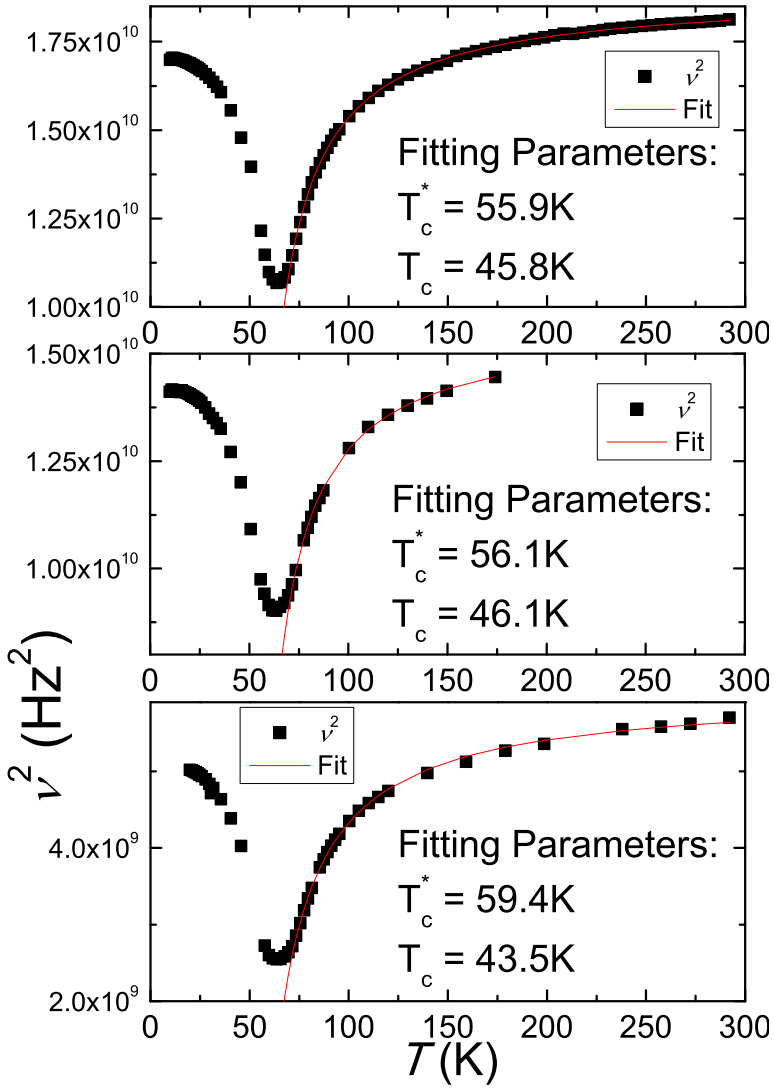

Figure 5.13: Fit for a pseudoproper ferroelastic transition to our frequency data in $Ba(Fe_{0.955}Co_{0.045})_2As_2$, fit described in text. The transition no longer appears at all first-order-like, with a smooth rounded transition spread over a wide temperature range. The three peaks we have fitted show good agreement in the fitting parameters. $|T_c^* - T_c|$ is much larger in this material than the Ba122 parent, and somewhat larger than the value in Sr122. This seems to indicate an increased role for strain in the doped compounds

here for completeness and shown in figure 5.14. These peaks are seen to behave in markedly different ways across the transition, as expected in crystalline samples of inexact geometry but broadly not seen in other datasets. Once again, one peak could be fitted with the thermoelastic fitting function 5.25, giving $T_c^* = (34.7 \pm 1.1)$K and $T_c = (12.1 \pm 2.1)$K, giving $|T_c^* - T_c| = (22.6 \pm 2.4)$K, significantly higher than for previous samples, indicating much stronger strain coupling to the structural order parameter.

Once again, as for Co-doped Ba122 but not for either of Sr122 or Ba122, the elastic constants recover below the transition[1]. Because of the low superconducting temperature in this material ($T_c \simeq (11.4 \pm 3.2)$K) we were not able to fully cross the superconducting transition, and in this case cannot detect any traces from elastic data.

5.7 Summary of RUS Results

We have seen in this chapter that the model developed for a bilinearly-coupled transition driven by a non-strain structural order parameter fits our measured elastic constant softening data very well. This is an important result. Since the coupling is bilinear, the strain and the order parameter must share the same symmetry, which rules out magnetism as the driver in this model. Importantly, I have not specified the nature of this order parameter, and will refer to it henceforth as a hidden order parameter. However, forms of coupling term that would allow magnetism as the order parameter (for example $\lambda e Q^2$ or $\lambda e^2 Q^2$) are ruled out, since according to equ. 5.21 they would produce no softening above T_c.

Although magnetism might seem like the natural choice for the driver of such a structural transition, there is other evidence for a structural driver. Most importantly, in the 1111 compounds and Ba122 a large iron isotope effect has been seen in both the superconducting T_c and T_N [39], suggesting structural effects are involved in both phenomena.

[1] In theory the rate of recovery should give us information about the transition, Ginzburg-Landau theory puts firm constraints on the relative gradients above and below the minimum [8]. However, the smoothness of the minimum and rapid change in gradient made it impossible to calculate this ratio to any specific value with accuracy

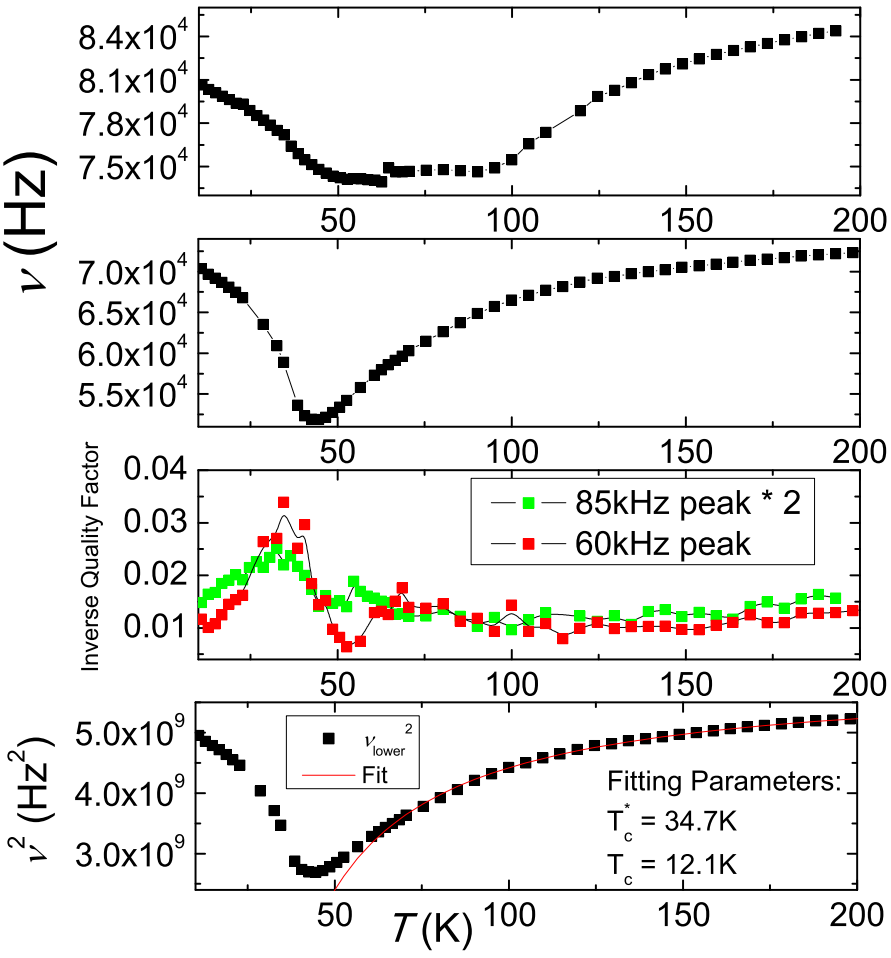

Figure 5.14: The behaviour of two peaks followed through the transition in $Sr(Co_{0.080}Fe_{0.920})_2As_2$. Once again, a less first-order-like behavior is seen. There is again a sharp upturn in the inverse quality factor below the transition point (here identified with the downturn in the lowest peak frequency, which coincides with a maximum in the derivative of the resistivity. Unfortunatly the higher-frequency peak seems rather unreliable, with a sudden and unexpected jump in frequency at 65K and strange peak behavior above that point. A fitting (as previous fits) for the better behaved peak elastic constant is shown in the bottom panel

Other authors [17] have developed a model that describes similar softening of the elastic constants via strain coupling to magnetic fluctuations above the Neel temperature. The hidden order theory described in this chapter fits the data better and is more intuitive, but further experimental data - for example microscopic evidence of hidden order - will be required to identify which of the two models best describes reality.

Chapter 6

Collaborations

In addition to the work described so far, I and my samples have been involved with several projects in collaboration with other workers and groups. In this chapter I will describe briefly a handful of these experiments and sample issues arising from them.

6.1 Quantum Oscillations

When a magnetic field is applied to a metal, electrons perform cyclotron orbits in the plane perpendicular to the field. The radii of these orbits, and their resulting energies, are quantised and lead to a set of Landau levels being filled by electrons (these effects are only noticeable when the thermal energy is much lower than the magnetic energy scale; $k_B T << \hbar\omega_c$). The energy of these levels and their occupation are proportional to magnetic field - as the field increases, the highest occupied levels move across the fermi surface and become depopulated. As more and more levels are pushed out, this depopulation leads to related oscillations in the conductivity and the magnetisation of the metal. The oscillating conductivity with magnetic field is called the Shubnikov-de-Haas effect, and carries information about the masses of the charge carriers in the crystal. The oscillations in the magnetisation is called the de-Haas-van-Alphen effect, and carries information about the maximal radius of electron cyclotron orbits, allowing detailed pictures of the fermi surface to be drawn [22].

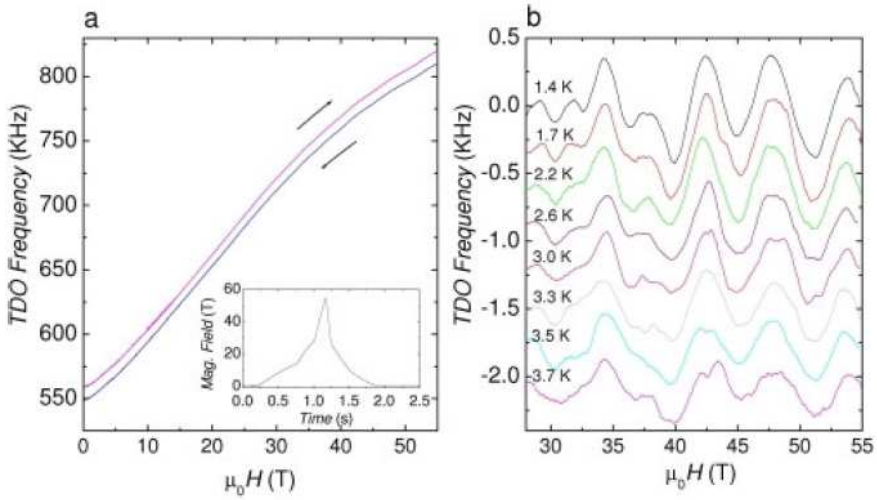

Figure 6.1: From ref. [59]. Quantum Oscillations measured in $SrFe_2As_2$. a) the TDO measurements for rising and falling magnetic field (inset, the magnetic field profile in time). b) quantum oscillations after a polynomial background subtraction

Shortly after the 122 family of Iron Pnictide materials were discovered, I grew a batch of crystals of Sr122 which were measured by a collaborator from the QM group in fields from 22T to 65T in Tallehassee and Los Alamos in the United States. Oscillation frequencies were found corresponding to small Fermi surface pockets, showing the fermi surface of the parent material in this family of superconductors to be reconstructed by magnetism at low temperatures. This work was the first quantum oscillation study of this family of materials, and was nominated as a highlight paper of 2008 by the publishing journal [59]. The observed oscillations are shown in figure 6.1.

More recently similar experiments have been duplicated in the lab. I have grown and mounted several samples for collaborators to measure the hall resistance. This is not a straight-forward process, requiring careful connection of six wires to a thin bar-like crystal sample, the experimental setup is shown in figure 6.2. Unfortunately, due to a shortage of funding only a limited set of runs was performed. However, in one sample, and only after an annealing process as described before, a good quality set of oscillations was observed at 30mK and only 10-16T. Since cyclotron orbits are extremely sensitive to mean free path in

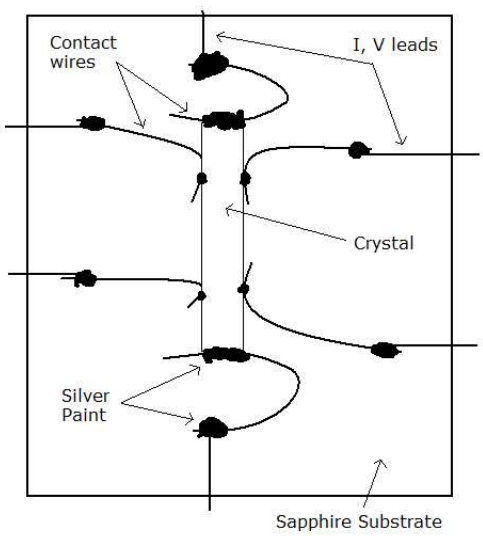

Figure 6.2: A schematic diagram of the setup to measure hall resistance. To allow a uniform current flow, a bar-like morphology is preferred. Here, length $> 5\times$ width. Two current leads of 50μm diameter are connected at either end, and two pairs of voltage leads of 25μm diameter are connected on opposite sides of the bar. The configuration can be checked by first measuring V vs. T using the terminals on the same side of the bar, the results should be close to each other if contacts are well spaced. Then, measuring V vs. T across the crystal with a current flowing in a perpendicular B-field allows measurement of the Hall effect. The photo above shows a sample I mounted. Ideally contacts will cover the whole thickness of the crystal to avoid any component of out-of-plane resistivity, but will not spill onto the crystal surface.

crystals, being easily scattered by impurities, this observation is indicative of the high quality of sample growth and preparation, and of the improvement of mean free path on annealing.

6.2 Pressure-Induced Superconductivity

Pressure is frequently found to be a useful tuning parameter for the behaviour of materials. It tends to flatten the electronic bandstructure of materials, and often leads to new phases emerging at low temperatures. Unlike chemical doping, which introduces impurities, physical pressure is 'clean' - it usually doesn't reduce the mean free path of electrons in the compound, although questions about the hydrostaticity of pressure inside the cells that are used still remain.

Although the parent compounds in the 122 family do not superconduct, samples of Sr122 and Ba122 have been found to superconduct when doped with Cobalt, Potassium, and other dopants which alter the electronic structure of the compound and suppress the magnetic Neel transition. The discovery that Ca122 superconducts under very moderate pressure (about 10 kbar) led us to investigate Sr122 and Ba122, again on samples grown by me. Very soon afterwards, high pressure susceptibility (both AC and DC) measurements taken by members of the Quantum Matter group confirmed a solely pressure-induced transition in my Sr122 and Ba122 compounds at temperatures of up to 29K, by far the largest purely pressure-induced transition temperature discovered to date, shown in figure 6.3.

This was also judged to be a significant breakthrough, and the published work was nominated as a highlight paper of 2009 by the same publisher [2]. Follow-up work led to my measurements described in section 4.4.

Members of the Quantum Matter group have been developing techniques for measuring quantum oscillations under pressures of up to 25 kbar. Although 25 kbar is not sufficient to drive Sr122 or Ba122 into superconductivity, it will for Ca122, or Co-doped Sr122 or Ba122 compounds. Since the suppression of anti-ferromagnetic ordering in these compounds is thought to be critical to the emergence of superconductivity, the ability to view the Fermi surface of these compounds up to and through the transition to a superconductor would be incredibly

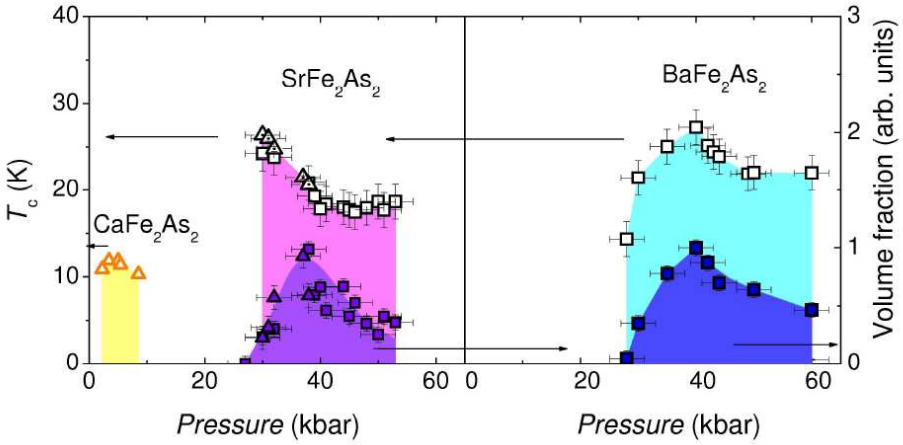

Figure 6.3: From ref. [2]. The transition temperature and superconducting volume fraction of Sr122 and Ba122. The white squares (triangles) show the critical temperature measured by SQUID magnetisation (AC magnetisation). The filled squares (triangles) show the volume fraction measured by SQUID magnetisation (AC magnetisation). The superconducting dome comes from ref. [71]

valuable to elucidating the nature of the mechanism by which this happens.

6.3 Transmission Electron Microscopy

Several of the Sr122 samples grown by me were used in a fascinating exploratory study of the Neel phase transition via Transmission Electron Microscopy (TEM) in the Cambridge Materials Science department. In order to be a first-order transition, two different phases must be seen to coexist. Using thermodynamic probes, this is very difficult to show unambiguously. Via TEM experiments, however, our collaborator was able to record videos in which twin boundary formation and evolution within the crystal (together with hysteresis and needle-twin structure) can be watched as the transition temperature is crossed (figure 6.4), demonstrating directly the first-order nature of the transition in this material.

This coexistence seems to be across quite a wide temperature range, with needle twins forming at temperatures apparently some way below the Neel temperature (with potential consequences for the peaks in inverse Q seen in our RUS measurements. Contrary to intuition, measurements across phase transitions in

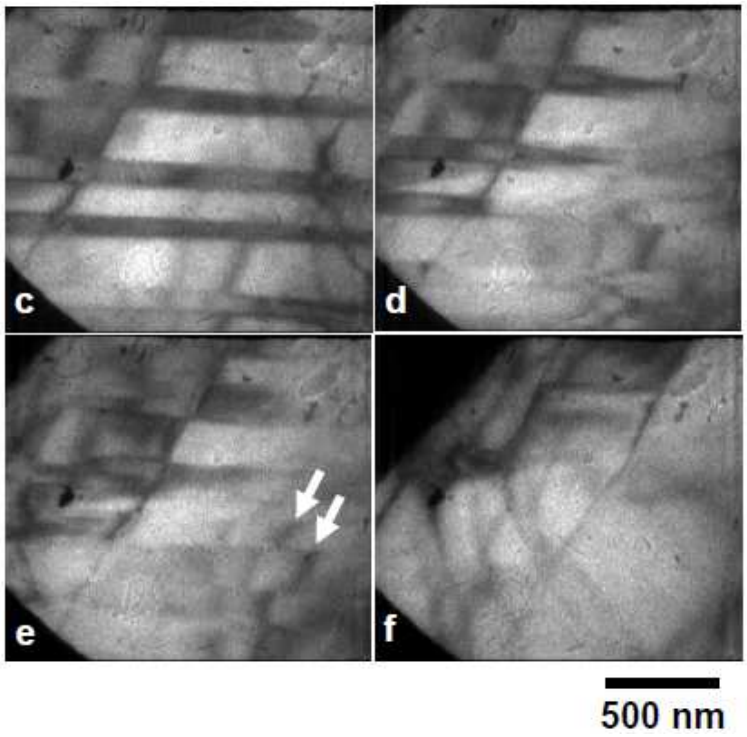

Figure 6.4: From ref. [40]. A bright field image of needle twins withdrawing on warming a crystal in the orthorhombic phase of Sr122. These pictures are nominally taken at c=146.1K, d=146.7K, e=147.0K, d=148.5K, with a total time of 68 seconds elapsing between them. If these temperatures are accurate, an interpretation may be that the withdrawal of the twins leaves behind an orthorhombic but detwinned crystal some way below the transition temperature.

single crystals can often be broader than in polycrystals due to the lack of availability of nucleation sites that occur naturally at polycrystal grain boundaries). In some neutron experiments, remains of these low temperature twins in single crystals have been seen to persist all the way up to 450K [36].

Unfortunately, doped samples currently have too high a dislocation density (thought to be due to the increased disorder in doped materials) to watch twin formation at this stage. We are working on annealing profiles that will hopefully eventually overcome this.

6.4 Inelastic Neutron Scattering

As discussed in section 3.2.4, a significant amount of effort was put into growing very large crystals for inelastic neutron experiments. Collaborators at the ISIS neutron beamline in Oxford invited me to attend the experiments, where I was able to assist with crystal alignment and observe the neutron scattering.

Since a collection of about 20 large crystals was to be used to increase overall crystal mass, these had to be aligned in order that the three crystal axes of each individual crystal were well aligned with the rest of the collection. To achieve this, crystals were added one by one to a growing matrix of crystals using a custom-made crystal mount allowing adjustability about all three rotational axes.

As each crystal was added, we attempted to align it by eye as much as possible to the other crystals. This is easily achieved by eye for the c-axis, since these are plate-like crystals. For the a- and b-axes, however, it is less straight-forward. We looked for any small 90° angles on the crystal surface, which often signified the axes we were looking for (the two are identical in the room-temperature tetragonal state), and the crystal was mounted with these aligned to the a- and b-axes of the other crystals (these will be at 45° to the orthorhombic axes, but as long as all are aligned, and since we have no way of detwinning the crystals below the transition, aligning the tetragonal axes was sufficient).

Once an additional crystal was added, crystals were placed in a white neutron beam for a short period, and diffraction spots measured. Typically we would have several spots for the existing matrix, and new smaller spots nearby for the newly added crystal. The matrix was left to cool for a period then removed, and

the crystal holder for the new crystal was adjusted slightly to move the spots into line. This process was repeated (in a highly time consuming process!) until all of the crystals were mounted.

I and several collaborators operated continuously on a rolling basis for 5 days and eventually mounted 21 single crystals with a mosaic sample of mass 5.4 g, the width of the combined measured Bragg peak for the mosaic was 4° (full-width at half-maximum)[15].

Neutrons as probes of magnetism have already been discussed in section 2.2. There is still considerable debate in the literature, but supported in part by our work, it is being recognised that itinerant models for magnetism can explain the observed magnetic ordered moments in the pnictides without recourse to highly anisotropic coupling parameters invoked by static models[80].

Chapter 7

Conclusion

The four main results of the work presented here are as follows.

1. A robust technique for synthesising high quality Sr122 and Ba122 single crystals via a self-flux technique with a selection of dopants has been established

2. I have mapped the phase diagram of Sr122 with Co-doping up to the end of the superconducting dome

3. In the Sr122 system, no evidence is found of a splitting of the magnetic and structural transitions, which are observed to coexist within experimental resolution to the lowest temperatures. This contrasts to reports of split transitions in the doped Ba122 system.

4. From elastic data, I have shown that the structural transition can be understood as arising from a hidden order parameter sharing the symmetry of the orthorhombic strain, and within this model I have ruled out magnetism as a driver of the transition

The first part of my work was a significant expansion of the QM group's crystal growth capabilities. Difficulties encountered in the growth and characterisation of 122 pnictides proved challenging but not insurmountable. I have been able to grow a very large quantity of high-quality crystals, which have been dispatched around the world for further study, making our group among the top sources for experimentalists wishing to study these materials.

The systems that I have put in place have also increased speed and efficiency for other group members to make their own samples of other materials, and I hope that many more interesting materials will continue to be investigated in the lab.

I await with excitement the arrival of an argon arc-welder. This will allow samples to be sealed in tantalum crucibles and welded shut using an electrical arc at above the melting point of tantalum, allowing for crucibles that can be increased to 1500 °C in our furnaces and for dealing with highly reactive materials. This should allow for a wider range of materials to be grown or used as precursors, for example metallic cobalt for use as a dopant; and the decreased reactivity of tantalum will allow growth of KFe_2As_2 and K-doped Ba122 and Sr122 materials, interesting due to their much higher critical temperatures ($\sim$40K), which I had so much trouble attempting to grow in quartz.

The next part of my work was a thorough exploration of the phase diagram of Sr122 with Cobalt doping. The comparison of this material with its Barium analogue has provided further evidence of the importance of dimensionality in these materials. Similarly to the cuprates, increased 2D character seems to be associated with weaker magnetism and stronger superconducting character. There is also the very interesting question of separateness or coincidence of the structural and magnetic transitions at higher temperature. More detailed work will be needed to elaborate on this further, but of particular interest are TEM measurements of the type described in section 6.3 which are able to visualise such transitions directly.

Finally, I have presented analysis of RUS measurements on four representative materials from this family. We have seen that above the transition, the undoped parent materials display elastic softening as expected for a ferroelastic material approaching a transition driven by a non-strain order parameter with limited (and decreasing with increasing 2-dimensionality) strain coupling. However, rather than recovering below the transition, elastic constants remain almost constant over a significant temperature range. This is an unexpected result, to my knowledge not seen in other materials. Further work is under way to try and better understand what could cause this.

Doped materials are seen to have a much wider broadening region, with all elastic constants behaving similarly. Potentially a more detailed study of intermediate dopings may shed light on the transition between the two types of behaviour, and perhaps on the separation between structural and magnetic transitions as described before. A similar ferroelastic model still seems to predict the behaviour well, but thorough lattice parameter vs T and heat capacity data will be needed for these dopings to extract Landau parameters.

Appendix A

Publications resulting in part or whole from work described in this thesis (most to least recent):

1. H. Z. Arham, C. R. Hunt, W. K. Park, J. Gillett, S. D. Das, S. E. Sebastian, Z. J. Xu, J. S. Wen, Z. W. Lin, Q. Li, G. Gu, A. Thaler, S. L. Budko, P. C. Canfield, L. H. Greene

   Gap-like feature in the normal state of $X(Fe_{1-x}Co_x)_2As_2$, X = Ba, Sr and $Fe_{1+y}Te$ revealed by Point Contact Spectroscopy

   http://arxiv.org/abs/1108.2749

2. M. Sutherland, D. J. Hills, B. S. Tan, M. M. Altarawneh, N. Harrison, J. Gillett, E. C. T. O'Farrell, T. M. Benseman, I. Kokanovic, P. Syers, J. R. Cooper, S. E. Sebastian

   Evidence for Dirac Nodes from Quantum Oscillations in $SrFe_2As_2$

   Submitted to *Physical Review Letters*

   http://arxiv.org/abs/1107.1704

3. R. A. Ewings, T. G. Perring, J. Gillett, S. D. Das, S. E. Sebastian, A. E. Taylor, T. Guidi, A. T. Boothroyd

   Itinerant Spin Excitations in $SrFe_2As_2$ Measured by Inelastic Neutron Scattering

   Phys. Rev. B 83, 214519 (2011)

4. J. Gillett, S. D. Das, P. Syers, A. K. T. Ming, J. I. Espeso, C. M. Petrone, S. E. Sebastian

   Dimensional Tuning of the Magnetic-Structural Transition in $A(Fe_{1-x}Co_x)_2As_2$ (A=Sr,Ba)

   Submitted to *Physical Review B*

   http://arxiv.org/abs/1005.1330

5. J. N. Hancock, S. I. Mirzaei, J. Gillett, S. E. Sebastian, J. Teyssier, R. Viennois, E. Giannini, D. van der Marel

   Strong Coupling to Magnetic Fluctuations in the Charge Dynamics of Fe-Based Superconductors

   Phys. Rev. B 82, 014523 (2010)

6. J. C. Loudon, C. J. Bowell, J. Gillett, S. E. Sebastian, P. A. Midgley

   Determination of the Nature of the Tetragonal to Orthorhombic Phase Transition in $SrFe_2As_2$ by Measurement of the Local Order Parameter

   Phys. Rev. B 81, 214111 (2010)

7. C. L. Zentile, J. Gillett, S. E. Sebastian, J. R. Cooper

   Measurement and Analysis of the Hall Effect of AFe_2As_2 Single Crystals with A = Ba, Ca or Sr

   http://arxiv.org/abs/0911.1259

8. X. Lu, W. K. Park, H. Q. Yuan, G. F. Chen, G. L. Luo, N. L. Wang, A.

S. Sefat, M. A. McGuire, R. Jin, B. C. Sales, D. Mandrus, J. Gillett, S. E. Sebastian, L. H. Greene

Point-Contact Spectroscopic Studies on Normal and Superconducting AFe_2As_2-type Iron-Pnictide Single Crystals

Supercond. Sci. Technol. 23 054009 (2010)

9. F. C. Niestemski, V. B. Nascimento, B. Hu, W. Plummer, J. Gillett, S. E. Sebastian, Z. Wang, V. Madhavan

   Unveiling the Atomic and Electronic Structure at the Surface of the Parent Pnictide $SrFe_2As_2$

   http://arxiv.org/abs/0906.2761

10. P. L. Alireza, Y. T. Chris Ko, J. Gillett, C. M. Petrone, J. M. Cole, S. E. Sebastian, G. G. Lonzarich

    Superconductivity up to 29 K in $SrFe_2As_2$ and $BaFe_2As_2$ at High Pressures

    J. Phys.: Condens. Matter 21 012208 (2008)

11. S. E. Sebastian, J. Gillett, N. Harrison, P. H. C. Lau, C. H. Mielke, G. G. Lonzarich

    Quantum Oscillations in the Parent Magnetic Phase of an Iron Arsenide High Temperature Superconductor

    J. Phys.: Condens. Matter 20 422203 (2008)

Appendix B

Below is a complete list of samples that I grew during my time working on this project. For reasons of space, details are rather limited!

Characterisation Abbreviations:

R - Resistance vs. T sweep performed

C_{p} - Heat Capacity vs. T sweep performed

E_{p} - Sample Electron Microprobed at room temperature

M_{S} - Low-field (typically 5-50Oe) Magnetisation vs. T performed up to 30K

M_{N} - High-field (typically 5T) Magnetisation vs. T performed up to room temperature

Table 1: List of Sample Growths Performed

HMSS Number	Date	Target Compound	Flux	Sealing Method	Result	Characterisation
59		CeFeAsO	Self-flux		No reaction	
60		CePAsO	Self-flux		No reaction	
61		CeFeAsO	Tin		No reaction	
62		CePAsO	Tin		No reaction	
63		SmAs	Self-flux		0.427g SmAs formed	
64	04/05/08	SmFeAsO	Self-flux		Black powder	
65	05/05/08	SmAs	Self-flux			
66		SmFeAsO	Tin		Sn didn't mix with SmFeAsO	
67	09/05/08	SmFeAsO	NaCl:KCl		Flux didn't mix with SmFeAsO	
68		SmFeAsO	NaCl:KCl		Flux didn't mix with SmFeAsO	
69	13/05/08	SmFeAsO	NaCl:KCl		Silvery flux blob	
70	14/05/08	SmFeAsO	Tin		Silvery flux blob	
71	14/05/08	SmFeAsO	Tin		Silvery flux blob	
72	15/05/08	SmAs	Self-flux		SmAs formed	
73	15/05/08	SmAs	Self-flux		SmAs formed	
74	15/05/08	SmAs	Self-flux		SmAs formed	

Table 1 – continued from previous page

HMSS Number	Date	Target Compound	Flux	Sealing Method	Result	Characterisation
75	15/05/08	SmAs	Self-flux		SmAs formed	
76	18/05/08	SmFeAsO	NaCl:KCl		No reaction	
77	21/05/08	SmFeAsO	Self-flux		No reaction	
78	21/05/08	SmFeAsO	Self-flux		No reaction	
79	30/05/08	SmAs	Self-flux		SmAs formed	
80	30/05/08	SmAs	Self-flux		SmAs formed	
81	02/06/08	SmAs	Self-flux		SmAs formed	
82	02/06/08	SmAs	Self-flux		SmAs formed	
83	09/06/08	SmFeAsO	NaCl:KCl			
84	09/06/08	SmFeAsO	NaCl:KCl			
85	09/06/08	SmFeAsO	-			
86	18/06/08	Ba122	Tin	on desk	small crystals	
87	18/06/08	Ba122	Tin	on desk	blob of flux	
88	18/06/08	Sr122	Tin	on desk	Nice crystals 1mm*1mm	R
89	18/06/08	Sr122	Tin	on desk	Nice crystals 1mm*1mm	
90	23/06/08	Sr122	Tin	on desk	Exploded due to high pressure	
91	23/06/08	Sr122	Tin	on desk	Exploded due to high pressure	
92	23/06/08	Sr122	Indium	on desk	Exploded due to high pressure	
93	23/06/08	Sr122	Indium	on desk	Exploded due to high pressure	
94	25/06/08	Sr122	Tin	on desk	No separate crystals	

Table 1 – continued from previous page

HMSS Number	Date	Target Compound	Flux	Sealing Method	Result	Characterisation
95	25/06/08	Sr122	Indium	on desk	V. small crystals formed	
96	25/06/08	Sr122	Tin	on desk	Large crystals, up to 5mm*5mm	
97	25/06/08	Sr122	Indium	on desk	V. small crystals formed	
98		SmFeAsO	-			
99	26/06/08	SmFeAOF	Self-flux		Explosion	
100	26/06/08	SmFeZnAOF	Self-flux			
101	01/07/08	SmAs	Self-flux		SmAs formed	
102	01/07/08	SmAs	Self-flux		SmAs formed	
103	01/07/08	SmAs	Self-flux		SmAs formed	
104	01/07/08	SmAs	Self-flux		SmAs formed	
105	01/07/08	Sr122	Tin	on desk	Lots of large, plate-like crystals	R
106	01/07/08	Sr122	Tin	on desk	Lots of large, plate-like crystals	
107	07/07/08	$SrKFe_2As_2$	Tin	on desk	No crystals	
108	07/07/08	$SrKFe_2As_2$	Tin	on desk	No crystals	
109	07/07/08	$SrKFe_2As_2$	Tin	on desk	No crystals	
110	07/07/08	$SrKFe_2As_2$	Tin	on desk	No crystals	
111	08/07/08	Sr122	Tin		No crystals	
112	08/07/08	Sr122	Tin		No crystals	
141	08/08/08	FeAs	Self-flux		FeAs formed	
142	08/08/08	FeAs	Self-flux		FeAs formed	

Table 1 – continued from previous page

HMSS Number	Date	Target Compound	Flux	Sealing Method	Result	Characterisation
143	08/08/08	FeAs	Self-flux		FeAs formed	
144	09/08/08	Sr122	Tin	on desk	Big crystals!	
145	09/08/08	Sr122	Tin	on desk	No crystals	
146	09/08/08	Sr122	Self-flux	on desk	No crystals	
147	11/08/08	FeAs	Self-flux		FeAs formed	
148	11/08/08	FeAs	Self-flux		FeAs formed	
149	11/08/08	FeAs	Self-flux		FeAs formed	
150	14/08/08	Sr122	Tin	on desk	Small crystals	
151	14/08/08	Sr122	Tin	on desk	Small crystals	
152	14/08/08	Sr122	Self-flux	on desk	No crystals	
159	29/08/08	annealed Sr122	-		Blackened crystals	
160	29/08/08	annealed Sr122	-		Blackened crystals	
161	29/08/08	annealed Sr122	-		Blackened crystals	
162	11/09/08	Sr122	Tin	on desk	No crystals	
163	11/09/08	Sr122	Tin	on desk	No crystals	M_N
164	12/09/08	Sr122	Tin	glovebox	Nice crystals 1mm*1mm	M_N
165	12/09/08	Sr122	Tin	glovebox	Oxidised, no crystals	
166	12/09/08	Sr122	Self-flux	glovebox	No crystals	
167	12/09/08	Sr122	Self-flux	glovebox	Crystals stuck in flux	
168	13/09/08	Ba122	Self-flux	glovebox	Several crystals, flux inclusion	R, M_N

Table 1 – continued from previous page

HMSS Number	Date	Target Compound	Flux	Sealing Method	Result	Characterisation
169	30/09/08	Sr122	Tin	glovebox	Lots of nice crystals	M_N
170	30/09/08	Sr122	Tin	glovebox	Lots of nice crystals	M_N
173	03/10/08	Sr122	Tin	glovebox	Cracked in furnace	
174	03/10/08	Sr122	Tin	glovebox	Lots of nice crystals	
175	05/10/08	Ba122	Self-flux	glovebox	Cracked during spin, gooey mess	
176	05/10/08	Ba122	Self-flux	glovebox	Cracked during spin, gooey mess	
177	09/10/08	Co-doped Sr122	Tin	glovebox	Crystals, seem undoped	
178	23/10/08	Sr122	Tin	glovebox	Nice crystals	
179	23/10/08	Sr122	Tin	glovebox	Oxidised, yellow crystals	
181	26/10/08	Sr122	Tin	glovebox	Bulged, wouldn't spin	
182	29/10/08	Ca122	Tin	glovebox	Broken, cloudy quartz attack	
183	29/10/08	Ca122	Tin	glovebox	Broken, cloudy quartz attack	
184	29/10/08	Ca122	Self-flux	glovebox	Survived, no crystals	
185	29/10/08	Ca122	Self-flux	glovebox	Shattered	
186	31/10/08	Co-doped Sr122	Tin	glovebox	Single v. large crystal	
187	31/10/08	Co-doped Sr122	Tin	glovebox	Many small superconducting crystals	M_N
188	05/11/08	Ca122	Tin	glovebox	No crystals	
189	05/11/08	Ca122	Tin	glovebox	Oxidised, hole in quartz	
190	05/11/08	Ca122	Tin	glovebox	Nice crystals	
191	05/11/08	Ca122	Tin	glovebox	Nice crystals	

Table 1 – continued from previous page

HMSS Number	Date	Target Compound	Flux	Sealing Method	Result	Characterisation
192	05/11/08	Ca122	Self-flux	glovebox	Quartz attacked and cracked, oxidation	
193	05/11/08	Ca122	Self-flux	glovebox	Fine dust, no crystals formed	
194	10/11/08	Ca122	Tin	glovebox	Nice crystals	
195	10/11/08	Ca122	Tin	glovebox	Lots of rod-like phase, few platelike	M_{N}
197	12/11/08	Ca122	Tin	glovebox	Crucible cracked - no crystals	
198	12/11/08	Ca122	Tin	glovebox	Flux not seperated off properly	
199	12/11/08	Ca122	Tin	glovebox	Crucible cracked - no crystals	
200	20/11/08	Co-doped Sr122	Self-flux	glovebox	Swelled up, couldn't spin	
201	20/11/08	Co-doped Sr122	Self-flux	glovebox	Limited swelling, but no crystals	
202	25/11/08	Ca122	Self-flux	glovebox	Some small crystals with flux inclusion	
203	25/11/08	Ca122	Self-flux	glovebox	Some small crystals stuckin flux	M_{N}
204	25/11/08	Ca122	Self-flux	glovebox	Some small crystals with flux inclusion	
205	28/11/08	Sr122	Self-flux	glovebox	Flux only	
206	28/11/08	Sr122	Self-flux	glovebox	Some nice small crystals	M_{N}
207	28/11/08	Co-doped Sr122	Self-flux	glovebox	Flux only	
208	28/11/08	Co-doped Sr122	Self-flux	glovebox	Quartz attacked, no crystals formed	
209	15/12/08	Sr122	Tin	glovebox	Several nice, large crystals	
210	15/12/08	Sr122	Tin	glovebox	Some small crystals	
211	15/12/08	Co-doped Sr122	Tin	glovebox	Many small seemingly undoped crystals	
212	15/12/08	Co-doped Sr122	Tin	glovebox	A few large crystals	M_{N}

Table 1 – continued from previous page

HMSS Number	Date	Target Compound	Flux	Sealing Method	Result	Characterisation
213	15/12/08	Co-doped Sr122	Tin	glovebox	Several small crystals	
214	15/12/08	Co-doped Sr122	Tin	glovebox	One large crystal, several smaller	M_N
215	16/12/08	Co-doped Sr122	Tin	glovebox	Several medium sized crystals	
216	16/12/08	Co-doped Sr122	Tin	glovebox	A few medium sized crystals	M_N
217	16/12/08	Co-doped Sr122	Tin	glovebox	Several small and a few larger crystals	
218	16/12/08	Co-doped Sr122	Tin	glovebox	Several large crystals	
219	18/12/08	Co-doped Sr122	Tin	glovebox	Looks unspun. Repeated with HMSS 230	
220	18/12/08	Co-doped Sr122	Tin	glovebox	Several small crystals	
221	18/12/08	Co-doped Sr122	Tin	glovebox	Several small crystals	M_N
222	18/12/08	Co-doped Sr122	Tin	glovebox	A few smallish crystals	
223	18/12/08	Co-doped Sr122	Self-flux	glovebox	Some crystals stuck in flux lump	
224	18/12/08	Co-doped Sr122	Self-flux	glovebox	Growth swelled: unable to spin	
225	07/01/09	Sr122	Self-flux	glovebox	Some small crystals with lots of flux inclusion	
226	07/01/09	Sr122	Self-flux	glovebox	No flux came off. Reheated - still no crystals	
227	07/01/09	Sr122	Self-flux	glovebox	A few very small crystals	
228	07/01/09	Ca122	Self-flux	glovebox	A few crystals formed	
229	08/01/09	$CaFe_4As_3$	Tin	glovebox	Many rod-like crystals	R, M_N
230	08/01/09	$CaFe_4As_3$	Tin	glovebox	Many intergrown rod-like crystals	
231	08/01/09	Ca122	Self-flux	glovebox	Very many nice but discoloured crystals	
232	08/01/09	Ca122	Self-flux	glovebox	Shattered on spin, no crystals	

Table 1 – continued from previous page

HMSS Number	Date	Target Compound	Flux	Sealing Method	Result	Characterisation
233	08/01/09	Co-doped Ca122	Self-flux	glovebox	Quartz attacked, all shattered on spin	
234	13/01/09	Ca122	Self-flux	glovebox	No crystals, quartz heavily attacked	
235	13/01/09	Ca122	Self-flux	glovebox	Flux seperated but no crystals formed	
237	13/01/09	Co-doped Ca122	Self-flux	glovebox	Lots of large crystals	M_S
238	13/01/09	Co-doped Ca122	Self-flux	glovebox	Cracked on spin, ingredients turned to powder	
239	15/01/09	Sr122	Self-flux	Glovebox	Some large crystals formed	
240	15/01/09	Sr122	Self-flux	Glovebox	Some large crystals formed	R, M_N
241	15/01/09	Co-doped Sr122	Self-flux	Glovebox	No flux seperation. Repeated at 1020, crystals form	R, M_S
242	15/01/09	Co-doped Sr122	Self-flux	Glovebox	No flux seperation	
243	21/01/09	Co-doped Sr122	Tin	Glovebox	Doping hasn't gone into crystals	
244	21/01/09	Co-doped Sr122	Tin	Glovebox	Doping hasn't gone into crystals	
245	21/01/09	Co-doped Sr122	Tin	Glovebox	Cracked on spin	
246	21/01/09	Co-doped Sr122	Tin	Glovebox	Doping hasn't gone into crystals	
247	21/01/09	Co-doped Sr122	Tin	Glovebox	Doping hasn't gone into crystals	M_S
248	21/01/09	Co-doped Sr122	Tin	Glovebox	Doping hasn't gone into crystals	
249	21/01/09	Co-doped Sr122	Self-flux	Glovebox	Quartz cracked, yellowish oxidised crystals formed	
250	21/01/09	Co-doped Sr122	Self-flux	Glovebox	Yellowish oxidised crystals formed, stuck in flux	
251	21/01/09	Co-doped Sr122	Self-flux	Glovebox	Cracked on spin, oxidised lump	
252	21/01/09	Co-doped Sr122	Self-flux	Glovebox	Flux lump with many tiny crystals trapped inside	
253	21/01/09	Co-doped Sr122	Self-flux	Glovebox	Flux lump only	

Table 1 – continued from previous page

HMSS Number	Date	Target Compound	Flux	Sealing Method	Result	Characterisation
254	24/01/09	Co-doped Ca122	Self-flux	Glovebox	Cracked on spin	
255	24/01/09	Co-doped Ca122	Self-flux	Glovebox	Foil like crystals trapped in flux lump	M_{N}, M_{S}
256	24/01/09	Co-doped Ca122	Self-flux	Glovebox	Remains charred and blackened, no crystals	
257	24/01/09	Co-doped Ca122	Self-flux	Glovebox	Some very thin crystals in quartz wool	R
258	03/02/09	Ba122	Self-flux	Glovebox	No crystals formed	
259	03/02/09	Ba122	Self-flux	Glovebox	No crystals formed	
260	03/02/09	Ba122	Self-flux	Glovebox	Large flux lump with tiny crystalline sparkles	
261	03/02/09	Ba122	Self-flux	Glovebox	No crystals formed	
262	08/02/09	Ba122	Self-flux	Glovebox	No spin of - ugly flux lump	
263	08/02/09	Ba122	Self-flux	Glovebox	Exploded in furnace	
264	08/02/09	Co-doped Sr122	Self-flux	Glovebox	Very thin foil-like crystals	R, M_{S}
265	08/02/09	Co-doped Sr122	Self-flux	Glovebox	No crystals formed	
266	12/02/09	Ca122	Self-flux	Glovebox	Many plate-like crystals	
267	12/02/09	Ca122	Self-flux	Glovebox	Flux attacked quartz, all oxidised to black powder	
268	12/02/09	Ca122	Self-flux	Glovebox	Flux attacked quartz, all oxidised to black powder	
269	13/02/09	Co-doped Sr122	Self-flux	Glovebox	Ugly flux lumps, with some very tiny crystals included	
270	13/02/09	Co-doped Sr122	Self-flux	Glovebox	No crystals formed	
271	13/02/09	Co-doped Sr122	Self-flux	Glovebox	No crystals formed	
272	17/02/09	Ca122	Tin	Glovebox	Many crystals but all rod-like phase	
273	17/02/09	Ca122	Tin	Glovebox	Cracked on spin	

Table 1 – continued from previous page

HMSS Number	Date	Target Compound	Flux	Sealing Method	Result	Characterisation
274	17/02/09	Ca122	Tin	Glovebox	Many crystals but all rod-like phase	
275a	19/02/09	Sr122	Self-flux	Glovebox	Melted together. Repeated at 1150, No crystals	
276a	19/02/09	Sr122	Self-flux	Glovebox	Materials melted together then re-run as 276b	
276b	22/02/09	Sr122	-	Glovebox	No crystals formed	
277	23/02/09	Sr122	Self-flux	Glovebox	Final material repeated at 1010. Cracked and oxidised	
278	23/02/09	Ca122	Tin	Glovebox	Many crystals but all rod-like phase	
280	23/02/09	Ca122	Tin	Glovebox	Many crystals but all rod-like phase	
281	25/02/09	Sr122	Self-flux	Glovebox	Some very small crystals	
282	25/02/09	Sr122	Self-flux	Glovebox	Some crystals stuck in flux lump	
283	25/02/09	Sr122	Self-flux	Glovebox	Many small crystals in lower crucible	R
284	04/03/09	Ca122	Tin	Glovebox	Many crystals but all rod-like phase	
285	04/03/09	Ca122	Tin	Glovebox	Many crystals but all rod-like phase	
286	03/03/09	Sr122	Self-flux	Glovebox	Quartz cracked on spin, material oxidised	
287	03/03/09	Sr122	Self-flux	Glovebox	Many nice very small crystals	R
288	03/03/09	Sr122	Self-flux	Glovebox	Many nice very small crystals stuck in flux	
289	09/03/09	Sr122	Self-flux	Glovebox	A few very small crystals stuck in flux	
290	09/03/09	Sr122	Self-flux	Glovebox	A few very small crystals stuck in flux	
291	10/03/09	FeAs	-	On Desk	Not very thorough reaction, some As vapour transport	
292	11/03/09	Ca122	Tin	Glovebox	Intergrown crystals, rod- and plate-like phase	M_{N}
293	12/03/09	Ca122	Tin	Glovebox	Intergrown crystals, rod- and plate-like phase	R

Table 1 – continued from previous page

HMSS Number	Date	Target Compound	Flux	Sealing Method	Result	Characterisation
294	11/03/09	Ca122	Tin	Glovebox	Everything oxidised. Ugly flux lump	
295	12/03/09	Ca122	Tin	Glovebox	Intergrown crystals, rod- and plate-like phase	R
296	13/03/09	FeAs	-	On Desk	Tube cracked, all material blackened	
297a	13/03/09	FeAs	-	On Desk	Lump of silvery material	
297b	16/03/09	FeAs	-	On Desk	Fine silvery powder	
298a	13/03/09	FeAs	-	On Desk	Lump of silvery material	
298b	16/03/09	FeAs	-	On Desk	Fine silvery powder	
299a	17/03/09	FeAs	-	On Desk	Silvery lump	
299b	18/03/09	FeAs	-	On Desk	Silvery pellet of little pieces	
300a	17/03/09	FeAs	-	On Desk	Silvery lump	
300b	18/03/09	FeAs	-	On Desk	Silvery pellet of little pieces	
301a	17/03/09	FeAs	-	On Desk	Silvery lump	
301b	18/03/09	FeAs	-	On Desk	Silvery pellet of little pieces	
302a	17/03/09	FeAs	-	On Desk	Silvery lump	
302b	18/03/09	FeAs	-	On Desk	Silvery pellet of little pieces	
303	17/03/09	Sr122	Self-flux	Glovebox	Many crystals, all rather thin	M_{N}
304	17/03/09	Sr122	Tin	Glovebox	Very thin crystals stuck to crucible	
305	17/03/09	Sr122	Tin	Glovebox	Typical Sn-flux crystals formed	
306	18/03/09	Sr122	Self-flux	Glovebox	Very small crystals stuck in flux	
307	18/03/09	Sr122	Tin	Glovebox	Very small crystals stuck in flux	

Table 1 – continued from previous page

HMSS Number	Date	Target Compound	Flux	Sealing Method	Result	Characterisation
308	18/03/09	Sr122	Tin	Glovebox	Tiny, thick crystals	
309	27/03/09	Sr122	Self-flux	Glovebox	Large flux lump with tiny crystalline sparkles	
310	27/03/09	Sr122	Self-flux	Glovebox	Lower crucible cracked, material leaked out	
311	27/03/09	Sr122	Self-flux	Glovebox	Nice large shiny crystals	
312	27/03/09	Sr122	Self-flux	Glovebox	Large flux lump with tiny crystalline sparkles	
313	27/03/09	Sr122	Self-flux	Glovebox	Large flux lump, no crystals	
314	27/03/09	Sr122	Self-flux	Glovebox	Lots of big intergrown crystals	
315	27/03/09	Sr122	Self-flux	Glovebox	Some large crystals up to 0.18g formed	M_{N}
316	27/03/09	Sr122	Self-flux	Glovebox	Some large crystals up to 0.32g formed	E_{p}, M_{N}
319	06/04/09	KFe_2As_2	Tin	Glovebox	Small crystals with Sn on surface	M_{S}
320	06/04/09	KFe_2As_2	Tin	Glovebox	Small crystals with Sn on surface	
321	09/04/09	Sr122	Tin	Glovebox	Sn didn't leave crystals - large flux blob	
322	09/04/09	Sr122	Tin	Glovebox	Sn didn't leave crystals - large flux blob	
323	10/04/09	KFe_2As_2	Self-flux	Glovebox	Quartz violently attacked by K, oxidation	
324	10/04/09	KFe_2As_2	Self-flux	Glovebox	Quartz violently attacked by K, oxidation	
325a	10/04/09	FeAs	-	On Desk	Silvery lump	
325b	23/04/09	FeAs	-	On Desk	Silvery pellet of little pieces	
326a	10/04/09	FeAs	-	On Desk	Silvery lump	
326b	23/04/09	FeAs	-	On Desk	Silvery pellet of little pieces	
327a	10/04/09	FeAs	-	On Desk	Silvery lump	

Table 1 – continued from previous page

HMSS Number	Date	Target Compound	Flux	Sealing Method	Result	Characterisation
327b	23/04/09	FeAs	-	On Desk	Silvery pellet of little pieces	
328a	10/04/09	FeAs	-	On Desk	Silvery lump	
328b	23/04/09	FeAs	-	On Desk	Silvery pellet of little pieces	
332a	25/04/09	FeAs	-	On Desk	Silvery lump	
332b	26/04/09	FeAs	-	On Desk	Silvery pellet of little pieces	
333a	25/04/09	FeAs	-	On Desk	Silvery lump	
333b	26/04/09	FeAs	-	On Desk	Silvery pellet of little pieces	
334a	25/04/09	FeAs	-	On Desk	Silvery lump	
334b	26/04/09	FeAs	-	On Desk	Silvery pellet of little pieces	
335a	25/04/09	FeAs	-	On Desk	Silvery lump	
335b	26/04/09	FeAs	-	On Desk	Silvery pellet of little pieces	
336a	25/04/09	FeAs	-	On Desk	Silvery lump	
336b	28/04/09	FeAs	-	On Desk	Silvery pellet of little pieces	
337a	25/04/09	FeAs	-	On Desk	Silvery lump	
337b	28/04/09	FeAs	-	On Desk	Silvery pellet of little pieces	
338a	25/04/09	FeAs	-	On Desk	Silvery lump	
338b	28/04/09	FeAs	-	On Desk	Silvery pellet of little pieces	
339a	25/04/09	FeAs	-	On Desk	Silvery lump	
339b	28/04/09	FeAs	-	On Desk	Silvery pellet of little pieces	
340a	29/04/09	FeAs	-	On desk	Exploded in furnace, some salvaged	

Table 1 – continued from previous page

HMSS Number	Date	Target Compound	Flux	Sealing Method	Result	Characterisation
340b	05/05/09	FeAs	-	On desk	Blackened silvery pieces	
341a	29/04/09	FeAs	-	On desk	Silvery lump	
342a	29/04/09	FeAs	-	On desk	Exploded in furnace	
343a	29/04/09	FeAs	-	On desk	Silvery lump	
343b	05/05/09	FeAs	-	On desk	Silvery pieces	
344a	29/04/09	FeAs	-	On desk	Silvery lump	
345a	29/04/09	FeAs	-	On desk	Silvery lump	
346a	29/04/09	FeAs	-	On desk	Silvery lump	
346b	05/05/09	FeAs	-	On desk	Silvery pieces	
347a	30/04/09	FeAs	-	On desk	Silvery lump	
348a	30/04/09	FeAs	-	On desk	Silvery lump	
349a	30/04/09	FeAs	-	On desk	Silvery lump	
349b	05/05/09	FeAs	-	On desk	Silvery pieces	
350a	30/04/09	FeAs	-	On desk	Silvery lump	
351a	30/04/09	FeAs	-	On desk	Silvery lump	
356a	07/05/09	FeAs	-	On desk	Silvery lump	
356b	11/05/09	FeAs	-	On desk	Silvery pieces	
357a	07/05/09	FeAs	-	On desk	Silvery lump	
357b	11/05/09	FeAs	-	On desk	Silvery pieces	
358a	12/05/09	FeAs	-	On desk	Silvery lump	

Table 1 – continued from previous page

HMSS Number	Date	Target Compound	Flux	Sealing Method	Result	Characterisation
358b	19/05/09	FeAs	-	On desk	Silvery pieces	
359a	12/05/09	FeAs	-	On desk	Silvery lump	
359b	19/05/09	FeAs	-	On desk	Silvery pieces	
360a	12/05/09	FeAs	-	On desk	Silvery lump	
360b	15/05/09	FeAs	-	On desk	Silvery pieces	
361a	12/05/09	FeAs	-	On desk	Silvery lump	
361b	19/05/09	FeAs	-	On desk	Silvery pieces	
362a	12/05/09	FeAs	-	On desk	Silvery lump	
362b	15/05/09	FeAs	-	On desk	Silvery pieces	
363a	12/05/09	FeAs	-	On desk	Silvery lump	
363b	15/05/09	FeAs	-	On desk	Silvery pieces	
364	14/05/09	Sr122	Self-flux	Glovebox	Serveral large crystals in lower crucible	
365	14/05/09	Sr122	Self-flux	Glovebox	Very small crystals formed	
366	14/05/09	Sr122	Self-flux	Glovebox	Many small and a few medium sized crystals	
367	14/05/09	Sr122	Self-flux	Glovebox	Several large crystals formed	
368	14/05/09	Sr122	Self-flux	Glovebox	Several large crystals formed (largest 0.2g)	M_{N}
369	14/05/09	Sr122	Self-flux	Glovebox	Lower crucible cracked during growth	
370	17/05/09	Sr122	Self-flux	Glovebox	Several large crystals formed (largest 0.2g)	
371	17/05/09	Sr122	Self-flux	Glovebox	Exploded in furnace	
372	17/05/09	Polycrystalline Sr122	Self-flux	Glovebox	Polycrystalline precursor material	

Table 1 – continued from previous page

HMSS Number	Date	Target Compound	Flux	Sealing Method	Result	Characterisation
373	17/05/09	Polycrystalline Sr122	Self-flux	Glovebox	Polycrystalline precursor material	
374a	17/05/09	FeAs	-	On desk	Silvery lump	
374b	17/05/09	FeAs	-	On desk	Exploded in furnace	
375	18/05/09	Sr122	Self-flux	Glovebox	Many small crystals formed	
376	18/05/09	Sr122	Self-flux	Glovebox	Crystals stuck in flux, couldn't remove	
377a	21/05/09	FeAs	-	On desk	Silvery lump	
377b	26/05/09	FeAs	-	On desk	Exploded in furnace	
378a	21/05/09	FeAs	-	On desk	Silvery lump	
378b	26/05/09	FeAs	-	On desk	Exploded in furnace	
379a	21/05/09	FeAs	-	On desk	Silvery lump	
379b	26/05/09	FeAs	-	On desk	Silvery pieces	
380a	21/05/09	FeAs	-	On desk	Exploded in furnace	
381	22/05/09	Sr122	Self-flux	Glovebox	Cracked during spin, oxidised	
382	22/05/09	Sr122	Self-flux	Glovebox	Cracked on spin, large crystals survived but oxidised	
383	22/05/09	Sr122	Self-flux	Glovebox	Some large (up to 0.32g) crystals formed	M_{N}
384	29/05/09	Sr122	Self-flux	Glovebox	Some large (up to 0.2g) crystals formed	
385	29/05/09	Sr122	Self-flux	Glovebox	Some large (up to 0.33g) crystals formed	
386	29/05/09	Sr122	Self-flux	Glovebox	Some large (up to 0.35g) crystals formed	M_{N}
387a	27/05/09	FeAs	-	On desk	Silvery lump	
387b	27/05/09	FeAs	-	On desk	Silvery pieces	

Table 1 – continued from previous page

HMSS Number	Date	Target Compound	Flux	Sealing Method	Result	Characterisation
390a	27/05/09	FeAs	-	On desk	Silvery lump	
390b	02/06/09	FeAs	-	On desk	Silvery pieces	
391a	27/05/09	FeAs	-	On desk	Silvery lump	
391b	01/06/09	FeAs	-	On desk	Silvery pieces	
393a	29/05/09	FeAs	-	On desk	Silvery lump	
393b	01/06/09	FeAs	-	On desk	Silvery pieces	
395	29/05/09	Sr122	Self-flux	Glovebox	Some large (up to 0.2g) crystals formed	M_{N}
396	30/05/09	Sr122	Self-flux	Glovebox	Flux leaked during growth, no crystal formation	
397	30/05/09	Sr122	Self-flux	Glovebox	Many small crystals formed	
398	02/06/09	Sr122	Self-flux	Glovebox	Some large (up to 0.24g) crystals formed	
399	02/06/09	Sr122	Self-flux	Glovebox	One very large 0.55g crystal! Many smaller crystals	M_{N}
400	03/06/09	Sr122	Self-flux	Glovebox	Many small crystals formed	
401	03/06/09	Sr122	Self-flux	Glovebox	Some large (up to 0.25g) crystals formed	M_{N}
402	03/06/09	Sr122	Self-flux	Glovebox	Several medium sized crystals up to 0.15g formed	
403	04/06/09	Sr122	Self-flux	Glovebox	Largest quartz used. Didn't react - repeated as 403b	
403b	09/06/09	Sr122	Self-flux	Glovebox	Several large crystals up to 0.4g formed	
404	04/06/09	Sr122	Self-flux	Glovebox	Several medium sized crystals up to 0.15g formed	M_{N}
405	04/06/09	Sr122	Self-flux	Glovebox	Several medium sized crystals up to 0.17g formed	
406	09/06/09	Sr122	Self-flux	Glovebox	Many nice but small crystals formed	
407	09/06/09	Sr122	Self-flux	Glovebox	Many nice but small crystals formed	R, E_{p}

Table 1 – continued from previous page

HMSS Number	Date	Target Compound	Flux	Sealing Method	Result	Characterisation
408	09/06/09	Sr122	Self-flux	Glovebox	Many nice but small crystals formed	
409	09/06/09	Sr122	Self-flux	Glovebox	Many nice but small crystals formed	
418	06/07/09	KFe_2As_2	Self-flux	Glovebox	K attacked quartz. FeAs survived but K gone. No crystals	
418”	14/07/09	Sr122	Self-flux	Glovebox	Several medium sized crystals up to 0.07g formed	R
419	14/07/09	Sr122	Self-flux	Glovebox	Several medium sized crystals up to 0.1g formed	R, M_N
420	14/07/09	Sr122	Self-flux	Glovebox	Blackened and charred remains - no crystals	
421	14/07/09	Sr122	Self-flux	Glovebox	Dropped during spin, cracked	
422	14/07/09	Sr122	Self-flux	Glovebox	Blackened and charred remains - no crystals	
426	16/07/09	KFe_2As_2	Self-flux	Glovebox	Quartz attacked. No crystals visable, sparkly flux lump	
427a	16/07/09	FeAs	-	On desk	Silvery lump	
427b	23/07/09	FeAs	-	On desk	Silvery pieces	
428a	16/07/09	FeAs	-	On desk	Silvery lump	
428b	23/07/09	FeAs	-	On desk	Silvery pieces	
429	20/07/09	Ba122	Self-flux	Glovebox	Flux leacked during spinning, no crystals - T too high?	
430	20/07/09	Ba122	Self-flux	Glovebox	Flux leacked during spinning, no crystals - T too high?	
431	24/07/09	Co-doped Sr122	Self-flux	Glovebox	Cracked on spin, several yellowed crystals recovered	R, E_p, M_N
432	24/07/09	Co-doped Sr122	Self-flux	Glovebox	Many large crystals formed	R, E_p, M_S, M_N
433	24/07/09	Co-doped Sr122	Self-flux	Glovebox	Many large crystals formed	R, E_p, M_S
434	24/07/09	Co-doped Sr122	Self-flux	Glovebox	Many crystals formed	R, E_p, M_S
435a	24/07/09	FeAs	-	On desk	Silvery lump	

Table 1 – continued from previous page

HMSS Number	Date	Target Compound	Flux	Sealing Method	Result	Characterisation
436a	24/07/09	FeAs	-	On desk	Silvery lump	
437a	28/07/09	FeAs	-	On desk	Silvery lump	
438a	28/07/09	FeAs	-	On desk	Silvery lump	
439a	28/07/09	FeAs	-	On desk	Silvery lump	
440a	28/07/09	FeAs	-	On desk	Silvery lump	
444	14/08/09	Co-doped Sr122	Self-flux	Glovebox	Many large crystals formed	R, E_{p}, M_{S}
445	14/08/09	Co-doped Sr122	Self-flux	Glovebox	Many large crystals formed	R, E_{p}, M_{S}
446	14/08/09	Co-doped Sr122	Self-flux	Glovebox	Many large crystals formed	R, E_{p}, M_{S}
447	14/08/09	Co-doped Sr122	Self-flux	Glovebox	Many crystals formed	R, E_{p}, M_{S}
448b	10/10/09	FeAs	-	On desk	Silvery pieces	
449b	10/10/09	FeAs	-	On desk	Silvery pieces	
450b	10/10/09	FeAs	-	On desk	Silvery pieces	
451b	10/10/09	FeAs	-	On desk	Silvery pieces	
460	21/09/09	Ba122	Self-flux	Glovebox	Many nice crystals formed	R, E_{p}, M_{N}
464	21/09/09	Sr122	Self-flux	Glovebox	Many nice crystals formed	R, E_{p}, M_{N}
465	21/09/09	Sr122	Self-flux	Glovebox	Many nice crystals formed	R, E_{p}, M_{N}
466	21/09/09	Sr122	Self-flux	Glovebox	Many nice crystals formed	R, C_{p}, E_{p}, M_{N}
467	21/09/09	Sr122	Self-flux	Glovebox	Many nice crystals formed	R, E_{p}, M_{N}
468	25/09/09	CoAs	-	On desk	Exploded in furnace	
469	01/10/09	Co-doped Sr122	Self-flux	Glovebox	Nice, large crystals (up to 0.33g) formed	R, E_{p}, M_{S}

Table 1 – continued from previous page

HMSS Number	Date	Target Compound	Flux	Sealing Method	Result	Characterisation
470	01/10/09	Co-doped Sr122	Self-flux	Glovebox	Nice, medium crystals (up to 0.14g) formed	R, E_p, M_S
471	02/10/09	Co-doped Sr122	Self-flux	Glovebox	Nice medium sized crystals formed	R, C_p, E_p, M_N
472	02/10/09	Co-doped Sr122	Self-flux	Glovebox	Cracked on spin, crystals heavily oxidised	
473	02/10/09	Co-doped Sr122	Self-flux	Glovebox	Nice medium sized crystals formed	R, C_p, E_p, M_N
474	02/10/09	Co-doped Sr122	Self-flux	Glovebox	Nice medium sized crystals formed	R, C_p, E_p, M_N
475	29/09/09	Annealed Sr122	-	On desk	Crystals went in shiney but came out blackened	R, M_N
476	07/10/09	CoAs	-	On desk	Explosion!	
478	13/07/09	KFe_2As_2	Self-flux	Glovebox	Eventually succeeded! Crystals!	R, E_p, M_S
480	14/10/09	Co-doped Sr122	Self-flux	Glovebox	Several small crystals formed	R, E_p, C_p, M_N
481	14/10/09	Co-doped Sr122	Self-flux	Glovebox	Many crystals formed	R, E_p
482	14/10/09	Co-doped Sr122	Self-flux	Glovebox	Many crystals formed	R, E_p, M_S
483	14/10/09	Co-doped Sr122	Self-flux	Glovebox	Many crystals formed	R, E_p, M_S
484	15/10/09	Co-doped Sr122	Self-flux	Glovebox	Many crystals formed	R, E_p, M_S
485	15/10/09	Co-doped Sr122	Self-flux	Glovebox	Many crystals formed	R, C_p, E_p, M_S
486	15/10/09	Co-doped Sr122	Self-flux	Glovebox	Some cracking - crystals oxidised	
487	15/10/09	Co-doped Sr122	Self-flux	Glovebox	No crystals	
488a	22/10/09	FeAs	-	On desk	Silvery lump	
488b	27/10/09	FeAs	-	On desk	Silvery lump	
489a	22/10/09	FeAs	-	On desk	Silvery lump	
489b	27/10/09	FeAs	-	On desk	Silvery lump	

Table 1 – continued from previous page

HMSS Number	Date	Target Compound	Flux	Sealing Method	Result	Characterisation
490	23/10/09	Co-doped Sr122	Self-flux	Glovebox	Many crystals formed	R, E_{p}, M_{S}
491	23/10/09	Co-doped Sr122	Self-flux	Glovebox	Many crystals formed	R, E_{p}, M_{S}
492	23/10/09	Co-doped Sr122	Self-flux	Glovebox	A few crystals formed	R, E_{p}, M_{S}
493	23/10/09	Co-doped Sr122	Self-flux	Glovebox	Many crystals formed	R, E_{p}, M_{S}
495a	27/10/09	FeAs	-	On desk	Silvery lump	
495b	10/11/09	FeAs	-	On desk	Silvery lump	
496a	27/10/09	FeAs	-	On desk	Silvery lump	
496b	10/11/09	FeAs	-	On desk	Silvery lump	
497	27/10/09	Co-doped Sr122	Self-flux	Glovebox	Many crystals formed	R, C_{p}, E_{p}, M_{N}
499a	30/10/09	FeAs	-	On desk	Silvery lump	
500a	05/11/09	FeAs	-	On desk	Silvery lump	
500b	20/11/09	FeAs	-	On desk	Silvery lump	
501	09/11/09	Co-doped Sr122	Self-flux	Glovebox	Many, large crystals formed	R, C_{p}, E_{p}, M_{N}
502	09/11/09	Co-doped Sr122	Self-flux	Glovebox	Many crystals formed	R, C_{p}, E_{p}, M_{N}
505	24/11/09	Co-doped Sr122	Self-flux	Glovebox	Many crystals formed	R, E_{p}, M_{N}
506	24/11/09	Co-doped Sr122	Self-flux	Glovebox	Many crystals formed	R, E_{p}, M_{N}
507a	27/11/09	FeAs	-	On desk	Silvery lump	
511	16/12/09	Co-doped Ba122	Self-flux	Glovebox	Cracked on spin	
512	16/12/09	Co-doped Ba122	Self-flux	Glovebox	Many crystals formed	R, E_{p}, C_{p}
513	17/12/09	Annealed Sr122	-	On desk	Annealed crystals	

Table 1 – continued from previous page

HMSS Number	Date	Target Compound	Flux	Sealing Method	Result	Characterisation
514	17/12/09	Annealed Sr122	-	On desk	Annealed crystals	
515	17/12/09	Annealed Sr122	-	On desk	Annealed crystals	
522'	12/01/10	Annealed Sr122	-	On desk	Annealed crystals	R
523'	12/01/10	Annealed Sr122	-	On desk	Annealed crystals	R, E_{p}
524'	12/01/10	Annealed Sr122	-	On desk	Annealed crystals	
525	12/01/10	Annealed Sr122	-	On desk	Annealed crystals	
526	12/01/10	Annealed Ba122	-	On desk	Annealed crystals	
527	12/01/10	Annealed Ba122	-	On desk	Annealed crystals	
532	01/02/10	Co-doped Ba122	Self-flux	Glovebox	Many crystals formed	R
533	01/02/10	Co-doped Ba122	Self-flux	Glovebox	Many crystals formed	R
540	15/02/10	Annealed Doped Sr122	-	On desk	Annealed crystals	R
541	15/02/10	Annealed Doped Sr122	-	On desk	Annealed crystals	R
542	15/02/10	Annealed Doped Sr122	-	On desk	Annealed crystals	R
543	15/02/10	Annealed Doped Sr122	-	On desk	Annealed crystals	R
554a	15/02/10	$BaCu_2S_2$	Self-flux	Glovebox	Pellet	M_{N}, M_{S}
554b	25/02/10	$BaCu_2S_2$	-	Glovebox	Pellet	
555a	15/02/10	$BaCu_2S_2$	Self-flux	Glovebox	Pellet - crystals visible!	M_{N}, M_{S}
555b	25/02/10	$BaCu_2S_2$	-	Glovebox	Pellet	
556a	15/02/10	$BaCu_2S_2$	Self-flux	Glovebox	Pellet - crystals visible!	M_{N}, M_{S}
550	20/02/10	Annealed Doped Sr122	-	On desk	Annealed crystals	R

Table 1 – continued from previous page

HMSS Number	Date	Target Compound	Flux	Sealing Method	Result	Characterisation
551	20/02/10	Annealed Doped Sr122	-	On desk	Annealed crystals	R
552	20/02/10	Annealed Doped Sr122	-	On desk	Annealed crystals	R, M_S
553	20/02/10	Annealed Doped Sr122	-	On desk	Annealed crystals	R
554	20/02/10	Annealed Doped Sr122	-	On desk	Annealed crystals	R
555	20/02/10	Annealed Doped Ba122	-	On desk	Annealed crystals	R
562	04/03/10	Sr122	Self-flux	Glovebox	Very large crystals formed	
563	04/03/10	Sr122	Self-flux	Glovebox	Very large crystals formed	
564	04/03/10	Annealed Doped Ba122	-	On desk	Annealed crystals	R
565	04/03/10	Annealed Doped Ba122	-	On desk	Annealed crystals	R
573a	17/03/10	FeAs	-	On desk	Explosion!	
574a	17/03/10	FeAs	-	On desk	Explosion!	
575a	17/03/10	FeAs	-	On desk	Explosion!	
576a	17/03/10	FeAs	-	On desk	Explosion!	
577a	17/03/10	FeAs	-	On desk	Explosion!	
578a	17/03/10	FeAs	-	On desk	Survived, silvery lumps formed	
578b	03/04/10	FeAs	-	On desk	Silvery lumps formed	
579	18/03/10	$BaCu_2S_2$	Self-flux	Glovebox	Only tiny crystallites form	
580	18/03/10	$BaCu_2S_2$	Self-flux	Glovebox	Tiny micro-crystals	
582	18/03/10	$SrCu_2S_2$	Self-flux	Glovebox	Lump, no visible crystals	
583	18/03/10	$BaCu_2S_2$	Self-flux	Glovebox	Flux lump with tiny sparkles	

Table 1 – continued from previous page

HMSS Number	Date	Target Compound	Flux	Sealing Method	Result	Characterisation
588	28/03/10	Sr122	Self-flux	Glovebox	Immense swelling, can't spin	
589	28/03/10	Sr122	Self-flux	Glovebox	Major swelling, can't spin	
591	07/04/10	Sr122	Self-flux	Glovebox	Major swelling, can't spin	

Appendix C

When considering linear deformations of a general 3-dimensional crystal, it is convenient to define a strain tensor to map the locations of points on the old lattice to those on the new lattice

$$[e_{ij}] \begin{pmatrix} x \\ y \\ z \end{pmatrix} = \begin{pmatrix} x' \\ y' \\ z' \end{pmatrix} \tag{1}$$

Such a strain must be a rank-2 symmetric tensor of dimension three

$$[e_{ij}] = \begin{bmatrix} e_{11} & e_{12} & e_{13} \\ e_{12} & e_{22} & e_{23} \\ e_{13} & e_{23} & e_{33} \end{bmatrix} \tag{2}$$

Where the indices $i, j = 1, 2, 3$ refer to the original axes x,y,z. However, the large number of indices rapidly becomes unwieldy and Voigt notation is introduced to reduce the number of subscripts. In Voigt notation, $e_{11} \rightarrow e_1$, $e_{22} \rightarrow e_2$ and so on as below (now $1 \geq i \geq 6$)

$$[e_i] = \begin{bmatrix} e_1 & \frac{1}{2}e_6 & \frac{1}{2}e_5 \\ \frac{1}{2}e_6 & e_2 & \frac{1}{2}e_4 \\ \frac{1}{2}e_5 & \frac{1}{2}e_4 & e_3 \end{bmatrix} \tag{3}$$

When considering a tetragonal $\rightleftharpoons$ orthorhombic transition, we will need to rotate the strain tensor by 45° using the conventional procedure for rotating

tensors

$$[e_{i,\text{ortho}}] = R[e_{i,\text{tet}}]R^T \tag{4}$$

with

$$R = \frac{1}{\sqrt{2}}\begin{bmatrix} 1 & -1 & 0 \\ 1 & 1 & 0 \\ 0 & 0 & \sqrt{2} \end{bmatrix} \tag{5}$$

For the transition we consider here, only e_6 and e_3 are non-zero. Applying rotation R gives

$$[e_{i,\text{ortho}}] = \frac{1}{2}\begin{bmatrix} -e_6 & 0 & 0 \\ 0 & e_6 & 0 \\ 0 & 0 & 2e_3 \end{bmatrix} \tag{6}$$

We see that the tetragonal strain is diagonalised in the orthorhombic axes - the strain leads to a contraction of one orthorhombic ab axes and an extension of the other. We can also see that the transition is symmetric in e_6 - the sign of the tetragonal strain only picks the longer and shorter axes of the local orthorhombic domain.

References

[1] K. Ahilan, F. L. Ning, T. Imai, A. S. Sefat, M. A. McGuire, B. C. Sales, and D. Mandrus. Electronic phase diagram of the iron-based high- T_c superconductor $Ba(Fe_{1-x}Co_x)_2As_2$ under hydrostatic pressure ($0 \leq x \leq 0.099$). *Phys. Rev. B*, **79**:214520, 2009. 40, 53

[2] P. L. Alireza, Y. T. C. Ko, J. Gillett, C. M. Petrone, J. M. Cole, S. E. Sebastian, and G. G. Lonzarich. Superconductivity up to 29 K in $SrFe_2As_2$ and $BaFe_2As_2$ at high pressures. *J. Phys.: Condensed Matter*, **21**:012208, 2009. 6, 35, 39, 53, 88, 89

[3] N. P. Butch, S. R. Saha, X. H. Zhang, K. Kirshenbaum, R. L. Green, and J. Paglione. Effective carrier type and field dependence of the reduced-t_c superconducting state in $SrFe_{2-x}Ni_xAs_2$. *Phys. Rev. B 81*, page 024518, 2010. 55

[4] P. C. Canfield, S. L. Budko, N. Ni, J. Q. Yan, and A. Kracher. Decoupling of the superconducting and magnetic/structural phase transitions in electron-doped $BaFe_2As_2$. *Phys. Rev. B*, **80**:060501(R), 2009. 7, 39

[5] P. C. Canfield and Z. Fisk. *Phil. Mag. B*, pages 65, 1117, 1992. 13

[6] Paul C. Canfield and Sergey L. Bud'ko. *Annu. Rev. Condens. Matter Phys.*, **1**:11, 2010. 49

[7] A. Cano, M. Civelli, I. Eremin, and I. Paul. Interplay of magnetic and structural transitions in Iron-based Pnictide superconductors. *Phys. Rev. B 82*, page 020408(R), 2010. 12, 53

[8] M. A. Carpenter and E. K. H. Salje. Elastic anomalies in minerals due to structural phase transitions. *Eur. J. Mineral.*, **10**:693–812, 1998. 62, 82

[9] M. A. Carpenter, E. K. H. Salje, and A. Graeme-Barber. Spontaneous strain as a determinant of thermodynamic properties for phase transitions in minerals. *Eur. J. Mineral.*, **10**:621–691, 1998. 62, 64

[10] X. H. Chen, T. Wu, G. Wu, R. H. Liu, H. Chen, and D. F. Fang. Superconductivity at 43K in $SmFeAsO_{1-x}F_x$. *Nature 453*, page 761, 2008. 1

[11] J.-H. Chu, J. G. Analytis, K. D. Greve, P. L. McMahon, Z. Islam, Y. Yamamoto, and I. R. Fisher. Evidence for an electron nematic phase transition in underdoped Iron Pnictide superconductors. *Science*, **329**:824–826, 2010. 50

[12] J.-H. Chu, J. G. Analytis, C. Kucharczyk, and I. R. Fisher. Determination of the phase diagram of the electron-doped superconductor $Ba(Fe_{1-x}Co_x)_2As_2$. *Phys. Rev. B*, **79**:014506, 2009. v, 9, 40, 48, 51

[13] E. Colombier, M. S. Torikachvili, N. Ni, A. Thaler, S. L. Budko, and P C Canfield. Electrical transport measurements under pressure for $BaFe_2As_2$ compounds doped with Co, Cr, or Sn. *Supercond. Sci. Technol. 23*, page 054003, 2010. 53

[14] K. Deguchi, Y. Mizuguchi, Y. Kawasaki, T. Ozaki, S. Tsuda, T. Yamaguchi, and Y. Takano. Alcoholic beverages induce superconductivity in $FeTe_{1-x}S_x$. *Supercond. Sci. Technol. 24*, page 055008, 2011. 1

[15] R. A. Ewings, T. G. Perring, J. Gillett, S. D. Das, S. E. Sebastian, A. E. Taylor, T. Guidi, and A. T. Boothroyd. Itinerant spin

excitations in $SrFe_2As_2$ measured by inelastic neutron scattering. *Phys. Rev. B 83*, page 214519, 2011. 92

[16] C. Fang, H. Yao, W. F. Tsai, J. P. Hu, and S. A. Kivelson. Theory of electron nematic order in LaOFeAs. *Phys. Rev. B*, **77**:224509, 2008. 50

[17] R. M. Fernandes, L. H. VanBebber, S. Bhattacharya, P. Chandra, V. Keppens, D. Mandrus, M. A. McGuire, B. C. Sales, A. S. Sefat, and J. Schmalian. Effect of nematic fluctuations on the elastic properties of iron arsenide superconductors. *Phys. Rev. Lett. 105*, page 157003, 2010. 84

[18] J. Gillett, S. D. Das, P. Syers, A. K. T. Ming, J. E. Espeso, C. Petrone, and S. E. Sebastian. Dimensional Tuning of the Magnetic-Structural Transition in $A(Fe_{1-x}Co_x)_2As_2$ (A=Sr,Ba). *arXiv*, page 1005.1330, 2010. 2

[19] H. Hiramatsu, T. Katase, T. Kamiya, M. Hirano, and H. Hosono. Water-induced superconductivity in $SrFe_2As_2$. *Phys. Rev. B*, **80**:052501, 2009. 18, 40

[20] F-C Hsu, J-Y Luo, K-W Yeh, T-K Chen, T-W Huang, P. M. Wu, Y-C Lee, Y-L Huang, Y-Y Chu, D-C Yan, and M-K Wu. Superconductivity in the PbO-type structure α-FeSe. *Proc. Nat. Acad. Sci. USA*, pages vol. 105 no. 38 14262–14264, 2008. 5

[21] W. Z. Hu, J. Dong, G. Li, Z. Li, P. Zheng, G. F. Chen, J. L. Luo, and N. L. Wang. Origin of the spin density wave instability in AFe_2As_2 (A=Ba,Sr) as revealed by optical spectroscopy. *Phys. Rev. Lett. 101*, page 257005, 2008. 9

[22] M. A. Itskovsky, T. Maniv, and I. D. Vagner. de Haas van Alphen (dHvA) effect in two-dimensional (2D) conductors: susceptibility oscillations. *Z. Phys. B*, pages 101, 1322, 1996. 85

[23] A. Jesche, C. Krellner, M. de Souza, M. Lang, and C.Geibel. Coupling between the structural and magnetic transition in CeFeAsO. *Phys. Rev. B*, **81**:134525, 2010. 9, 18

[24] D. C. Johnston. The puzzle of high temperature superconductivity in layered iron pnictides and chalcogenides. *Adv. Phys. 59*, page 803, 2010. 10

[25] Y. Kamihara, T. Watanabe, M. Hirano, and H. Hosono. Iron-based layered superconductor La($O_{1-x}F_x$)FaAs (x = 0.05 - 0.12) with T_c = 26K. *J. Am. Chem. Soc.*, **130**:3296, 2008. 1, 39

[26] Y. Kamiya, N. Kawashima, and C. D. Batista. Crossover behavior from decoupled criticality. *Phys. Rev. B 82*, page 054426, 2010. 50

[27] T. Kariyado and M. Ogata. Normal-state spin dynamics of five-band model forIron Pnictides. *Phys. Soc. Jpn. 78*, page 043708, 2009. 10

[28] S. A. J. Kimber, A. Kreyssig, Y. Z. Zhang, H. O. Jeschke, R Valent, F. Yokaichiya, E. Colombier, J. Yan, T. C. Hansen, T. Chatterji, R. J. McQueeney, P. C. Canfield, A. I. Goldman, and D. N. Argyriou. Similarities between structural distortions under pressure and chemical doping in superconducting $BaFe_2As_2$. *Nature Materials*, **8**:471, 2009. 7

[29] J. Knolle, I. Eremin, A. V. Chubukov, and R. Moessner. Theory of itinerant magnetic excitations in the SDW phase of Iron-based superconductors. *Phys. Rev. B*, **81**:140506, 2010. 9, 46

[30] M. M. Korshunov, I. Eremin, D. V. Efremov, D. L. Maslov, and A. V. Chubukov. Nonanalytic spin susceptibility of a fermi liquid: The case of Fe-based Pnictides. *Phys. Rev. Lett. 102*, page 236403, 2009. 27

[31] H. Kotegawa, T. Kawazoe, H. Sugawara, K. Murata, and H. Tou. Effect of uniaxial stress for pressure-induced superconductor $SrFe_2As_2$. *J. Phys. Soc. Japan*, **78**:083702, 2009. 46

[32] C. Krellner, N. Caroca-Canales, A. Jesche, H. Rosner, A. Ormeci, and C. Geibel. Magnetic and structural transitions in layered FeAs systems: AFe_2As_2 versus RFeAsO compounds. *Phys. Rev. B*, **78**[10]:100504(R), 2008. 50

[33] M. Kumar, M. Nicklas, A. Jesche, N. Caroca-Canales, M. Schmitt, M. Hanfland, D. Kasinathan, U. Schwarz, H. Rosner, and C. Geibel. Effect of pressure on the magnetostructural transition in $SrFe_2As_2$. *Phys. Rev. B*, **78**:184516, 2008. 53

[34] C.-H. Lee, A. Iyo, H. Eisaki, H. Kito, M. T. Fernandez-Diaz, T. Ito, K. Kihou, H. Matsuhata, M. Braden, and K. Yamada. Effect of structural parameters on superconductivity in Fluorine-free $LnFeAsO_{1-y}$ (Ln = La, Nd). *J. Phys. Soc. Japan*, **77**:083704, 2008. 7

[35] A. Leithe-Jasper, W. Schnelle, C. Geibel, and H. Rosner. Superconducting state in $SrFe_{2-x}Co_xAs_2$ by internal doping of the Iron Arsenide layers. *Phys. Rev. Lett.*, **101**:207004, 2008. 2, 40, 44

[36] H. Li, W. Tian, J. L. Zarestky, A. Kreyssig, N. Ni, S. L. Budko, P. C. Canfield, A. I. Goldman, R. J. McQueeney, and D. Vaknin. Magnetic and lattice coupling in single-crystal $SrFe_2As_2$: A neutron scattering study. *Phys. Rev. B 80*, page 054407, 2009. 12, 91

[37] H. Li, W. Tian, J. L. Zarestky, A. Kreyssig, N. Ni, S. L. Budko, P. C. Canfield, A. I. Goldman, R. J. McQueeney, and D. Vaknin. Magnetic and lattice coupling in single-crystal $SrFe_2As_2$: A neutron scattering study. *Phys. Rev. B 80*, page 054407, 2009. 73

[38] C. Liu, T. Kondo, N. Ni, A. D. Palczewski, A. Bostwick, G. D. Samolyuk, R. Khasanov, M. Shi, E. Rotenberg, S. L. Budko, P. C. Canfield, and A. Kaminski. Three- to two-dimensional transition of the electronic structure in $CaFe_2As_2$ - parent compound for an Iron Arsenic high temperature superconductor. *Phys. Rev. Lett.*, **102**:167004, 2009. 50

[39] R. H. Liu, T. Wu, G. Wu, H. Chen, X. F. Wang, Y. L. Xie, J. J. Ying, Y. J. Yan, Q. J. Li, B. C. Shi, W. S. Chu, Z. Y. Wu, and X. H. Chen. A large iron isotope effect in $SmFeAsO_{1-x}F_x$ and $Ba_{1-x}K_xFe_2As_2$. *Nature 459*, page 64, 2009. 82

[40] J.C. Loudon, C.J. Bowell, J. Gillett, S.E. Sebastian, and P.A. Midgley. Determination of the nature of the tetragonal to orthorhombic phase transition in $SrFe_2As_2$ by measurement of the local order parameter. *Phys. Rev. B 81*, page 214111, 2010. 50, 90

[41] Weicheng Lv, Jiansheng Wu, and Philip Phillips. Orbital ordering induces structural phase transition and the resistivity anomaly in Iron Pnictides. *Phys. Rev. B*, **80**[22]:224506, 2009. 50

[42] L. Malone, J. D. Fletcher, A. Serafin, A. Carrington, N. D. Zhigadlo, Z. Bukowski, S. Katrych, and J. Karpinski. Magnetic penetration depth of single crystal $SmFeAsO_{1-x}F_y$: a fully gapped superconducting state. *Phys. Rev. B 79*, page 140501(R), 2009. 10

[43] I. I. Mazin, D. J. Singh, M. D. Johannes, and M. H. Du. Unconventional superconductivity with a sign reversal in the order parameter of $LaFeAsO_{1-x}F_x$. *Phys. Rev. Lett. 101*, page 057003, 2008. 10

[44] P. Monthoux, D. Pines, and G. G. Lonzarich. Superconductivity without phonons. *Nature 450*, page 1177, 2007. 10

[45] E. G. Moon and S. Sachdev. Quantum critical point shifts under superconductivity: the pnictides and the cuprates. *Phys. Rev. B*, **82**:104516, 2010. 12

[46] G. Mu, H. Luo, Z. Wang, L. Shan, C. Ren, and H.-H. Wen. Low temperature specific heat of the hole-doped $Ba_{0.6}K_{0.4}Fe_2As_2$ single crystals. *Phys. Rev. B 79*, page 174501, 2009. 10

[47] S. Nandi, M. G. Kim, A. Kreyssig, R. M. Fernandes, D. K. Pratt, A. Thaler, N. Ni, S. L. Bud'ko, P. C. Canfield, J. Schmalian, R. J. McQueeney, and A. I. Goldman. Anomalous suppression of the

orthorhombic distortion in superconducting $Ba(Fe_{1-x}Co_x)_2As_2$. *Phys. Rev. Lett.*, **104**:057006, 2010. 2, 8, 9, 40, 79

[48] N. Ni, S. L. Budko, A. Kreyssig, S. Nandi, G. E. Rustan, A. I. Goldman, S. Gupta, J. D. Corbett, A. Kracher, and P. C. Canfield. Anisotropic thermodynamic and transport properties of single-crystalline $Ba_{1-x}K_xFe_2As_2$ (x=0 and 0.45). *Phys. Rev. B*, **78**:014507, 2008. 20

[49] N. Ni, A. Thaler, A. Kracher, J. Q. Yan, S. L. Bud'ko, and P. C. Canfield. Phase diagrams of $Ba(Fe_{1-x}M_x)_2As_2$ single crystals (M=Rh and Pd). *Phys. Rev. B*, **80**:024511, 2009. 39

[50] N. Ni, M. E. Tillman, J.-Q. Yan, A. Kracher, S. T. Hannahs, S. L. Budko, and P. C. Canfield. Effects of co substitution on thermodynamic and transport properties and anisotropic H_{c2} in $Ba(Fe_{1-x}Co_x)_2As_2$ single crystals. *Phys. Rev. B*, **78**:214515, 2009. v, 9, 40, 48

[51] H. Ogino, Y. Matsumura, Y. Katsura, K. Ushiyama, S. Horii, K. Kishio, and J. Shimoyama. Superconductivity at 17 K in $(Fe_2P_2)(Sr_4Sc_2O_6)$: a new superconducting layered pnictide oxide with a thick perovskite oxide layer. *Supercond. Sci. and Technol.*, **22**:075008, 2009. 6

[52] H. Okamoto. The as-fe (arsenic-iron) system. *J. Phase Equilibria*, **12**[4]:457, 1991. 14

[53] J. Paglione and R. L. Greene. High-temperature superconductivity in Iron-based materials. *Nature Physics 6*, pages 645–658, 2010. 11

[54] Z. Ren, Q. Tao, S. Jiang, C. Feng, C. Wang, J. Dai, G. Cao, and Z. Xu. Superconductivity induced by Phosphorus doping and its coexistence with ferromagnetism in $EuFe_2(As_{0.7}P_{0.3})_2$. *Phys. Rev. Lett. 102*, page 137002, 2009. 6

[55] M. Rotter, M. Tegel, and D. Johrendt. Superconductivity at 38 K in the iron arsenide $(Ba_{1-x}K_x)Fe_2As_2$. *Phys. Rev. Lett.*, **101**:107006, 2008. 6, 39, 46

[56] M. Rotter, M. Tegel, D. Johrendt, I. Schellenberg, W. Hermes, and R. Pttgen. Spin-density-wave anomaly at 140 K in the ternary iron arsenide $BaFe_2As_2$. *Phys. Rev. B 78*, page 020503, 2008. 75

[57] C. R. Rotundu, B. Freelon, T. R. Forrest, S. D. Wilson, P. N. Valdivia, G. Pinuellas, A. Kim, J.-W. Kim, Z. Islam, E. Bourret-Courchesne, N. E. Phillips, and R. J. Birgeneau. Heat capacity study of $BaFe_2As_2$: Effects of annealing. *Phys. Rev. B*, **82**:144525, 2010. 75

[58] S. R. Saha, N. P. Butch, K. Kirshenbaum, Johnpierre Paglione, and P. Y. Zavalij. Superconducting and ferromagnetic phases induced by lattice distortions in stoichiometric $SrFe_2As_2$ single crystals. *Phys. Rev. Lett.*, **103**:037005, 2009. 40

[59] S. E. Sebastian, J. Gillett, N. Harrison, P. H. C. Lau, D. J. Singh, C. H. Mielke, and G. G. Lonzarich. Quantum oscillations in the parent magnetic phase of an iron arsenide high temperature superconductor. *J. Phys.: Condensed Matter*, **20**:422203, 2008. 10, 86

[60] A. S. Sefat, R. Jin, M. A. McGuire, B. C. Sales, D. J. Singh, and D. Mandrus. Superconductivity at 22 K in Co-doped $BaFe_2As_2$ crystals. *Phys. Rev. Lett.*, **101**:117004, 2008. 39, 55

[61] A. S. Sefat, D. J. Singh, L. H. VanBebber, Y. Mozharivskyj, M. A. McGuire, R. Jin, B. C. Sales, V. Keppens, and D. Mandrus. Absence of superconductivity in hole-doped $BaFe_{2x}Cr_xAs_2$ single crystals. *Phys. Rev. B*, **79**:224524, 2009. 7

[62] D.J. Singh. Electronic structure of Fe-based superconductors. *Physica C 469*, page 418, 2009. 9, 10

[63] G. R. Stewart. Superconductivity in Iron Compounds. *arxiv:*, page 1106.1618, 2011. 10

[64] U. Stockert, M. Abdel-Hafiez, D. V. Evtushinsky, V. B. Zabolotnyy, A. U. B. Wolter, S. Wurmehl, I. Morozov, R. Klingeler, S. V. Borisenko, and B. Bchner. The superconducting gaps in LiFeAs: Joint study of specific heat and ARPES. *arxiv*, page 1011.4246v1, 2010. 11

[65] Y. Su, P. Link, A. Schneidewind, T. Wolf, P. Adelmann, Y. Xiao, M. Meven, R. Mittal, M. Rotter, D. Johrendt, T. Brueckel, and M. Loewenhaupt. Antiferromagnetic ordering and structural phase transition in $BaFe_2As_2$ with Sn incorporated from the growth flux. *Phys. Rev. B*, **79**:064504, 2009. 46

[66] Y. Su, P. Link, A. Schneidewind, Th. Wolf, P. Adelmann, Y. Xiao, M. Meven, R. Mittal, M. Rotter, D. Johrendt, Th. Brueckel, and M. Loewenhaupt. Antiferromagnetic ordering and structural phase transition in $BaFe_2As_2$ with Sn incorporated from the growth ux. *Phys. Rev. B 79*, page 064504, 2009. 75

[67] M. A. Tanatar, E. C. Blomberg, A. Kreyssig, M. G. Kim, N. Ni, A. Thaler, S. L. Bud'ko, P. C. Canfield, A. I. Goldman, I. I. Mazin, and R. Prozorov. Uniaxial-strain mechanical detwinning of $CaFe_2As_2$ and $BaFe_2As_2$ crystals: Optical and transport study. *Phys. Rev. B*, **81**:184508, 2010. 12

[68] M. A. Tanatar, N. Ni, G. D. Samolyuk, S. L. Budko, P. C. Canfield, and R. Prozorov. Resistivity anisotropy of AFe_2As_2 (A=Ca, Sr, Ba): Direct versus Montgomery technique measurements. *Phys. Rev. B*, **79**:134528, 2009. 29

[69] J. H. Tapp, Z. Tang, B. Lv, K. Sasmal, B. Lorenz, P. C. W. Chu, and A. M. Guloy. LiFeAs: An intrinsic FeAs-based superconductor with T_c=18K. *Phys. Rev. B*, **78**:060505, 2008. 5

[70] M. Tegel, M. Rotter, V. Weiss, F. M. Schappacher, R. Pottgen, and D. Johrendt. Structural and magnetic phase transitions in the

ternary iron arsenides $SrFe_2As_2$ and $EuFe_2As_2$. *J. Phys.: Condens. Matter 20*, page 452201, 2008. 6, 72, 73

[71] M.S. Torikachvili, S. L. Budko, N. Ni, and P. C. Canfield. Pressure-induced superconductivity in $cafe_2as_2$. *Phys. Rev. Lett.*, **101**:057006, 2008. 89

[72] X. F. Wang, T. Wu, G. Wu, R. H. Liu, H. Chen, Y. L. Xie, and X. H. Chen. The peculiar physical properties and phase diagram of $BaFe_{2x}Co_xAs_2$ single crystals. *New Journal of Physics*, **11**:045003, 2009. 6

[73] C. Xu, Y. Qi, and S. Sachdev. Experimental observables near a nematic quantum critical point in the pnictide and cuprate superconductors. *Phys. Rev. B*, **78**:134507, 2008. 12

[74] J. Q. Yan, A. Kreyssig, S. Nandi, N. Ni, S. L. Bub'ko, A. Kracher, R. J. McQueeney, R. W. McCallum, T. A. Lograsso, A. I. Goldman, and P. C. Canfield. Structural transition and anisotropic properties of single-crystalline $SrFe_2As_2$. *Phys. Rev. B*, **78**:024516, 2008. 2

[75] J.-Q. Yan, A. Kreyssig, S. Nandi, N. Ni, S. L. Budko, A. Kracher, R. J. McQueeney, R. W. McCallum, T. A. Lograsso, A. I. Goldman, and P. C. Canfield. Structural transition and anisotropic properties of single-crystalline $SrFe_2As_2$. *Phys. Rev. B 78*, page 024516, 2008. 73

[76] K-W Yeh, T.-W. Huang, Y.-L. Huang, T.-K. Chen, F.-C. Hsu, P. M. Wu, Y.-C. Lee, Y.-Y. Chu, C.-L. Chen, J.-Y. Luo, D.-C. Yan, and M.-K. Wu. Tellurium substitution effect on superconductivity of the alpha-phase Iron Selenide. *Europhys. Lett. 84*, page 37002, 2008. 1, 5

[77] Z. P. Yin, S. Lebe'gue, M. J. Han, B. P. Neal, S.Y. Savrasov, and W. E. Pickett. Electron-hole symmetry and magnetic coupling in antiferromagnetic LaFeAsO. *Phys. Rev. Lett. 101*, page 047001, 2008. 10

[78] M. Yoshizawa, R. Kamiya, R. Onodera, Y. Nakanishi, K. Kihou, H. Eisaki, and C. H. Lee. Strong electron-lattice coupling and orbital

fluctuations in Iron Pnictide superconductor $Ba(Fe_{1-x}Co_x)_2As_2$. *arxiv*, page 1008.1479v3, 2010. 59

[79] W. Yu, A. A. Aczel, T. J. Williams, S. L. Budko, N. Ni, P. C. Canfield, and G. M. Luke. Absence of superconductivity in single-phase $CaFe_2As_2$ under hydrostatic pressure. *Phys. Rev. B*, **79**:020511, 2009. 7

[80] J. Zhao, D. T. Adroja, D. X. Yao, R. Bewley, S. Li, X. F. Wang, G.Wu, X. H. Chen, J. Hu, and P. Dai. Spin waves and magnetic exchange interactions in $CaFe_2As_2$. *Nature Physics 5*, page 555, 2009. 9, 92